

Ionospheric studies at Saturnian satellites

Richard P Haythornthwaite

A dissertation submitted in partial fulfillment
of the requirements for the degree of
Doctor of Philosophy
of
University College London.

Department of Space & Climate Physics
University College London

February 15, 2023

I, Richard P Haythornthwaite, confirm that the work presented in this thesis is my own. Where information has been derived from other sources, I confirm that this has been indicated in the work.

Abstract

An ionosphere refers to the region of charged particles contained in the upper regions of a body's atmosphere. They are typically fed from the neutral atmosphere, which ionises due to sources such as solar photons or precipitating particles. Apart from Mercury, all the planets in the solar system have ionospheres, additionally, ionospheres have been observed at several moons including: Europa, Triton and Titan. This thesis covers several studies regarding ionospheric composition and dynamics at the Saturnian moons of Enceladus and Titan, utilising data from the Cassini-Huygens mission which studied these moons between 2004 and 2017.

The first study focuses on ion velocities in Enceladus's plume as measured by sensors from the Cassini Plasma Spectrometer instrument. One of the key findings from the Cassini mission was a large water ice plume emanating from the south polar region of the moon Enceladus. Cassini made several passes through the plume and the Cassini Plasma Spectrometer sensors made insitu measurements of positive and negatively charged ions. The recorded energies of the ions were used to infer ion velocities along Cassini's trajectory. Two populations were found, associated with faster and slower moving water ion populations. These were linked with velocity characteristics found in the neutral water population. Comparing the velocities of the positive and negative ions also indicated the presence of an electrostatic field in the plume.

The second study covers heavy positive ion measurements in Titan's ionosphere. Previous studies of Titan's ionosphere have revealed a plethora of cations and anions composed of hydrocarbons and nitriles. Using data taken across five Titan flybys by the Cassini Ion Beam Spectrometer sensor, positive ions were stud-

ied with masses ranging from 170 amu up to 350 amu. Examining the possible molecular structure of the ions, the most abundant ion masses were found to be consistent with molecular ions of polycyclic aromatic compounds, including polycyclic aromatic hydrocarbons and nitrogen-bearing polycyclic aromatic hydrocarbons. This was further supported by examining the difference in mass between the most abundant ions. A difference of 12 or 13 amu was found to be the most common, indicating the addition of a carbon or carbon-hydrogen molecule, consistent with polycyclic aromatic hydrocarbon growth pathways.

The third and fourth studies were performed in tandem and cover ion velocities within Titan's ionosphere. Previous studies have examined ion velocities parallel to Cassini's trajectory over a selection of Titan flybys from early on its mission. Here, ion velocities parallel and perpendicular to Cassini's trajectory, known as alongtrack and crosstrack velocities respectively, were derived across a large series of flybys allowing for a statistical approach. For both crosstrack and alongtrack directions, the positive and negative ions velocities were found to be proportional to each other, agreeing with the expectation from ion-neutral collisional coupling. Alongtrack velocities were further investigated through a comparison to the expected superrotation in Titan's ionosphere. Some measurements did not agree with expectations from neutral wind measurements and provide evidence for complex ion wind structures within Titan's ionosphere.

Impact Statement

The first study in this thesis focused on the Enceladus plume, investigating the water ion populations that are present in it. The impact of this study helped advance the discussion around two main topics. Firstly, whether there are fast and slow moving populations in the plume. Secondly, whether an electrostatic field exists within the plume.

The second, third and fourth studies all focused on Titan's atmosphere and ionosphere. The second study focused on the heavy positive ions that exist in the ionosphere, finding that they are likely complex hydrocarbon molecular ions. This advances the discussion around pre-biotic chemistry at Titan and the possible existence of life, which future missions will further investigate. The third and fourth studies investigate winds in Titan's ionosphere, which impact the distribution of molecules around Titan and possibly influence conditions necessary for the creation of complex pre-biotic molecules.

The first two studies in this thesis have been published, Haythornthwaite et al. (2020) and Haythornthwaite et al. (2021), increasing the impact of the work through dissemination of results.

The methodologies used in this thesis will aid future investigation using electrostatic analysers by highlighting what the sensors can currently be used for, issues that need to be resolved and possible resolutions to these issues.

From a wider viewpoint, the studies in this thesis advance the understanding of other worlds and the origins of life. This adds to the discussion of ontological questions such as “Why are we here?”

UCL Research Paper Declaration Form: referencing the doctoral candidate's own published work(s)

Please use this form to declare if parts of your thesis are already available in another format, e.g. if data, text, or figures:

- have been uploaded to a preprint server;
- are in submission to a peer-reviewed publication;
- have been published in a peer-reviewed publication, e.g. journal, textbook.

This form should be completed as many times as necessary. For instance, if you have seven thesis chapters, two of which containing material that has already been published, you would complete this form twice.

1. For a research manuscript that has already been published (if not yet published, please skip to section 2):		
a) Where was the work published? (e.g. journal name)	JGR Space Physics	
b) Who published the work? (e.g. Elsevier/Oxford University Press):	Wiley	
c) When was the work published?	03/02/2020	
d) Was the work subject to academic peer review?	Yes	
e) Have you retained the copyright for the work?	No	
[If no, please seek permission from the relevant publisher and check the box next to the below statement]: <input checked="" type="checkbox"/> I acknowledge permission of the publisher named under 1b to include in this thesis portions of the publication named as included in 1a.		
2. For a research manuscript prepared for publication but that has not yet been published (if already published, please skip to section 3):		
a) Has the manuscript been uploaded to a preprint server? (e.g. medRxiv):	Please select.	If yes, which server? Click or tap here to enter text.
b) Where is the work intended to be published? (e.g. names of journals that you are planning to submit to)	Click or tap here to enter text.	
c) List the manuscript's authors in the intended authorship order:	Click or tap here to enter text.	
d) Stage of publication	Please select.	

3. For multi-authored work, please give a statement of contribution covering all authors (if single-author, please skip to section 4):

R Haythornthwaite – Data Analysis, Paper writing. Other authors: Scientific knowledge, Paper drafting

4. In which chapter(s) of your thesis can this material be found?

Chapter 3

5. e-Signatures confirming that the information above is accurate (this form should be co-signed by the supervisor/ senior author unless this is not appropriate, e.g. if the paper was a single-author work):

Candidate:	Richard Haythornthwaite	Date:	30/09/2022
Supervisor/ Senior Author (where appropriate):	Andrew Coates	Date:	30/09/2022

UCL Research Paper Declaration Form: referencing the doctoral candidate's own published work(s)

Please use this form to declare if parts of your thesis are already available in another format, e.g. if data, text, or figures:

- have been uploaded to a preprint server;
- are in submission to a peer-reviewed publication;
- have been published in a peer-reviewed publication, e.g. journal, textbook.

This form should be completed as many times as necessary. For instance, if you have seven thesis chapters, two of which containing material that has already been published, you would complete this form twice.

1. For a research manuscript that has already been published (if not yet published, please skip to section 2):		
a) Where was the work published? (e.g. journal name)	The Planetary Science Journal	
b) Who published the work? (e.g. Elsevier/Oxford University Press):	American Astronomical Society	
c) When was the work published?	09/02/2021	
d) Was the work subject to academic peer review?	No	
e) Have you retained the copyright for the work?	Yes	
[If no, please seek permission from the relevant publisher and check the box next to the below statement]: <input type="checkbox"/> I acknowledge permission of the publisher named under 1b to include in this thesis portions of the publication named as included in 1a.		
2. For a research manuscript prepared for publication but that has not yet been published (if already published, please skip to section 3):		
a) Has the manuscript been uploaded to a preprint server? (e.g. medRxiv):	Please select.	If yes, which server? Click or tap here to enter text.
b) Where is the work intended to be published? (e.g. names of journals that you are planning to submit to)	Click or tap here to enter text.	
c) List the manuscript's authors in the intended authorship order:	Click or tap here to enter text.	
d) Stage of publication	Please select.	

3. For multi-authored work, please give a statement of contribution covering all authors (if single-author, please skip to section 4):

R Haythornthwaite – Data Analysis, Paper writing. Other authors: Scientific knowledge, Paper drafting

4. In which chapter(s) of your thesis can this material be found?

Chapter 4

5. e-Signatures confirming that the information above is accurate (this form should be co-signed by the supervisor/ senior author unless this is not appropriate, e.g. if the paper was a single-author work):

Candidate:	Richard Haythornthwaite	Date:	30/09/2022
Supervisor/ Senior Author (where appropriate):	Andrew Coates	Date:	30/09/2022

Acknowledgements

I would like to thank my supervisors Andrew Coates and Geraint Jones for their support and guidance throughout my PhD. I would also like to thank Annie Wellbrock for her insight on the Titan studies in this thesis.

Through my years at MSSL I had the joy of spending it with some great people who made the experience far more enjoyable: Frankie Staples, Michaela Mooney, Qasim Afghan, Catherine Regan, Will Dunn, Ahlam Al Qasim. A special mention for my planetary student colleague, fellow big planet lover and desk neighbour Affelia Wibisono.

I would like to acknowledge my collaborators for the papers published from this thesis, whose invaluable feedback definitely improved the quality of the work.

A substantial portion of my PhD was during the COVID-19 pandemic, so I would like to acknowledge the friendship and camaraderie I shared during those bleak times with my housemates: Curtis May, Hannah Drumm, Ryan French and Georgie Getley.

I would also like to personally acknowledge my partner Katie Simkins, whose constant love and support helped me immensely through my PhD.

List of Papers

1. Nicolaou, G., **R. P. Haythornthwaite**, & A. J. Coates, Resolving Space Plasma Species With Electrostatic Analyzers, *Frontiers in Astronomy and Space Sciences*, vol. 9, id. 861433, 10.3389/fspas.2022.861433, 06/2022
2. Wibisono, A. D., G. Branduardi-Raymont, W. R. Dunn, T. Kimura, A. J. Coates, D. Grodent, Z. H. Yao, H. Kita, P. Rodriguez, G. R. Gladstone, B. Bonfond, & **R. P. Haythornthwaite**, Jupiter's X-ray aurora during UV dawn storms and injections as observed by XMM-Newton, Hubble, and Hisaki, *Monthly Notices of the Royal Astronomical Society*, Volume 507, Issue 1, pp.1216-1228, 10.1093/mnras/stab2218, 10/2021
3. **Haythornthwaite, R. P.**, A. J. Coates, G. H. Jones, A. Wellbrock, J. H. Waite, V. Vuitton, & P. Lavvas, Heavy Positive Ion Groups in Titan's Ionosphere from Cassini Plasma Spectrometer IBS Observations, *The Planetary Science Journal*, Volume 2, Issue 1, id.26, 13 pp., 10.3847/PSJ/abd404, 02/2021
4. Mihailescu, T., R. T. Desai, O. Shebanits, **R. Haythornthwaite**, A. Wellbrock, A. J. Coates, J. P. Eastwood, & J. H. Waite, Spatial Variations of Low-mass Negative Ions in Titan's Upper Atmosphere, *The Planetary Science Journal*, Volume 1, Issue 2, id.50, 8 pp., 10.3847/PSJ/abb1ba, 09/2020
5. **Haythornthwaite, R. P.**, A. J. Coates, G. H. Jones, & J. H. Waite, Fast and Slow Water Ion Populations in the Enceladus Plume, *Journal of Geophysical Research: Space Physics*, Volume 125, Issue 2, article id. e27591, 10.1029/2019JA027591, 02/2020

Contents

1	Introductory Material	28
1.1	Plasma Physics	28
1.1.1	Plasma definition	28
1.1.2	Single particle motion	29
1.1.3	Particle gyromotion	29
1.1.4	$\mathbf{E} \times \mathbf{B}$ drift	30
1.1.5	Ion-neutral collisions	31
1.2	Ion-neutral pathways	32
1.2.1	Ion formation and loss	32
1.2.2	Ionisation energy and electron affinity	34
1.3	Planetary magnetospheres	34
1.3.1	Induced magnetospheres	34
1.4	Ionospheric Physics	35
1.4.1	Ionospheric dynamo region	37
1.5	Saturn's magnetosphere & moons	37
1.5.1	Enceladus	37
1.5.2	Titan	39
1.6	Thesis outline	43
2	Methods and Instrumentation	44
2.1	Electrostatic analysers	44
2.2	The Cassini-Huygens mission	45
2.3	Cassini Plasma Spectrometer (CAPS)	45

<i>Contents</i>	9
2.3.1 Electron Spectrometer (ELS)	46
2.3.2 Ion Mass Spectrometer (IMS)	47
2.3.3 Ion Beam Spectrometer (IBS)	47
2.4 CAPS measurements of cold plasmas	48
2.5 Spacecraft charging	49
3 Fast and Slow Water Ion Populations in the Enceladus Plume	51
3.1 Introduction	51
3.2 Particle Velocities in the Enceladus Plume	52
3.3 Methodology	53
3.4 Results	54
3.4.1 E5 Flyby	55
3.4.2 E3 Flyby	62
3.5 Discussion	64
3.5.1 EM-fields	65
3.5.2 Other Possibilities	66
3.6 Summary and Conclusions	66
4 Heavy Positive Ion Groups in Titan's Ionosphere from Cassini Plasma Spectrometer IBS Observations	68
4.1 Introduction	68
4.2 Methodology	70
4.2.1 Cassini Plasma Spectrometer	71
4.2.2 Data Analysis and Ion Winds	71
4.2.3 High Mass Methodology and Uncertainties	73
4.2.4 Studied Flybys	76
4.3 Results	76
4.3.1 Previously Reported Ion Groups (100 - 200 u/q)	78
4.3.2 High Mass Ions (170 - 310 u/q)	80
4.4 Discussion	82
4.4.1 Ion Mass Group Composition	84

<i>Contents</i>	10
4.4.2 Variations between Flybys	86
4.4.3 Comparison with Neutral PACs in Titan’s Atmosphere	89
4.5 Conclusions	90
5 Ion velocities and spacecraft charging in Titan’s ionosphere: I.	
Crosstrack velocities and Cassini spacecraft potentials	92
5.1 Introduction	93
5.1.1 Spacecraft potential measurements and discrepancies	93
5.2 Methodology	94
5.2.1 Crosstrack ion velocities	94
5.2.2 Spacecraft potential	98
5.2.3 Cassini Flybys	99
5.3 Results	99
5.3.1 Crosstrack Ion Velocities	99
5.3.2 Derived spacecraft potential	100
5.4 Discussion	104
5.4.1 Crosstrack velocity distributions and magnitudes	104
5.4.2 Spacecraft potential measurements	106
5.4.3 Spacecraft potential discrepancies	108
5.5 Conclusions	109
6 Ion velocities and spacecraft charging in Titan’s ionosphere: II. Along-track velocities and their connection to neutral winds	111
6.1 Introduction	111
6.2 Methodology	115
6.2.1 Alongtrack ion velocities	115
6.3 Results	120
6.3.1 Actuating flybys	120
6.3.2 Fixed actuation flybys: T55-T59	121
6.4 Discussion	123
6.4.1 Ion velocity distributions and magnitudes	123

<i>Contents</i>	11
6.4.2 Corotational Flow	130
6.4.3 Electrodynamic dynamo region	130
6.4.4 Driving from below and circulation cells	132
6.4.5 Instrumentation uncertainties	133
6.5 Conclusions	134
7 Conclusions and Further Work	136
7.1 Summary & Conclusions	136
7.1.1 Enceladus	136
7.1.2 Titan	137
7.2 Further Work	139
7.2.1 CAPS heavy ion energy-angle response	139
7.2.2 3D velocity determination	139
7.2.3 Cassini spacecraft charging model in Titan’s ionosphere . .	140
7.2.4 Future mission & campaigns	140
Appendices	143
A Studied Titan flybys	143
A.1 Table A.1	143
A.2 Table A.2	144
B Acronyms	145
Bibliography	146

List of Figures

1.1	Diagram depicting simple $\mathbf{E} \times \mathbf{B}$ drift in uniform fields, the drift velocity can be seen to be perpendicular to both fields. Diagram from Kivelson et al. (1995)	30
1.2	Diagram demonstrating the orientation of the Parallel, Hall and Pedersen currents in relation to the electric and magnetic fields.	31
1.3	Diagram highlighting several features of Saturn's magnetosphere. Image credit: NASA	35
1.4	The various layers of the Earth's atmosphere, with the E and F regions of the ionosphere shown on the right. As can be seen, ionospheric layers overlap with atmospheric layers, with the terms used depending on context. [Credit: (Kelley, 2009)]	36
1.5	Figure demonstrating the difference between dayside and nightside ionospheric layers. Four layers are seen on the dayside while only two are seen on the nightside. [Credit: NASA's Goddard Space Flight Center/Mary Pat Hrybyk-Keith]	37
1.6	Picture of Enceladus taken by Cassini on 28th October 2015 at a distance of approximately 96,000 km.	38
1.7	Picture of Titan taken by Cassini on 30th January 2012 at a distance of approximately 191,000 km.	39
1.8	Figure demonstrating the various atmospheric layers of Titan. [Source: https://commons.wikimedia.org/wiki/File:Titan%27s_atmosphere.svg]	41

1.9	Figure demonstrating the different positions of Titan's corotation and solar wakes during its orbit (Coates, 2009).	42
2.1	Cartoon showing the operation of an electrostatic analyser and how particles with different charges and energies pass through it.	44
2.2	Diagram outlining CAPS sensors from Young et al. (2004).	46
3.1	An overview of the trajectories of the Enceladus flybys studied in the Enceladus frame. The closest approaches are shown with triangles. The Cassini start position helps indicate Cassini's direction of travel. Both the E3 and E5 flybys were -Z directed flybys. The geometric corotational wake of Enceladus is indicated by the green lines.	54
3.2	The Cassini trajectory in the YZ plane during the E3 and E5 flybys. Negative Y is in the direction of the corotation of magnetospheric plasma. The highlighted red areas of the trajectories between the labels A#-B# and C#-D# where # is 3 or 5 correspond to the E3 and E5 flybys respectively, are the regions where the low energy peak occurs in the energy spectrograms. Similar labels can be found in subsequent figures. The squares indicate an arbitrary start location to help demonstrate the north-south direction that Cassini traveled in, the black triangle indicates the location of closest approach, while the dots indicate Cassini's location at 1 minute intervals. The geometric corotational wake of Enceladus is indicated by the green lines.	55

3.6	Energy spectrogram of the IMS ram anodes (Anodes 4 and 5) during the E3 flyby. Horizontal lines indicate energy locations of various molecules, solid lines indicate the location of an entirely stagnated flow without corrections, whilst the dot-dashed lines indicate the locations with spacecraft potential and ion velocity corrections applied.	62
3.7	Spectrogram using ELS data from the E3 flyby, similar annotations to Figure 3.5	63
3.8	Spectrograms of IBS data gathered during the E7, E17 and E18 flybys. Comparing to the E3 and E5 flybys, no consistent second energy peak can be seen across adjacent sweeps.	64
4.1	An example of an IBS energy spectrum taken during the T57 flyby. The error bars shown represent the uncertainty due to Poisson counting error. Red x's indicate the peaks as identified by the peak finding algorithm. Due to the logarithmic energy scale, at low energies the ion beams can be seen over a number of bins, while at the high energies the beams can only be seen in a single bin.	70
4.2	An energy/charge spectrogram from the T59 Titan flyby with intensity shown in Differential Energy Flux (DEF). Peaks identified by the algorithm are indicated by the black dots. The mass groups identified can be seen by horizontal lines of dots. Small variations in the energy of the identified peaks are due to effects such as ion velocity, spacecraft potential and slight shifts in spacecraft orientation. The energy shift on the inbound leg of the flyby (before 15:30) is due to the acceleration of ions away from Titan.	72

- 4.3 These three panels are used to illustrate the difference between observing low mass and high mass ion beams with the IBS sensor. For all three panels, the red lines represent the IBS response, with each gaussian curve representing a different IBS energy bin. The black line represents an observed ion beam, idealized with a gaussian and the width being determined by equation 4.1. The blue lines are each of the IBS energy bins (red) multiplied by the ion beam (black) and are representative of the spectra generated by IBS. 74
- 4.4 a) An altitude-mass plot for every peak identified by the peak finding algorithm at the altitudes examined. The error bars represent the instrument uncertainty for the peak detection. Each color represents a different flyby, T55 - blue, T56 - orange, T57 - green, T58 - red, T59 - purple. Panel b) is a section of panel a) between 200 and 300 u/q. Clear grouping of ions can be seen, notably around 203, 217, 229, 241 and 266 u/q, labelled C16, C17, C18, C19 and C21 respectively, as discussed in Section 4.3.2. 77
- 4.5 The black line represents the summed percent occurrence of the peaks over the flybys with 1 u/q binning from the present study. The blue line represents the percent occurrence from Crary et al. (2009). Good agreement can be seen, with the present study showing more defined peaks for the ion groups around 180 and 190 u/q. 79

- 5.1 This figure displays data from the T49 flyby to illustrate how the crosstrack velocities are observed using time-energy spectrograms and the actuator position. All panels have time on the x-axis, with energy on the y-axis for the top three panels which are spectrograms while the bottom panel has azimuthal angle on the y-axis. On the three spectrograms intensity in Differential Energy Flux (DEF) is shown in colour. The top two spectrograms are two anodes from the ELS sensor, while the third spectrogram is from the IBS central fan. In the last panel the actuator position is shown with the red line as it actuates back and forth across the angle associated with Cassini's trajectory, this angle is shown with the horizontal black line. When the actuator crosses Cassini's trajectory vector, a vertical black line is added across all panels, indicating the expected angle that ions would arrive from if crosstrack velocities were not present. The vertical dotted and dashed lines represent the direction that the heaviest negative and positive ions respectively are measured from. These are associated with the near horizontal dotted/dashed lines in the last panel which show at what angle these ions are measured at. . . . 95

- 5.2 A cartoon to illustrate the field of view (FOV) of CAPS ELS and a brief pictoral depiction of the methodology in this study. Shown on the right is the FOV for CAPS ELS, with 8 anodes across the elevation direction and CAPS rotating with its actuator around the azimuthal direction. The middle fan of IBS has a similar FOV but without anodes along the elevation direction. Typically during the Titan flybys used in this study, CAPS actuates across the velocity vector so that the central anodes of ELS pass over the incoming ions. The direction the incoming ions would appear from without the effect of crosstrack velocities is noted by vertical red lines, where they are actually observed coming from is noted by the vertical red dashed line. As can be seen, this difference is associated with an angle relating to the crosstrack velocity as described in the text. 96
- 5.3 A latitude/longitude plot to display the spatial coverage of the data used. As can be seen, there is variation in sampling, but most latitudes and longitudes are covered. 99
- 5.4 The distribution of the cation and anion crosstrack velocities as measured from CAPS IBS and ELS respectively, with 1D distributions plotted on the sides. In the plot text, the equation describing the best linear regression fit is shown, as well as 95% confidence interval values for the correlation coefficient . The fit is shown with the red dashed line, along with a 95% confidence interval in red shading. The black line is a $y=x$ line to highlight the offset. 100

- 5.8 A plot demonstrating the investigation of pairwise relationships between derived values. The values shown are derived spacecraft potentials from IBS and ELS, as well as crosstrack velocities from the sensors as well. All derived values are shown, including where ELS values cannot be derived, this causes the distributions to not always be reflected in the scatter plots. As can be seen in the scatter plots there is good correlation between the crosstrack velocities, but no correlations can be seen between the crosstrack velocities and spacecraft potentials. 107
- 6.1 A cartoon extending on Figure 5.2. The bottom plot demonstrates the flux fitting process applied across an energy sweep which is covered further in this chapter. The red dashed line on the spectrogram cuts along the y-axis which represents energy, in the bottom plot the energy is shown on the x-axis to allow demonstration of the flux fitting process. 115
- 6.2 An example to illustrate the fitting algorithm to derive positive ion alongtrack velocities from IBS data. On the x-axis, energy/charge is plotted linearly and counts/second is plotted on the y-axis with logarithmic scaling. The IBS data spectrum is shown with a green step plot, with the logarithmic spaced energy bin visible. The energy peaks are not necessarily from the same energy sweep, this is due to the methodology which accounts for if peak fluxes of different ion masses don't appear in the same energy sweep. It then combines the spectra into the single spectrum seen above. Multiple Gaussians curves are shown in blue which are fitted to ion peaks associated with the various ion families observed in the spectra. The best fit of the Gaussians to the data is shown in black. Several statistics are shown in the bottom right, highlighting the derived parameters and goodness of fit (GOF). 116

6.6 A cartoon demonstrating trajectories of Cassini flybys through Titan's ionosphere. Trajectories of three Titan flybys: T17, T43 and T55 are shown, with T17 passing Titan on the Saturn-facing sector and the other two passing on the opposite side. Shells are overlaid on Titan indicating different atmospheric layers. The innermost layer, with red arrows, indicates the portion of Titan's atmosphere which corotates/superrotates with the moon. The next layer, with purple arrows, displays different characteristics while the last layer, with blue arrows, has velocities consistent with loss to Saturn's magnetosphere. The green lines indicate the geometric wake of Titan.	124
6.7 Datapoints from the low-latitude actuating flybys used in this study. The four columns are arranged by the 4 longitude sectors described in the text with longitudes plotted on the x-axis. The top row has the latitude on the y-axis, with altitude and solar zenith angle on the middle and bottom rows respectively.	125
6.8 Alongtrack positive ion velocity measurements of the low latitude (within 50.5 degrees of the equator) actuating flybys, separated by sector in the first four panels. The four 90 degree longitude sectors are the Saturn-facing, wake side (the wake caused by the corotational flow in the magnetosphere), anti-Saturn facing and ram sector. In each panel ion velocity measurements from flybys are shown with errorbars in colour, with an average shown in black. The lines plotted are binned in altitude, with each bin being 100 km, the lowest bin is centred at 1000 km. The errorbars on the black lines indicate the standard deviation of the data points in that altitude bin. Some flybys can span multiple panels, if that flyby crossed multiple sectors. The fifth panel shown highlights the averages found on Saturn-facing and anti-Saturn facing sectors studied.	126
6.9 The same as Figure 6.8 but for negative ion measurements.	127

List of Tables

3.1	The velocity ranges of positive and negative ions in ms^{-1} for the two Enceladus flybys examined. The ranges result from spacecraft potential discrepancies and the energy resolution of the CAPS sensors. E3 H_3O^+ velocities are calculated from IMS data while E5 H_3O^+ velocities are calculated from IBS data. ELS is used for both E3 and E5 in the OH^- ion velocity determination.	58
4.1	Table displaying the data used in this study. The time where Cassini emerged from Titan’s geometric shadow is shown in the under “Titan shadow exit UTC time”. Min and Max altitudes demonstrate that these samples were taken at some of the lowest regions of Titan’s ionosphere traversed by Cassini. Latitude(Lat) and Longitude(Long) are displayed at the closest approach during the flyby. Solar Zenith Angle(SZA) Range is the range of SZA values observed in the sample range. Titan Local Time is shown in the last column.	78

A.1 Alt, Lat, Lon and SZA are Altitude (in km), Latitude (deg), Longitude (deg) and Solar Zenith Angle (deg) are within 2 minutes of closest approach, values are from the Atmospheres Node of NASA PDS. The "Cross-vel" column contains pairs of (positive ion crosstrack velocity, negative ion crosstrack velocity) in m/s as measured nearest to closest approach, the sign indicates the direction of the velocity. "Along-vel" is similar to "Cross-vel" but for along-track velocities, with positively signed values indicating headwinds in the Cassini frame.	143
A.2 For column descriptions see previous table. Flybys T55 through T59 do not have cross-track velocity measurements and the along-track velocities are an average of 40 seconds around closest approach.	144

Chapter 1

Introductory Material

1.1 Plasma Physics

Most of the plasma physics concepts described here are explained in further detail in Baumjohann and Treumann (1996) and Kivelson et al. (1995).

1.1.1 Plasma definition

A standard definition of plasma is “a quasineutral ionized gas that exhibits collective behaviour”. Quasineutrality implies that there is very little or no electric charge present, meaning the electrons and ions rearrange to cancel out any charge imbalances. The fundamental length scale this occurs at is known as the Debye length. A standard Coulombic potential of a single charged particle is given by:

$$\phi_{vac} = \frac{Q}{4\pi\epsilon_0 r} \quad (1.1)$$

where Q is the charge of a particle, r is the distance from the particle. Through the use of statistical physics it can be shown that the potential in a plasma falls as:

$$\phi_{debye} = \frac{Q}{4\pi\epsilon_0 r} \times \left(\frac{-r}{\lambda_D}\right) \quad (1.2)$$

where λ_D is the Debye length and is given as,

$$\lambda_D = \sqrt{\frac{\epsilon_0 k_B T}{e^2 n_e}} \quad (1.3)$$

where k_B is the Boltzmann constant, T is the plasma temperature and n_e is

the electron density. At lengths larger than the Debye length, the electric fields created by the charged particles cancel each other out, generating the quasineutrality condition.

From the Debye length, a sphere of radius λ_D known as the Debye sphere can be defined. The number of electrons inside the Debye sphere is known as the plasma parameter, defined as,

$$N_D = \frac{4\pi}{3} \lambda_3^3 n_e \quad (1.4)$$

where N_D is the plasma parameter. For an “ideal plasma”, $N_D \gg 1$ meaning that the plasma is “weakly coupled”. If this condition does not hold then the plasma is “strongly coupled”, implying low temperatures and high density are present. This could therefore represent a non-plasma state such as a gas, liquid or solid.

1.1.2 Single particle motion

The force exerted on a single charged particle by electromagnetic fields is determined by the Lorentz equation,

$$\mathbf{F}_p = q_p(\mathbf{E} + \mathbf{v}_p \times \mathbf{B}) \quad (1.5)$$

where the force on the particle \mathbf{F}_p is calculated from the charge q_p and velocity \mathbf{v}_p of the particle, in addition to the electric and magnetic field vectors.

1.1.3 Particle gyromotion

As a result of the Lorentz force, a particle moving perpendicular to a uniform magnetic field will perform a circular orbit. This motion generates fundamental frequency and length scales for the motion of a charged particle. The frequency is known as the Larmor frequency, cyclotron frequency or gyrofrequency, given by

$$\Omega_c = \frac{|q|B}{m} \quad (1.6)$$

which represents the angular frequency of a particle with charge q and mass m , in a uniform magnetic field with strength B . The resulting orbital radius is known

as the Larmor radius or gyroradius, and can be calculated by

$$r_L = \frac{v_\perp}{\Omega_c} = \frac{mv_\perp}{|q|B} \quad (1.7)$$

similar to $r = v/\omega$. A key difference is that all particles of the same species will have the same gyrofrequency but their gyroradii are dependent on each particle's velocity relative to the magnetic field. If the particle has a velocity component parallel to the magnetic field the particle will undergo helical motion around the magnetic field line.

1.1.4 $\mathbf{E} \times \mathbf{B}$ drift

The addition of a uniform electric field causes the charged particles to gain a drift velocity, as seen in Figure 1.1. This drift velocity is described by

$$\mathbf{v}_e = \frac{\mathbf{E} \times \mathbf{B}}{|\mathbf{B}|^2} \quad (1.8)$$

where \mathbf{v}_e is the drift velocity, \mathbf{E} and \mathbf{B} are the electric and magnetic field vectors respectively. This implies that the drift velocity is perpendicular to both fields and that the guiding centre, the point that the charged particles gyrate around, drifts across field lines.

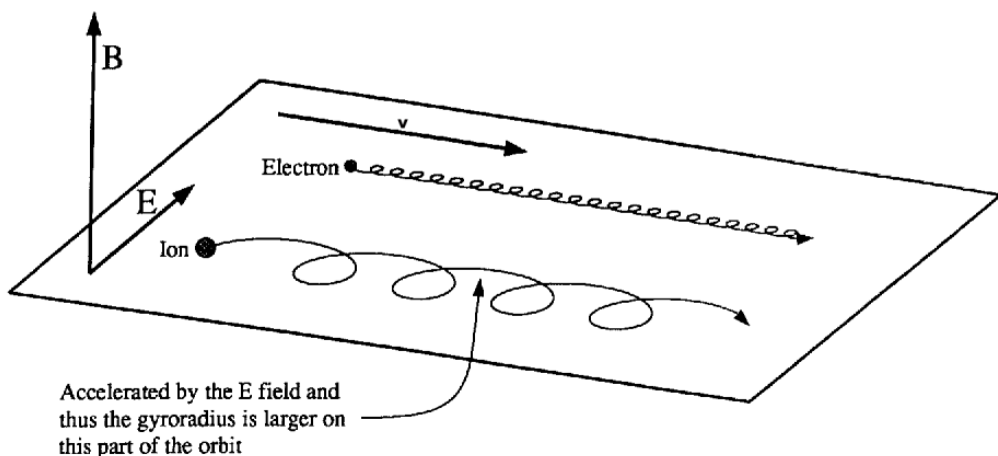


Figure 1.1: Diagram depicting simple $\mathbf{E} \times \mathbf{B}$ drift in uniform fields, the drift velocity can be seen to be perpendicular to both fields. Diagram from Kivelson et al. (1995)

1.1.5 Ion-neutral collisions

Under certain conditions, ion-neutral collisions can become dominant over electromagnetic effects in determining the ion dynamics. Understanding when collisions dominate is done by comparing the ion gyrofrequency to the ion-neutral collision frequency, i.e. $k = \Omega_c / \bar{v}_{in}$, where if $k \gg 1$ then EM effects dominate and where $k \ll 1$ collisions dominate (Sangalli et al., 2009). We have previously defined the gyrofrequency in Equation 1.6.

One definition of the ion-neutral collision frequency is

$$\bar{v}_{in} = \frac{n_i m_i + n_n m_n}{m_i m_n} 2.21\pi(\alpha e^2 \mu)^{1/2} \quad (1.9)$$

from Banks and Kockarts (1973), which accounts for how differing neutral and ion densities affect the ion-neutral collision frequency. \bar{v}_{in} is the ion-neutral collision frequency, n_i and n_n are the ion and neutral densities respectively, m_i and m_n are the ion and neutral masses respectively, α is the atomic polarizability, μ is the ion-neutral reduced mass and e is the electric constant.

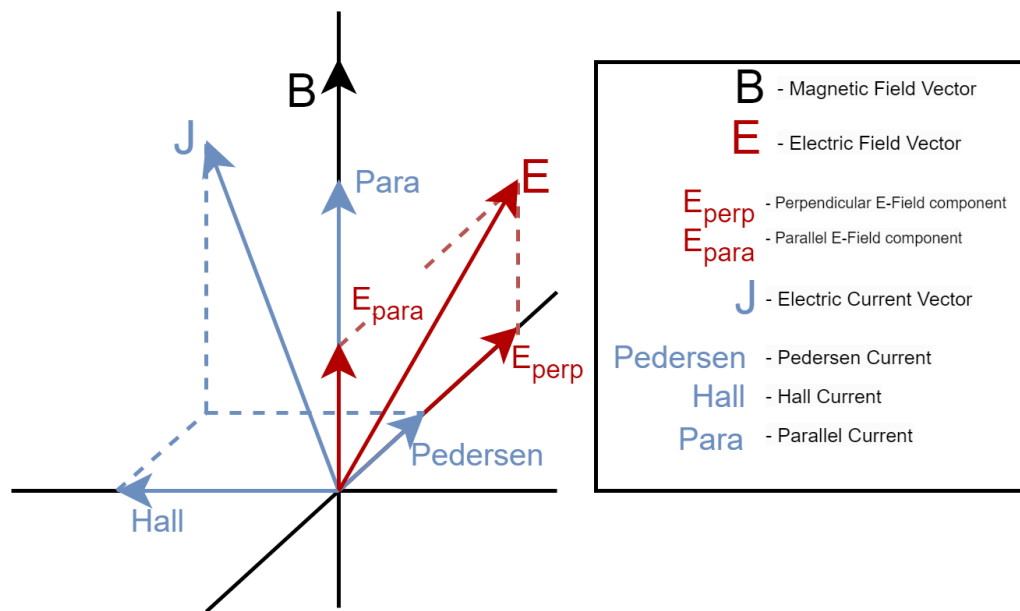


Figure 1.2: Diagram demonstrating the orientation of the Parallel, Hall and Pedersen currents in relation to the electric and magnetic fields.

When a magnetic field is present, collisions affect the conductivity in an

anisotropic manner within ionospheres. The conductivity can be broken into three parts, these are the Parallel, Hall and Pedersen conductivities (see Figure 1.2). Parallel conductivity is parallel to the magnetic field, Pedersen conductivity is perpendicular to the magnetic field but parallel to the electric field and Hall conductivity is perpendicular to both the magnetic and electric fields. Hall currents are driven by the $\mathbf{E} \times \mathbf{B}$ drift and Pedersen currents are driven by the electric field. Both Hall and Pedersen conductivities are dependent on ion-neutral and electron-neutral collision frequencies, as well as the respective gyroperiods of the charged particles. However, the parallel conductivity is only dependent on the collision frequencies (Kivelson et al., 1995).

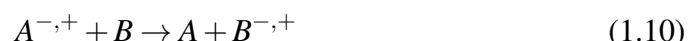
1.2 Ion-neutral pathways

There are many reaction pathways for neutral molecules to become ionised. These processes can range from simple photoionisation to processes which also affect the composition of the neutral and plasma phases, such as ion-pair formation. Here I will cover a selection of the most prominent ion formation and loss processes in heliospheric environments. The negative ion chemistry in this section is adapted from Millar et al. (2017).

1.2.1 Ion formation and loss

1.2.1.1 Charge exchange

Charge exchange is the exchange of an electron between a fast moving ion and a slow neutral.



This process can occur with both positive and negative ions. Charge exchange does not change the combined composition of the ion and neutral phases but does affect the relative composition of the phases. In addition it also affects the velocity distributions of the species in the reaction by replacing fast ions with fast neutrals and slow ions with slow neutrals. This process can also work in reverse with slow

moving ions and fast neutrals.

1.2.1.2 Photoionisation and photodetachment

Photoionisation is the removal of an electron from a neutral molecule by a photon.



A similar process occurs for negative ions, known as photodetachment, creating neutral molecules.



The photon energy must be higher than the electron affinity of the negative ion for photodetachment to take place.

1.2.1.3 Electron impact ionisation

Electron impact ionisation is when an energetic electron collides with a neutral particle and removes an electron from the atom resulting in a positively charged ion.



1.2.1.4 Ion-pair formation

Ion-pair formation is a process where both a positively charged fragment and negatively charged fragment are created from a neutral molecule. This reaction can be induced for excited neutrals atoms by either photon interactions or collisions with electrons.



1.2.1.5 Dissociative recombination

Dissociative recombination is where a positive molecular ion combines with an electron and creates multiple neutral fragments.



There is no energy barrier for this reaction to proceed, making it a common reaction in astrophysical contexts.

1.2.2 Ionisation energy and electron affinity

Ionisation energy is defined as the minimum energy required to remove the outermost electron of a gaseous atom, ion or molecule. For neutral atoms the ionisation energy is positive, meaning it is an endothermic process and requires energy to be put into a system to remove the outermost electron.

A related concept is electron affinity. Electron affinity is defined as the amount of energy released when an electron attaches to a neutral atom or molecule in gaseous state. Through this electron attachment an anion is formed. There are some commonalities with the idea of electronegativity. Such as chlorine having a high electron affinity and electronegativity, this is due to the extra electron filling the outermost valence shell.

1.3 Planetary magnetospheres

A planetary magnetosphere is created when plasma surrounding a body encounters the external solar wind, Figure 1.3 shows Saturn's magnetosphere as an example. Two main boundaries are present, the outermost is the bow shock, where the solar wind plasma is slowed and heated. The other is the magnetopause, which results from a pressure balance between the shocked solar wind plasma and the planetary plasma and magnetic field. The region between the bow shock and magnetopause is known as the magnetosheath. Behind the planetary body the magnetotail stretches for a much greater distance than the magnetosphere on the sun-facing side.

1.3.1 Induced magnetospheres

Another form of magnetosphere is the induced magnetosphere, which can be created when no substantial planetary dynamo exists and therefore no magnetic field. Venus and Mars are examples of induced magnetospheres. Here, the solar wind

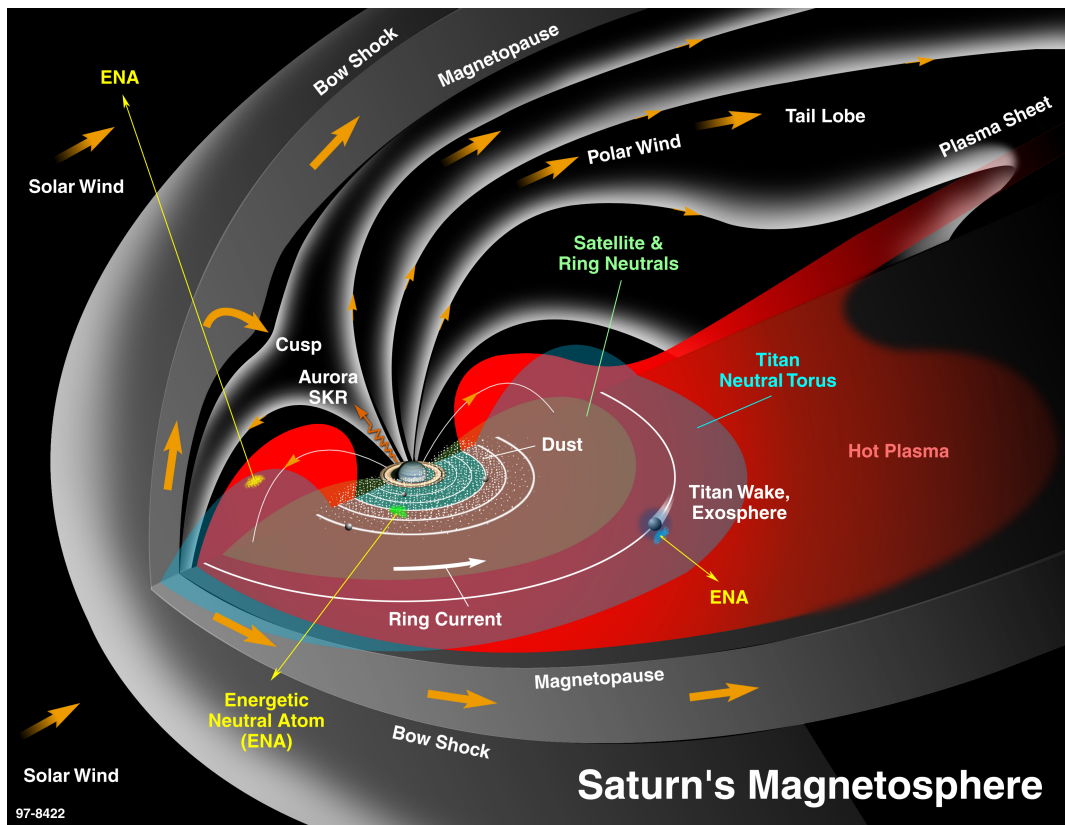


Figure 1.3: Diagram highlighting several features of Saturn's magnetosphere. Image credit: NASA

magnetic field cannot penetrate the conducting ionosphere and drapes around the planetary body. This creates a similar configuration to the typical magnetosphere including a magnetotail and magnetopause.

1.4 Ionospheric Physics

An ionosphere exists between a body's atmosphere and magnetosphere, and contains both ionised plasma and neutral molecules. The neutral molecules act as a source for the ionised material, with the majority of known ionospheres being created by photoionisation from solar UV photons. Additional ionisation can come from precipitating energetic electrons and ions which can be the primary source of ionisation on the nightside of bodies.

The vertical structure of Earth's atmosphere and ionosphere is shown in Figure 1.4. The various atmospheric layers are seen on the left side of the figure from the troposphere through to the exosphere. In contrast, the right side shows the

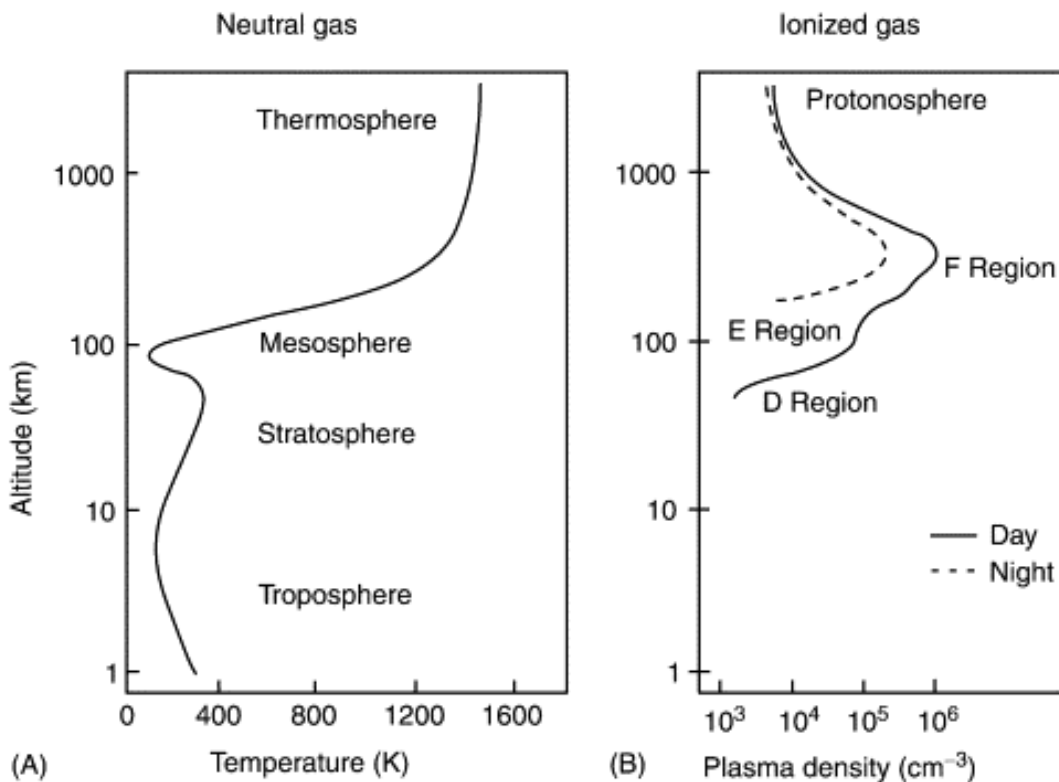


Figure 1.4: The various layers of the Earth's atmosphere, with the E and F regions of the ionosphere shown on the right. As can be seen, ionospheric layers overlap with atmospheric layers, with the terms used depending on context. [Credit: (Kelley, 2009)]

ionosphere and the primary two layers, the E and F layers. Thus demonstrating the somewhat complex and overlapping definitions of atmospheric and ionospheric layers.

This complexity is furthered by a daytime/nighttime split in the ionosphere, highlighted by Figure 1.5. On the nightside the two layers are the ones previously described, the E and F region layers, whereas on the dayside there are four layers. Going outwards from Earth, these are the D, E, F₁ and F₂ layers. The ionisation sources and densities of these layers all vary.

Across these layers, the interaction between neutrals and ions also changes. Sangalli et al. (2009) showed through measurements of the ion velocity, neutral wind velocity and electric field that there is a transition around 118km between a region where the ion drift velocity is dominated by ion-neutral collisions to a region where $\mathbf{E} \times \mathbf{B}$ drift dominates the ion drift velocity.

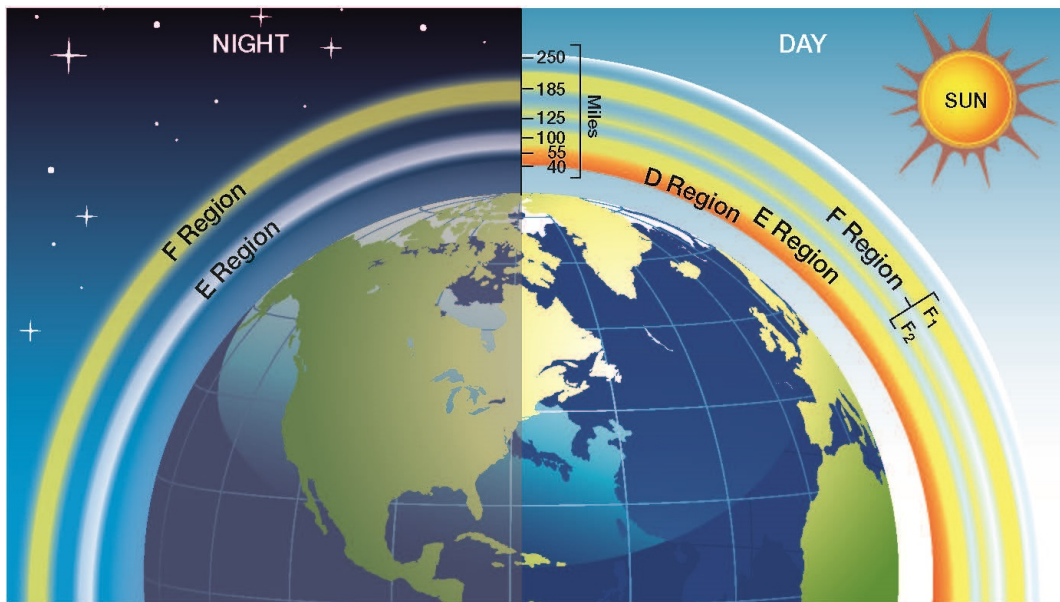


Figure 1.5: Figure demonstrating the difference between dayside and nightside ionospheric layers. Four layers are seen on the dayside while only two are seen on the nightside. [Credit: NASA's Goddard Space Flight Center/Mary Pat Hrybyk-Keith]

1.4.1 Ionospheric dynamo region

In a region of Earth's ionosphere between 85 and 200 km the ionospheric plasma is electrically conductive. The lower boundary of this region is where the electron gyrofrequency is equal to the electron-neutral collision frequency. The upper boundary is where the ion gyrofrequency is equal to the ion-neutral collision frequency (Shebanits et al., 2022). Between the boundaries the ions are collisionally coupled to the neutral atmosphere while the electrons can still move along magnetic field lines. This causes the electrical conductivity to become anisotropic.

1.5 Saturn's magnetosphere & moons

This section provides a brief overview of the Saturnian satellites studied in this thesis and the magnetospheric environment they are exposed to.

1.5.1 Enceladus

Enceladus is the sixth largest moon of Saturn and was discovered in 1789 by William Herschel. The moon is entirely covered in ice, making it one of the most reflective bodies in the solar system. It has an equatorial diameter of 513km and

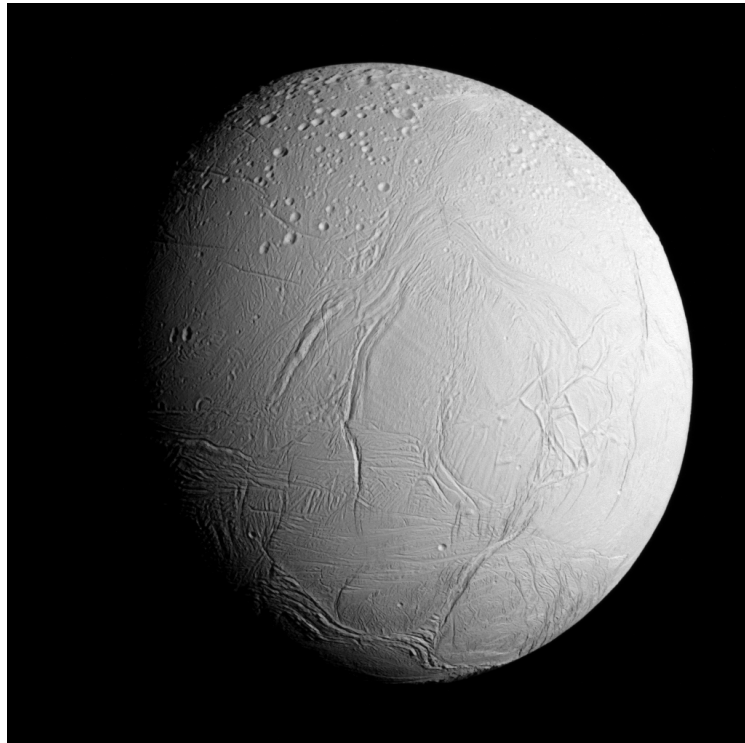


Figure 1.6: Picture of Enceladus taken by Cassini on 28th October 2015 at a distance of approximately 96,000 km.

was first studied in-situ by the Voyager probes in 1980 and 1981. Detailed studies were not performed until the Cassini-Huygens mission to the Saturnian system. The Cassini investigation consisted of 22 targeted flybys of the moon between 2005 and 2015, and covered a variety of flyby velocities and geometries.

The most startling find of the flybys was the discovery of a plume emanating from around the moon's south pole (Dougherty et al., 2006). The plume was later shown to fuel Saturn's E-ring. Below the exterior ice layer, the existence of a subsurface ocean was discovered, it being the source of the plume material. When Cassini flew through the water plume, it allowed sampling of the subsurface ocean material.

Through Cassini measurements, water was found to be the major constituent in all three plume phases: dust, gas and ions. Water makes up 98% of the gas phase, with the rest being mostly composed of carbon dioxide, methane, ammonia and molecular hydrogen (Waite et al., 2009; Waite et al., 2017; Waite et al., 2019).

With no internal magnetic dynamo, the plume material is directly exposed to

the corotational flow in Saturn's magnetosphere, causing the flow to slow and undergo interactions with the plume material.

1.5.2 Titan

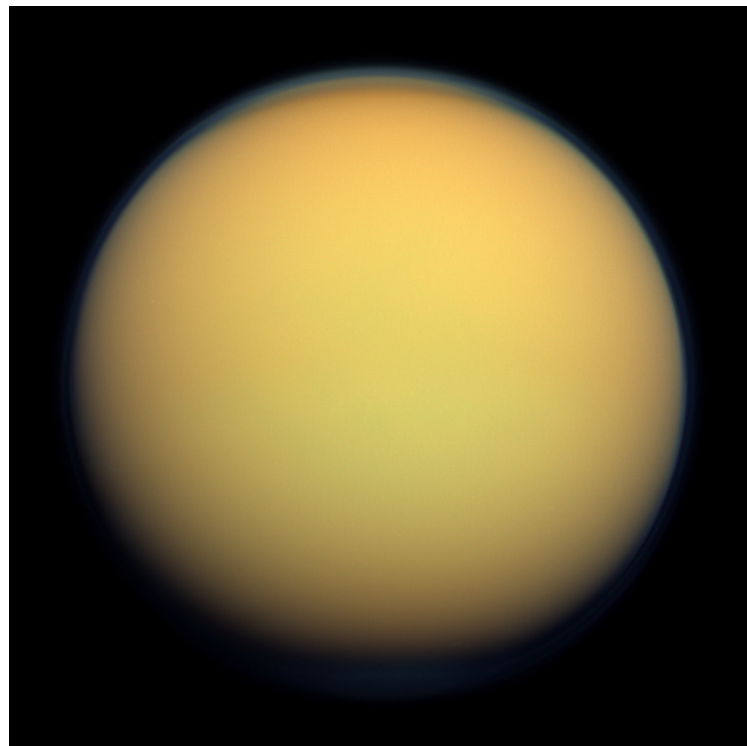


Figure 1.7: Picture of Titan taken by Cassini on 30th January 2012 at a distance of approximately 191,000 km.

Titan is the largest moon of Saturn and the only known moon in the solar system with a dense atmosphere. Since the discovery of the moon by Christiaan Huygens, it has been observed using both telescopes and spacecraft including the Pioneer 11, Voyager 1 & 2 spacecraft and most recently Cassini-Huygens. Data from the Voyager flybys revealed that Titan possessed a thick atmosphere (150 kPa) rich in nitrogen and hydrocarbon compounds (Tyler et al., 1981; Lindal et al., 1983). During Cassini's tour of the Saturnian system between 2004 and 2017, the spacecraft performed over 100 flybys of Titan, taking in-situ measurements of its ionosphere and upper atmosphere. These in-situ measurements helped demonstrate the connection between the ion-neutral reactions that generate large charged molecules in the upper atmosphere and the formation of aerosols (Waite et al., 2005, 2007;

Coates et al., 2007).

1.5.2.1 Atmosphere & Ionosphere

Titan's atmosphere is nitrogen-rich (95-98%) and contains minor species of methane (2-5%) and hydrogen (0.1%). A plethora of trace species exist including hydrocarbons, nitriles and oxygen-bearing molecules such as carbon dioxide and carbon monoxide (Coustenis et al., 2007; Waite et al., 2005).

Noticeable features of Titan's atmosphere are the haze layers that give rise to the moon's orange appearance. The layers are optically thick in most visible wavelengths making remote observations of Titan's surface difficult (Porco et al., 2005). From early experiments using N_2/CH_4 mixtures, a combination of polycyclic aromatic hydrocarbons (PAHs) and polycyclic aromatic nitrogen heterocycles (PANHs) was proposed as the composition of the aerosols that make up the organic haze (Sagan et al., 1993).

Not only is Titan's atmosphere similar to Earth's in regards to being nitrogen-dominated, but also has 4 well-defined atmospheric layers: the troposphere, stratosphere, mesosphere and thermosphere. Due to Titan's lower gravity, these layers stretch over a wider range of altitudes and together create an extended atmosphere. As shown in Figure 1.8, the troposphere stretches up to 40km, the stratosphere from 40 to 300km, the mesosphere from 300 to 490km and finally the thermosphere from 490 km up to the exobase at 1500km. Titan's ionosphere stretches from 900 to 1500km in altitude, with the main production sources being photoionisation by solar UV photons, soft X-ray's and energetic particle precipitation from Saturn's magnetosphere (Bertucci, 2021).

Since 2001 (Kostiuk et al., 2001), Titan has been shown to possess a complicated wind system throughout its atmosphere. This extends from the surface and troposphere up into the upper thermosphere and ionosphere. Early findings found prograde winds throughout the atmosphere, with equatorial wind speeds of up to 160 m/s at altitudes of 300 km in the upper stratosphere (Moreno et al., 2005). The arrival of the Cassini-Huygens mission revolutionised the understanding of Titan's winds, with early measurements finding zonal wind speeds of 245 m/s in the

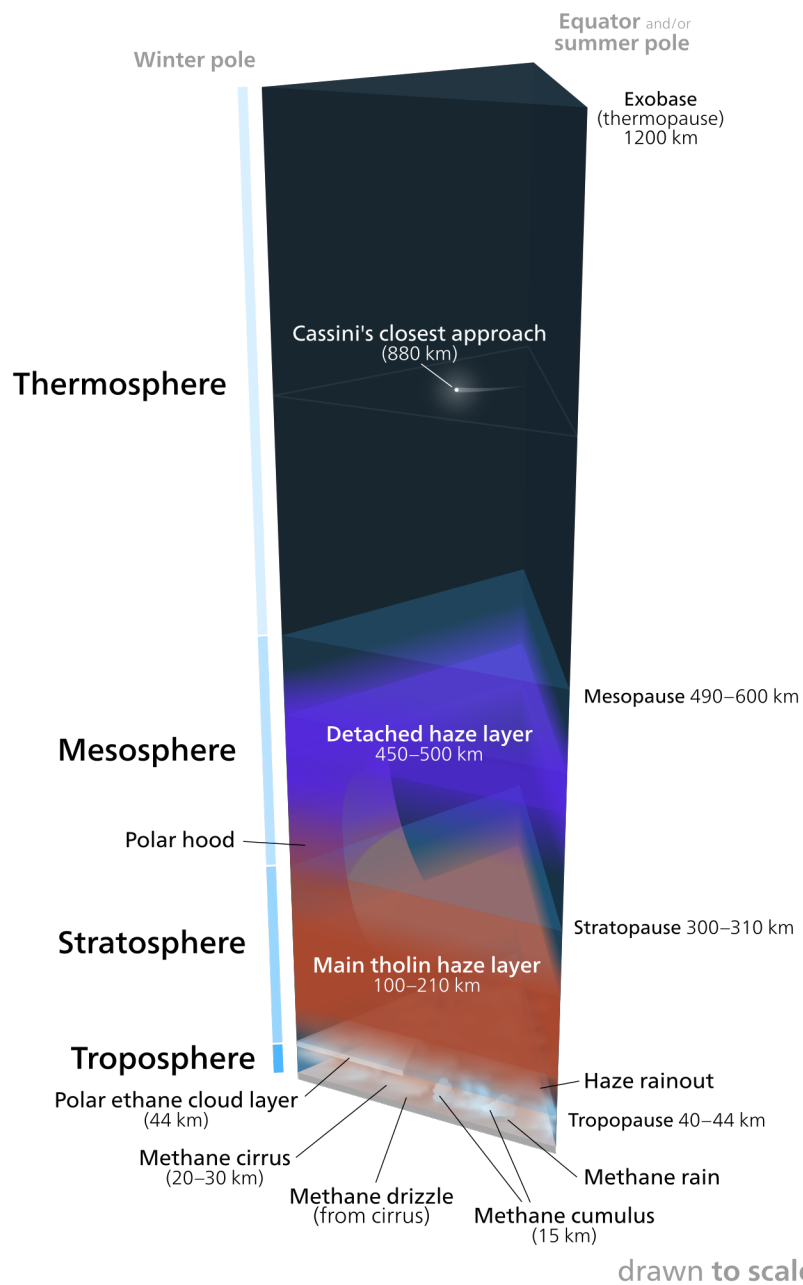


Figure 1.8: Figure demonstrating the various atmospheric layers of Titan.
 [Source: https://commons.wikimedia.org/wiki/File:Titan%27s_atmosphere.svg]

thermosphere, implying the thermosphere could be superrotating (Müller-Wodarg et al., 2006). Measurements of ion wind speeds in the ionosphere were performed by Crary et al. (2009) finding velocities up to 260 m/s. Recently, the use of the Atacama Large Millimeter/submillimeter Array (ALMA) telescope has advanced

the study of winds in Titan's atmosphere, allowing detailed remote sensing observations to take place. Studies utilising this data have found an intense equatorial thermospheric jet with speeds of up to 340 m/s at 1000km (Lellouch et al., 2019).

Furthermore, Titan has important seasonal effects due to Saturn's axial tilt of 27 degrees (Horst, 2017). These seasonal effects can include compositional differences in the atmosphere related to changes in the north-south circulation. Other effects include shifting haze layers, temperature variations and the appearance of the winter polar hood (Horst, 2017).

1.5.2.2 Magnetospheric interaction

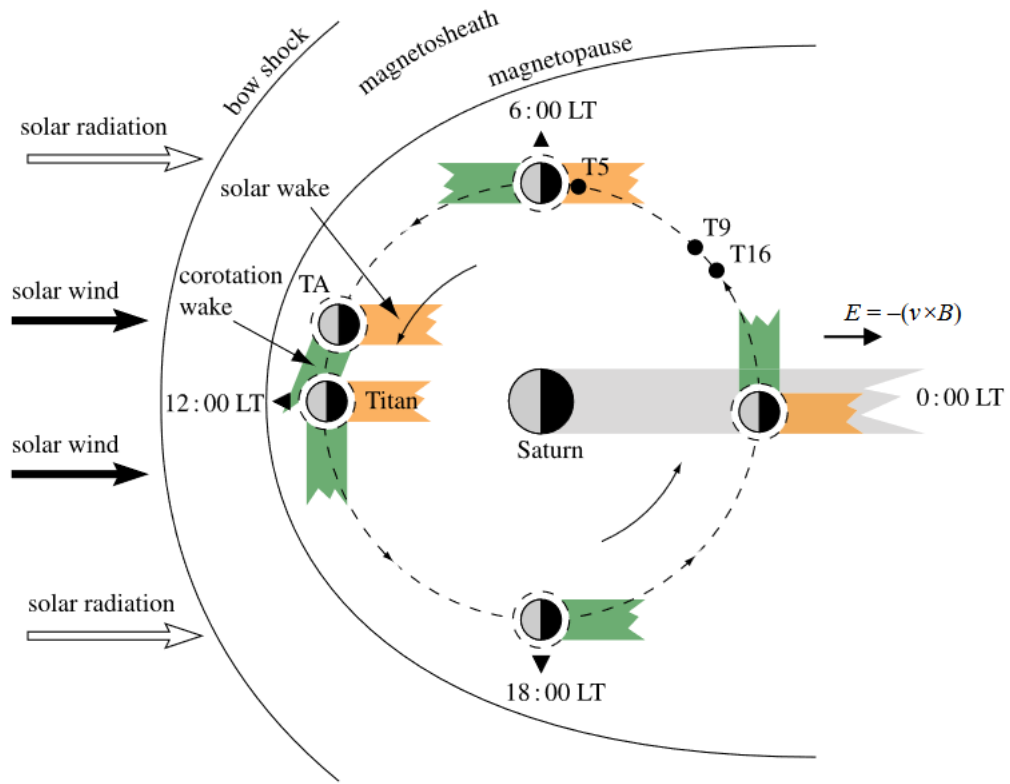


Figure 1.9: Figure demonstrating the different positions of Titan's corotation and solar wakes during its orbit (Coates, 2009).

Titan has no intrinsic magnetic field so its atmosphere is directly exposed to external plasma flows. Titan orbits Saturn at a radius of 20 Saturn radii (R_s), close to Saturn's average magnetopause distance of $22 R_s$. This means that under certain conditions Titan is outside the magnetosphere, in the solar wind. While Titan

is within the magnetosphere it undergoes a high variable interaction with the Saturnian plasma, but always forms a well-defined induced magnetosphere (Bertucci, 2021). This creates several features in the local plasma environment around Titan, including a decrease of the plasma flow speed due to mass loading of the plasma by ionospheric ions. The magnetic field in the flow pile ups and drapes around Titan. In Titan's tail two magnetic lobes are created separated by a neutral sheet. The tail is also where most of the plasma escape from Titan occurs.

Due to the plasma having a higher velocity than Titan, Titan's corotation wake precedes it. Furthermore, due to Titan's orbit around Saturn, the relative orientations of the corotation wake and solar wake can be at any angle, all the way from the two wakes being aligned to being oppositely directly, as shown in Figure 1.9

1.6 Thesis outline

Here I will outline the remaining chapters of this thesis. Chapter 2 covers the instrumentation and theory regarding the Cassini Plasma Spectrometer, which was the primary instrument used for the studies. Chapter 3 covers a study investigating the velocity characteristics of water ion populations inside the Enceladus plume. Chapter 4 investigates the composition of heavy positive ions in Titan's ionosphere. Chapters 5 and 6 investigate ion velocities and spacecraft charging in Titan's ionosphere from in situ measurements. Chapter 7 summarises the conclusions of the studies and suggests directions for future work.

Chapter 2

Methods and Instrumentation

This chapter briefly covers electrostatic analysers and the necessary theory to understand their measurements. Specifically, the Cassini Plasma Spectrometer instrument package is covered, which is used in all research chapters in this thesis.

2.1 Electrostatic analysers

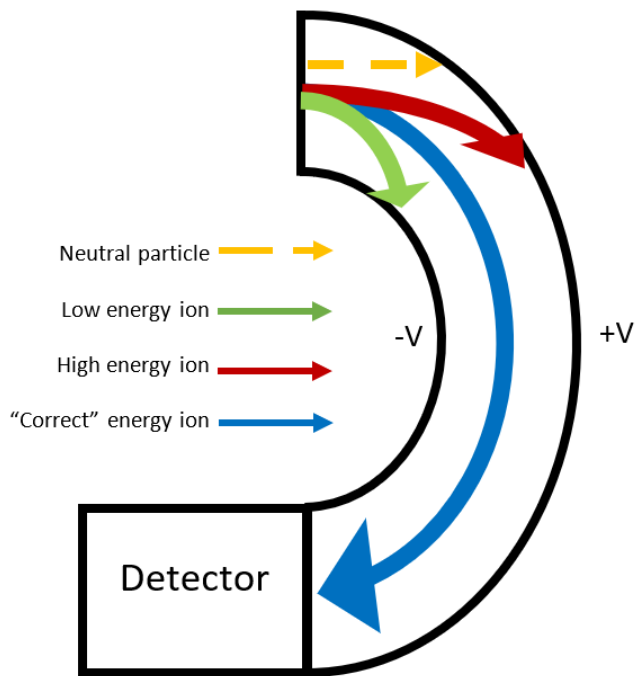


Figure 2.1: Cartoon showing the operation of an electrostatic analyser and how particles with different charges and energies pass through it.

Electrostatic analysers are a type of instrument that utilise ion optics to make

energy per charge measurements of charged particles. They operate by allowing particles in through an aperture that leads to two curved electrodes. The electrodes are set at different potentials creating an electric field between them. Depending on the strength of the electric field, the trajectories of particles with different energies are bent different amounts. At the other end of the electrodes there is a particle detector. For a given electric field, only particles of a specific energy will pass through the electrodes to the detector, Figure 2.1 illustrates this.

2.2 The Cassini-Huygens mission

Cassini-Huygens was a mission to explore the Saturn system, including study of the planet, its rings and moons. It was a joint mission of the National Aeronautics and Space Administration (NASA), European Space Agency (ESA) and Italian Space Agency (ASI). The mission launched in 1997 and arrived at the Saturn system in 2004 before spending 13 years exploring the system until its planned deorbiting into Saturn's atmosphere in September 2017. The spacecraft carried a full scientific suite, with a range of optical instruments from UV through to infrared, fields and particle sensors as well as radars. Huygens was an atmospheric entry probe carried by the Cassini spacecraft. It landed on Titan in January 2005 becoming the first spacecraft to land on Titan.

2.3 Cassini Plasma Spectrometer (CAPS)

The Cassini Plasma Spectrometer (CAPS) was one of Cassini's instruments which studied ions and electrons using three electrostatic analyzers. The instrument was mounted on an actuator which increased its field of view by allowing it to observe different azimuths. CAPS was in operation up to 2011 and for a short time during 2012. The three CAPS sensors were the Electron Spectrometer (ELS), Ion Mass Spectrometer (IMS) and the Ion Beam Spectrometer (IBS), a diagram of the sensors is shown in Figure 2.2. A detailed description of the instrument can be found in Young et al. (2004).

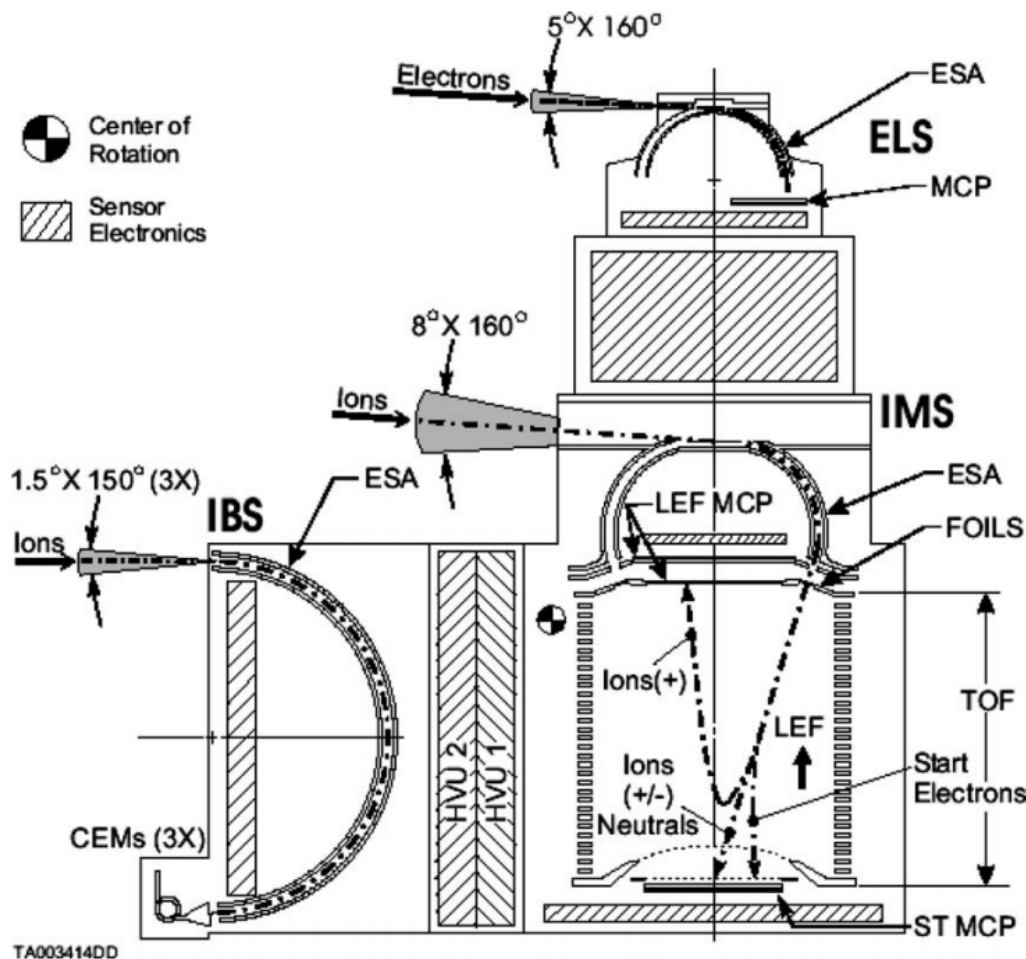


Figure 2.2: Diagram outlining CAPS sensors from Young et al. (2004).

2.3.1 Electron Spectrometer (ELS)

The CAPS Electron Spectrometer (ELS) was a hemispherical top-hat electrostatic analyser (Linder et al., 1998; Young et al., 2004). It was designed to measure a range of electron energies, from thermal electrons at Titan, as well as more energetic trapped electrons and auroral particles (Young et al., 2004).

ELS had eight anodes spread across the elevation direction, with the centre of each anode spaced 20 degrees apart. Each anode had an angular resolution of 20 degrees at Full Width Half Maximum (FWHM) in the elevation direction. The CAPS actuation was in the azimuthal direction and the angular resolution of ELS in this direction was 5.2 degrees at FWHM. The anodes combined create a total instantaneous Field-Of-View (FOV) of $5.2^\circ \times 160^\circ$ in the azimuth and elevation

directions respectively.

ELS was designed to measure electrons with energy/charge ratios from 0.58 eV/q to 28 keV/q, with an energy resolution $\frac{\Delta E}{E} = 0.167$ at FWHM. ELS had 64 voltage levels, all of which, apart from the lowest energy steps, were logarithmically spaced to match the energy resolution of ELS.

2.3.2 Ion Mass Spectrometer (IMS)

When particles entered the CAPS Ion Mass Spectrometer (IMS) they passed through a top-hat electrostatic analyser similar to ELS. Unlike ELS where the particles immediately impacted the microchannel plate detectors after the electrodes, IMS had a Time-Of-Flight (TOF) section, seen labelled in Figure 2.2. The TOF section contained a linear electric field which aided in the separation of ions, neutrals, electrons and negative ions. CAPS IMS was designed to measure hot, diffuse magnetospheric plasma in addition to low-concentration ion species. The energy range of the instrument was 1 ev/q to 50 keV/q with an energy resolution of $\frac{\Delta E}{E} = 0.167$ and its FOV was similar to ELS with an instantaneous FOV of $8.3^\circ \times 160^\circ$.

2.3.3 Ion Beam Spectrometer (IBS)

The CAPS Ion Beam Spectrometer (IBS) was designed to determine the velocity of ion beams in Saturn's magnetosphere and the solar wind, in addition to studying Titan's upper atmosphere during flybys (Young et al., 2004). IBS was a curved-electrode electrostatic analyzer in contrast to the other CAPS sensors that were top-hat analyzers. It consisted of three apertures offset by 30° to each other in the view direction, each with a FOV of $1.5^\circ \times 150^\circ$. The crossed-fan geometry of IBS allowed for the determination of 3-D plasma velocity space distributions. The apertures led to spherical electrodes that extended 178° from the aperture, which the particles passed between before impacting on channel-electron multipliers. The energy range of IBS was similar to IMS from 1 ev/q to 50 keV/q but its energy resolution of $\frac{\Delta E}{E} = 0.014$ was more than an order of magnitude higher than IMS.

The response of IBS was investigated through simulation and testing during the manufacturing and calibration of the instrument (Vilppola et al., 1993, 1996,

2001). Vilppola et al. (2001) described some of the calibration of the IBS sensor, including a reported 3.1 degrees FWHM in the azimuthal direction. They also report a misaligned inner hemisphere and a larger than design value analyzer gap.

2.3.3.1 Actuator

CAPS was mounted on a rotating platform, known as the CAPS actuator, that allowed it to rotate 208 degrees around an axis parallel to the spacecraft's Z-axis at a speed of 1 degrees/sec (Young et al., 2004), named the azimuthal direction in the CAPS instrument frame. The range however was restricted to -80 degrees to +104 degrees, as below -80 degrees FOV encroachments occurred. At 0 degrees, the actuator was aligned with the spacecraft -Y axis and at 90 degrees it was aligned with the Ion and Neutral Mass Spectrometer (INMS) and Magnetospheric Imaging Instrument(MIMI)/Charge Energy Mass Spectrometer(CHEMS) instruments along the -X axis. When the actuator was within 12 degrees of the endpoint of a sweep, the actuator decelerated as it reached the endpoint before accelerating in the other direction (Young et al., 2004). There were two limit switches at ± 110 degrees which gave hard stops to the actuator motion, these were used for calibration.

2.4 CAPS measurements of cold plasmas

When Cassini was at a high velocity relative to the cold plasma it was measuring, the ions appeared as a cold supersonic ion beam in the CAPS frame, directed primarily opposite to the spacecraft's velocity vector. In the instrument frame, the ions energies were measured with a kinetic energy associated with the spacecraft velocity as well as other factors such as ion velocities, spacecraft potential and ion temperature. This is described by equation 2.1,

$$E_\alpha = \frac{1}{2}m_\alpha(v_{sc} + v_{along})^2 - Qe\Phi_{sc} + 8kT. \quad (2.1)$$

where E_α is the measured energy of an ion species α , m_α is the ion mass, v_{sc} is the spacecraft velocity, v_{along} is the alongtrack ion velocity, Q is the charge ($Q=+1$ for positive ions, -1 for electrons and negative ions), Φ_{sc} is the spacecraft potential, T is

the ion temperature, e and k are the electric and Boltzmann constants respectively. This equation assumes the ions are singly charged, as electrostatic analyzers do not measure energy but rather energy per charge ratios.

These previously described conditions mean that the detected energy/charge ratio of the particles can be related to the mass/charge ratio of the particle and by applying this approximation an eV/q measurement can be converted to an amu/q measurement. As seen in Equation 2.1 the conversion is affected by the spacecraft velocity and spacecraft potential. The temperature term has been dropped in Equation 2.2 due to its negligible effects in cold plasmas. The potential energy shift must be performed in phase space density to satisfy Liouville's theorem (e.g. Lewis et al. (2008)), which states that the phase space density of a distribution must be conserved along the trajectory of the system.

$$\frac{m}{q} = \frac{2}{q(v_{sc} - v_i)^2} (E + Q\Phi_{sc}) \quad (2.2)$$

This technique has been previously used at Titan (Coates et al., 2007; Crary et al., 2009; Desai et al., 2017) and at Enceladus (Jones et al., 2009; Coates et al., 2010a; Hill et al., 2012).

2.5 Spacecraft charging

When a spacecraft is immersed in a plasma it gains a potential relative to the surrounding plasma due to a current balance between itself and the plasma. The final potential can be positive or negative relative to the plasma and results from a combination of different charging mechanisms, for example: the incident ion current, incident electron current, photoelectron current and secondary electron currents (Whipple, 1981).

When the spacecraft has a positive potential relative to the plasma, emitted photoelectrons from the spacecraft's body can be attracted back to the spacecraft and impact on its surface. If the energy of this population can be measured then an estimate of the spacecraft potential can be derived. CAPS ELS can measure the energy of the photoelectrons, providing an estimate of the spacecraft potential,

although during Cassini's tour positive potentials occurred infrequently.

Another method of calculating spacecraft potential involves using positive and negative ion measurements in certain environments. By using known and estimated parameters such as ion mass and ion velocity, spacecraft potentials can be derived by examining the observed energy of the ions.

Langmuir probes can provide estimates of the spacecraft potential for both positive and negative charging. A typical Langmuir single probe operates by charging the probe to either a constant or time-varying electric potential. By using a time-varying electric potential, the charge-voltage characteristics of the surrounding plasma are measured and a spacecraft potential can be inferred.

Chapter 3

Fast and Slow Water Ion Populations in the Enceladus Plume

This chapter is a modified version of a paper published in the *Journal of Geophysical Research: Space Physics* with the full citation:

Haythornthwaite, R. P., A. J. Coates, G. H. Jones, & J. H. Waite, Fast and Slow Water Ion Populations in the Enceladus Plume, *Journal of Geophysical Research: Space Physics*, Volume 125, Issue 2, article id. e27591, doi:10.1029/2019JA027591, 02/2020

3.1 Introduction

One of the most startling finds of the Cassini mission was the discovery of a water plume emanating from Enceladus's south pole (Dougherty et al., 2006). The plume's composition is dominated by water, confirmed by INMS (Waite et al., 2009), Ultraviolet Imaging Spectrograph (UVIS) (Hansen et al., 2006) and CAPS (Tokar et al., 2009; Coates et al., 2010a) measurements. The plume was found to originate from diffuse sources and collimated geyser-like jets. The jets were associated with a series of 4 fissures, commonly known as the "Tiger Stripes", that dominate the south polar terrain. The plume fly-throughs thereby allowed direct sampling of the ocean material providing an insight into the physics and chemistry present in the subsurface ocean.

It is well established that water is the major constituent in all three plume

phases: dust, gas and ions. The gas consists of neutral molecules with H₂O comprising up to 98% with other major species being CO₂, CH₄, NH₃ and H₂ (Waite et al., 2009; Waite et al., 2017; Waite et al., 2019). There are also hydrocarbons, alcohols and nitriles detected at below 0.2% relative abundance to H₂O (Magee and Waite, 2017).

Various CAPS sensors have previously detected ions at Enceladus. CAPS ELS has been used in the detection of negative ions, consisting of primarily water group ions (O⁻, OH⁻) (Coates et al., 2010b) and clusters of these ions, likely in the form (H₂O)_n-OH⁻ or (OH)_n (Postberg et al., 2018b). These clusters were found to extend up to high masses (300-500 amu/q) with inferred densities in the plume between 0.1 and 50 cm⁻³. Similarly, CAPS IMS has complemented these findings with positive ions including H₂⁺, water group ions (O⁺, OH⁺, H₂O⁺, H₃O⁺) and water dimer molecules (H_xO₂) (Tokar et al., 2009). The same study inferred that ion-neutral reactions in the plume plasma as well as charge exchange between magnetospheric ions and plume neutral molecules are major sources of these ions. In situ photoionization has been shown to contribute to the ion population as well (Sakai et al., 2016). H₃O⁺ is understood to be the dominant water group ion, as demonstrated through physical chemistry models of the plume (Fleshman et al., 2010), particle test models (Sakai et al., 2016) and in situ data from the INMS instrument (Cravens et al., 2009).

3.2 Particle Velocities in the Enceladus Plume

The plume gas emission has been shown to contain two distinct water components, a thermal population and a supersonic population (Teolis et al., 2017).

The thermal component arises from molecules interacting with fissure walls or sublimation. The bulk velocities of the neutral water molecules in the plume have been estimated between 500 and 1400 ms⁻¹. These measurements have been derived through various methods such as modelling (Smith et al., 2010; Tenishev et al., 2010, 2014), in-situ measurements (Dong et al., 2011; Teolis et al., 2017) and UVIS measurements (Hansen et al., 2008).

The supersonic water population has been associated with driven fast gas emission from fissures. Some studies have found velocities from 1200 ms^{-1} up to 2600 ms^{-1} (Postberg et al., 2011; Hansen et al., 2011). Through a combination of INMS and UVIS measurements, Teolis et al. (2017) suggested Mach numbers up to 10, corresponding to jet velocities of 6 km^{-1} using a thermal velocity of 576 ms^{-1} . Other fitting attempts such as that performed by Yeoh et al. (2017) used INMS/UVIS data and considered diffuse and jet sources. They found during the E5 flyby narrow jets with velocities in excess of Mach 5 (1500 ms^{-1}) and that vents III, IV and VI were the strongest influences in the fitting. The model by Tenishev et al. (2014) fitted bulk velocities to the 8 vents found by Spitale and Porco (2007), finding a range of velocities between 580 and 1338 ms^{-1} .

There have also been attempts to model ion velocities inside the plume. Kriegel et al. (2011) modeled an ion bulk velocity less than 1 kms^{-1} inside the plume. Other modelling work by Sakai et al. (2016) modelled velocities between 1 and 3 kms^{-1} .

3.3 Methodology

In this study I present data from all three of the Cassini Plasma Spectrometer (CAPS) sensors (Young et al., 2004): the Electron Spectrometer (ELS), Ion Mass Spectrometer (IMS) and Ion Beam Spectrometer (IBS). For details on these sensors, see Section 2.3.

This study consists of CAPS measurements of cold plasmas and the derivation of the alongtrack ion velocity term. The techniques used in these measurements are covered in Section 2.4.

There are extra caveats to using ELS as a negative ion mass spectrometer and further treatment of the data is required. This is due to electron counts from various populations such as magnetospheric electrons and photoelectron peaks being present (Coates et al., 2013; Taylor et al., 2018). As stated previously, the ions appear as a highly directed supersonic population travelling at Cassini's velocity in ELS, this means the negative ions only appear in the central anodes of the sensor. The central anodes or ram anodes were typically the fourth and fifth anodes

during encounters due to the spacecraft attitude and CAPS being actuated so that Cassini's velocity vector was between the two anodes. To reduce the possibility that the detected peak is associated with an electron population an assumed background isotropic electron distribution was found by averaging over the non-ram anodes (anodes 1-3 and 6-8) (Wellbrock et al., 2013; Desai et al., 2017). This background was then subtracted off the ram anodes to isolate the negative ion signal. The remaining peaks in the spectrograms after this background removal are interpreted as negative ion peaks.

3.4 Results

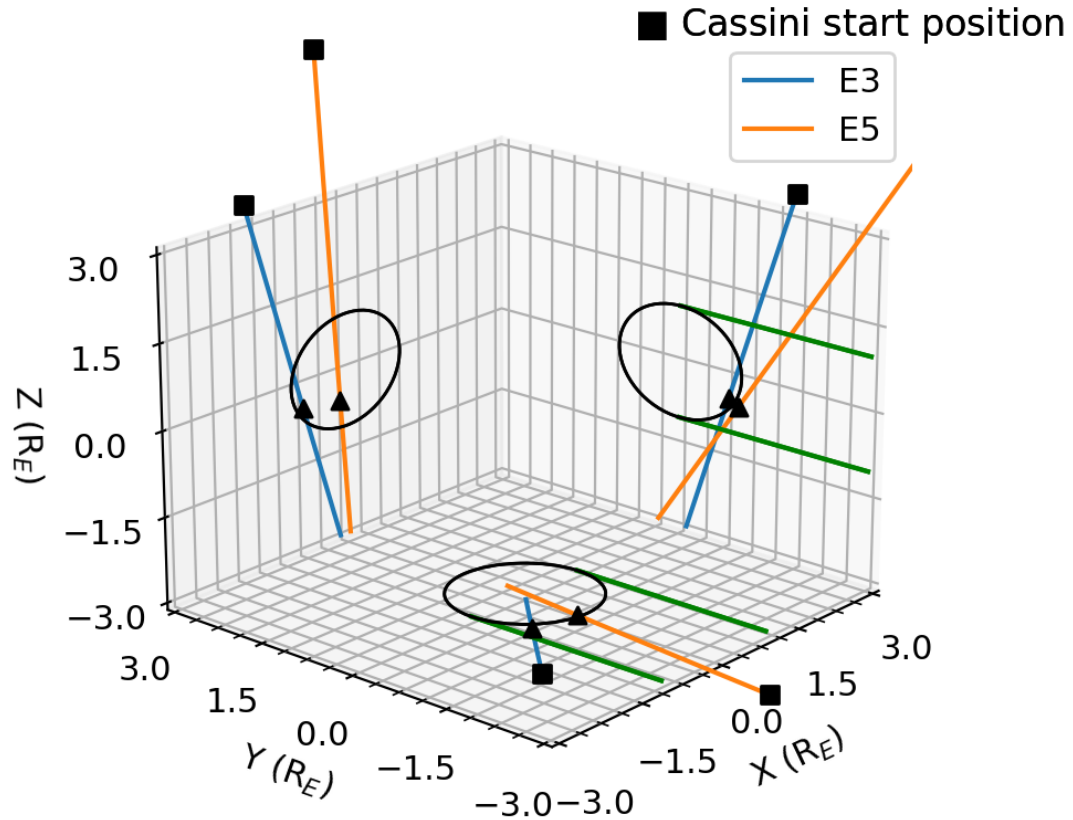


Figure 3.1: An overview of the trajectories of the Enceladus flybys studied in the Enceladus frame. The closest approaches are shown with triangles. The Cassini start position helps indicate Cassini's direction of travel. Both the E3 and E5 flybys were -Z directed flybys. The geometric corotational wake of Enceladus is indicated by the green lines.

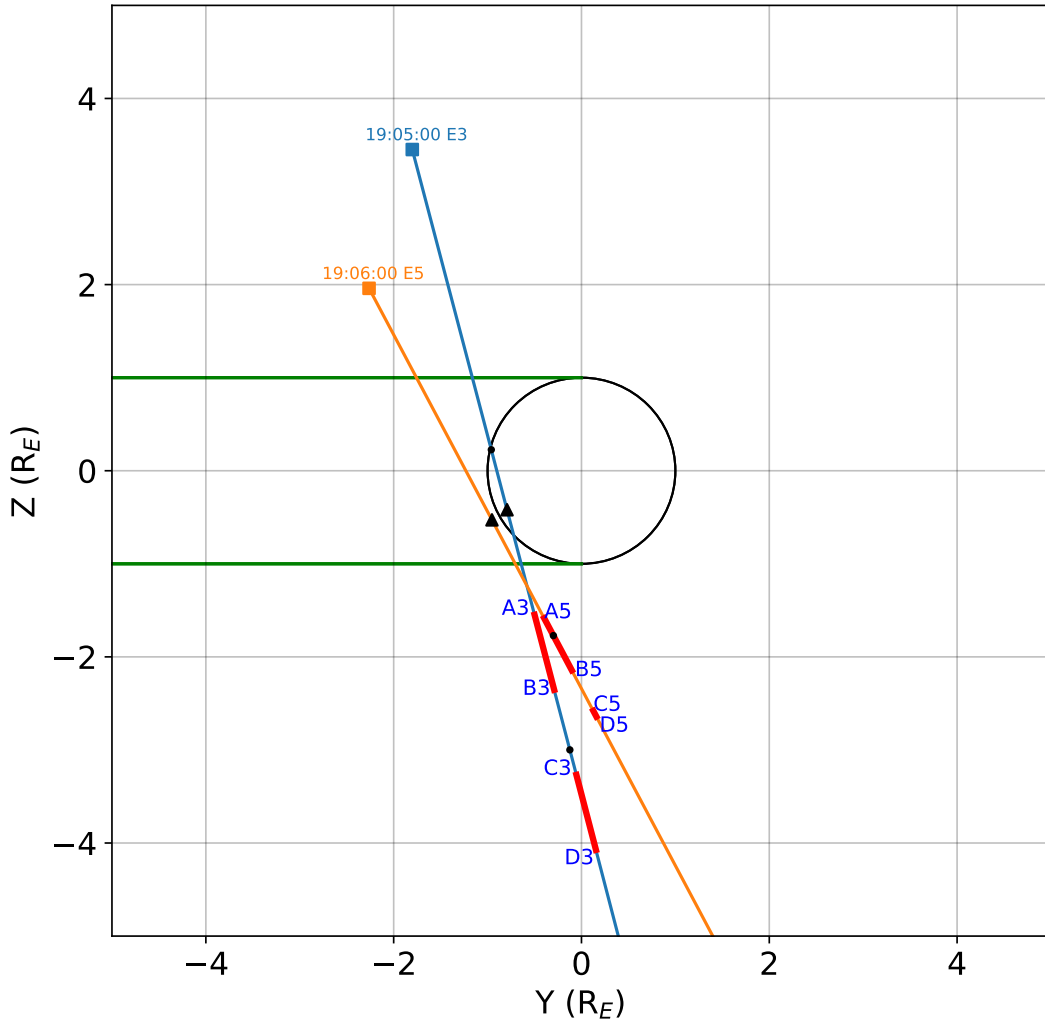


Figure 3.2: The Cassini trajectory in the YZ plane during the E3 and E5 flybys. Negative Y is in the direction of the corotation of magnetospheric plasma. The highlighted red areas of the trajectories between the labels A#-B# and C#-D# where # is 3 or 5 correspond to the E3 and E5 flybys respectively, are the regions where the low energy peak occurs in the energy spectrograms. Similar labels can be found in subsequent figures. The squares indicate an arbitrary start location to help demonstrate the north-south direction that Cassini traveled in, the black triangle indicates the location of closest approach, while the dots indicate Cassini's location at 1 minute intervals. The geometric corotational wake of Enceladus is indicated by the green lines.

3.4.1 E5 Flyby

E5 was a targeted Enceladus flyby that took place in October 2008. It was the fastest flyby at 17.7 km/s and the closest with a closest approach of 25km. The -Z trajectory of the flyby, as seen in Figures 3.1 and 3.2, meant it followed along the plume motion as the ejecta move in a negative Z direction away from Enceladus.

3.4.1.1 E5 Positive Water Ions

Positive ions during the E5 flyby have been previously studied by Tokar et al. (2009) using CAPS-IMS.

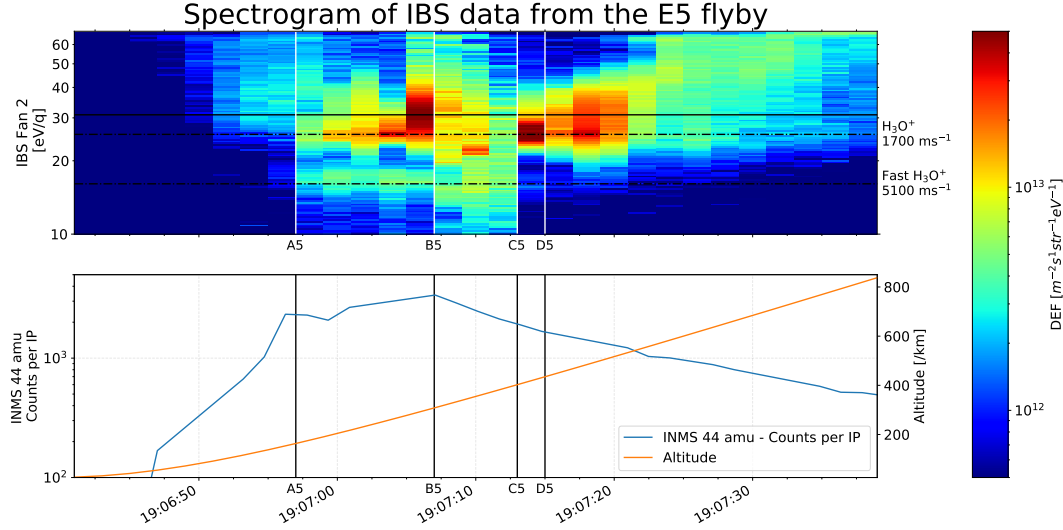


Figure 3.3: The first panel is an energy spectrogram from IBS fan 2 during the E5 flyby. This has energy plotted on the y-axis, time on the x-axis and differential energy flux (DEF) shown by the colour. Horizontal lines demonstrate the energy location of the presumed major water ion H_3O^+ , with the solid line displaying the energy location when assumed to be stationary in the plume frame, while the dot-dashed lines displays the molecules positions with an along-track velocity away from Cassini and a constant spacecraft potential taken into account. Fast H_3O^+ fits a velocity of 5.1 km s^{-1} , while the main H_3O^+ population fits a velocity of 1.7 km s^{-1} . The second panel plots 44 amu neutral counts/IP from the INMS instrument, see Perry et al. (2015) for details. In addition Cassini's altitude above the Enceladus surface is plotted.

An energy-time spectrogram displaying data from fan 2 of CAPS IBS during the E5 flyby can be seen in Figure 3.3. The main intensity peak seen in the spectrogram can be associated with the dominant ion species present in the plume, the water group ion H_3O^+ . The secondary lower energy peak that occurs at 19:06:55 is the subject of interest in this study. The background ions drop out occurs at 19:06:37, along with an intensity peak that decreases in energy from 19:06:45 to 19:06:55 (prior to the A1 label). As noted by Tokar et al. (2009), this peak is associated with H_3O^+ being formed in the plume that is gradually accelerated and dragged into the magnetospheric wake.

At the B5 location in Figure 3.3 the energy peak structure can be seen to break

down when Cassini is directly over the south polar region of Enceladus. As confirmed by INMS measurements seen in the lower panel of Figure 3.3, Cassini is in the densest region of the plume at this point. The sweeps between B5 and C5 lack clear peak structure, this could be due to masking from dust grain impacts in the instrument creating anomalous peaks, as this is when Cassini traversed a more active (Yeoh et al., 2017) and higher dust-to-gas ratio region (Hedman et al., 2018). Another possible cause of the peak structure disruption in the B5-C5 energy sweeps could be the time-aliasing of the instrument in the highly dynamic plume environment. Despite the possible instrument effects, the low energy peak appears to shift to a lower energy in the first sweep after B5, this could be indicative of an increase in ion velocity due to Cassini passing through the middle of a high-velocity jet.

The horizontal lines in Figure 3.3 indicate energies of various molecules with different characteristics, the energies of which have been determined using Equation 2.1. I note that previous spacecraft potential discrepancies found between CAPS and the Radio and Plasma Wave (RPWS) Langmuir probe (LP) range between 0.5 to -2 V (Coates et al., 2007; Schippers et al., 2009; Desai et al., 2017) and that the LP potential varies from -0.43 to -1.27 V during the E5 encounter. However if a positive spacecraft potential existed due to discrepancies, positive ion energies would be reduced. If spacecraft potential is solely considered to explain the low energy peak seen in Figure 3.3, a positive voltage of +5 V would be needed to explain the H_3O^+ peak. This would be an order of magnitude larger than previous reported discrepancies and would affect both energy peaks in a similar fashion, therefore this explanation is unlikely. Furthermore if spacecraft potential is solely considered, the energy offset would also affect CAPS ELS data by increasing the negative ion energies but this effect is not observed.

This requires another mechanism to explain the low energy peak seen in the plume.

3.4.1.2 Ion Velocities

If a velocity component exists along Cassini's trajectory, it affects the measured energy/charge ratio of the particles. Previously used mass-energy conversions for

CAPS have considered ions at rest relative to Enceladus implying that in the Cassini frame (Tokar et al., 2009; Coates et al., 2010a), the particles are moving towards CAPS at the spacecraft ram velocity. If a non-zero velocity exists in the Enceladus frame there can exist an ion velocity component along the Cassini trajectory. A velocity component pointing away from Cassini would result in the reduction of the relative velocity between Cassini and the ions, adding the ion velocity term in Equation 2.2.

Reducing the relative velocity of the molecules results in the molecules appearing at lower energies. As seen in Figure 3.3, correcting with a constant spacecraft potential and applying an ion velocity of $\sim 1700 \text{ ms}^{-1}$ results in the major peak in the spectrogram aligning with the expected H_3O^+ peak. Applying the same method to the lower energy peak requires an ion velocity of $\sim 5100 \text{ ms}^{-1}$.

	E3	E5
Slow H_3O^+	[200, 2000]	[1400, 2200]
Fast H_3O^+	[2300, 4800]	[4550, 5800]
Slow OH^-	[-1800, -300]	[-1600, 450]
Fast OH^-	-	[3000, 5000]

Table 3.1: The velocity ranges of positive and negative ions in ms^{-1} for the two Enceladus flybys examined. The ranges result from spacecraft potential discrepancies and the energy resolution of the CAPS sensors. E3 H_3O^+ velocities are calculated from IMS data while E5 H_3O^+ velocities are calculated from IBS data. ELS is used for both E3 and E5 in the OH^- ion velocity determination.

Table 3.1 contains the ranges of velocities that could account for the peaks seen in the CAPS sensors. This has been applied across the entire plume encounter which is likely incorrect as variations in the velocity would be expected during the encounter, this likely effect can be seen when the lower peak at 19:07:07 shifts to lower energies. However determining the velocity on a sweep-by-sweep basis has not been attempted, due to a lack of detailed information on the spacecraft potential at the same temporal resolution.

3.4.1.3 Peak-Source Correspondence

Jones et al. (2009) found correspondence between dust peaks seen in CAPS ELS and IMS spectrograms and the reported jet sources in the fissures (Spitale and Porco,

2007). By applying the vent findings from Jones et al. (2009) I find that the start of the lower energy peak at 19:06:57 matches the E5i1 peak (see Jones et al. (2009)), which was associated with vent V. This vent was assigned a bulk velocity of 1030 ms^{-1} by Tenishev et al. (2014). However, this assignment does not concur with the results of Yeoh et al. (2017), as they find vent III to be the major source. Assuming the vent V assignment is correct it implies the ion velocity is 570 ms^{-1} higher than the neutral bulk velocity but this still lies in the range reported by Hansen et al. (2011). Furthermore plume ions could be accelerated outwards by electric fields in the plume (Jones et al., 2009; Farrell et al., 2010; Sakai et al., 2016), possibly up to several kms^{-1} .

There is also the possibility that the associated source is not one of the earlier reported vents but one of the 98 jets later identified by Porco et al. (2014). Teolis et al. (2017) studied three flybys in 2010-2011 that were low altitude horizontal flybys. Using optical and ultraviolet images, as well as 3D modelling, they constrained the magnitudes and velocities of the jets detected using high spatial resolution measurements from INMS. They found large variability in the derived velocities between flybys as well as along the fissures. They also found that the jets contained a mixture of low and high velocity gas emissions, with gas being accelerated up to Mach 10. In their modelling they used the 98 jets from Porco et al. (2014) and found that some of the jets corresponded well with high velocities seen in INMS. Contributions from the 98 jets is not considered in this work due to the lack of spatial information in the data, possible mixing from multiple jets, and temporal variability.

In Figure 3.4, a break in the occurrence of the peak can be seen corresponding to the interval 19:07:07-19:07:13. This interval also corresponds to Cassini's passage over the south pole and the Baghdad fissure. Jones et al. (2009) identified a positive nanograin peak between 19:07:09 and 19:07:13, originating from the nearby vent VI. This leads to the interpretation that charged nanograins or neutral dust are affecting IBS during this timeframe and obscuring the peak structure.

A similar effect does occur at the Cairo fissure crossing but not at the same

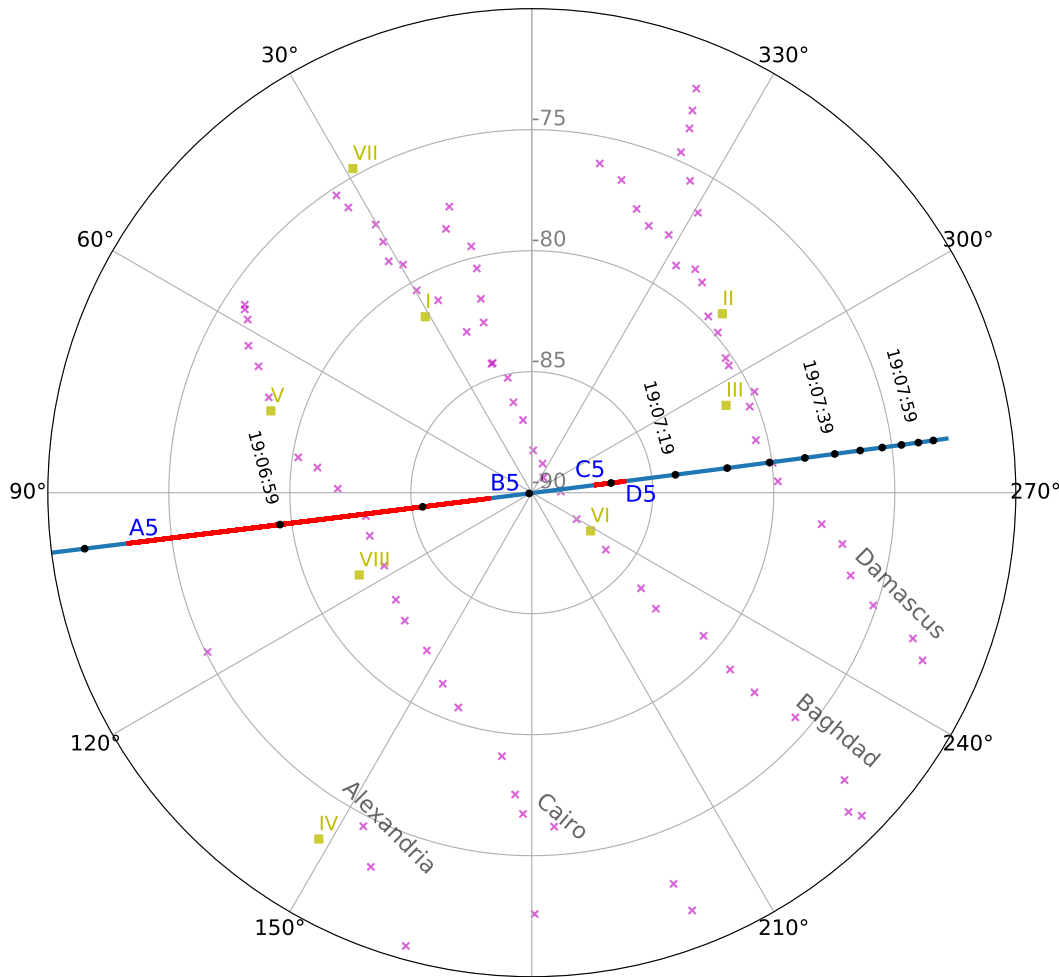


Figure 3.4: Diagram of the E5 flyby surface track over the south polar fissures. Black dots on the track are markers spaced at 5-second intervals. Yellow squares indicate the vent locations as identified by Spitale and Porco (2007) whilst pink crosses indicate the jet sources from Porco et al. (2014). The red regions of the surface track are the times where the low energy peak can be seen (19:06:55-19:07:07, 19:07:13-19:07:15).

intensity. The main water peak broadens and the lower peak is weakened during the 19:07:01-19:07:03 IBS sweep. The lower intensity could be due to a reduced dust-gas ratio at the Cairo fissure compared to Baghdad (Hedman et al., 2018), it could also be due to less active jets (Yeoh et al., 2017).

3.4.1.4 E5 Negative Water Ions

As described in section 2.4, the CAPS Electron Spectrometer (ELS) can be used as an anion spectrometer when viewing a highly directed negative ion population. Negative ions were previously studied in the Enceladus plume by Coates et al.

(2010a,b). During these studies the negative ions were assumed to be stationary relative to Enceladus.

Applying similar methods to that performed with the positive ions, velocities of negative ions during the E5 flyby are found using ELS data. A spectrogram of ELS data can be seen in Figure 3.5. During the E5 flyby a range of velocities are found for the OH^- ions, between -1600 ms^{-1} to 450 ms^{-1} and therefore agree with the assumption of stationary or nearly stationary ions. This negative ion population is likely associated with the slower neutral population due to its low velocity.

A tentative low energy peak appears once the isotropic electron background is removed. As the peak exists at the upper energy range of the electron energies the detection of a low energy negative ion peak is tentative. If this low energy peak is associated with fast moving OH^- ions, its resulting velocity would be between 3000 and 5000 ms^{-1} . Similar to the positive ions this peak could be associated with the fast neutral population. The velocities of the negative ions appear to be lower than the positive ions, implying a deceleration of the negative water ions once the neutral water molecules are ionised

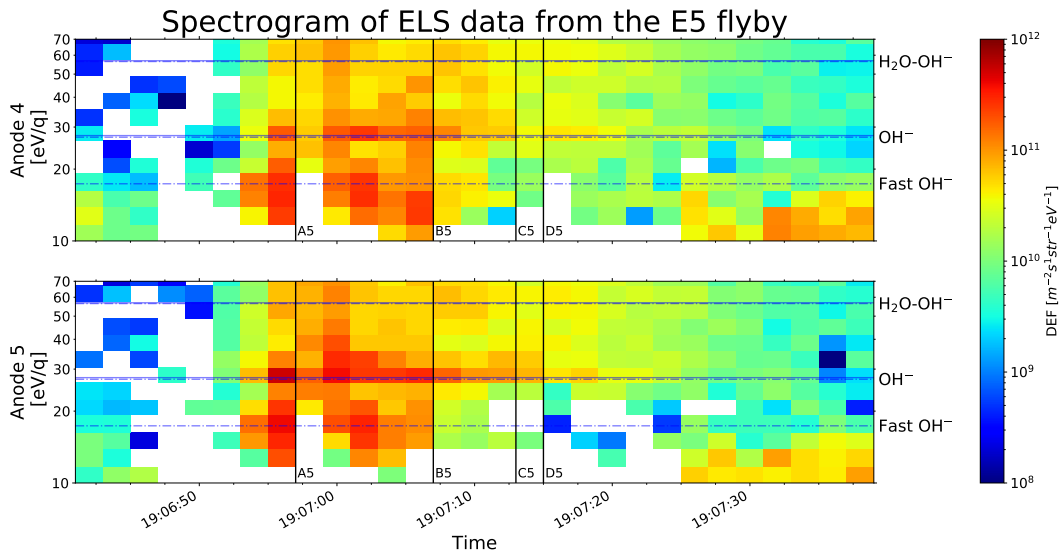


Figure 3.5: Energy spectrogram of the ELS ram anodes (Anodes 4 and 5) during the E5 flyby. An isotropic electron background calculated from the mean of the non-ram anodes has been removed. The lines represent energies of various molecules, dot-dashed lines represent ions with the same mass with spacecraft potential and different ion velocity corrections applied.

3.4.2 E3 Flyby

As seen in Figure 3.2, E3 was another targeted Enceladus flyby and took place before E5 in March 2008. It had a similarly inclined -Z trajectory to E5 and a comparable velocity of 14.4 kms^{-1} .

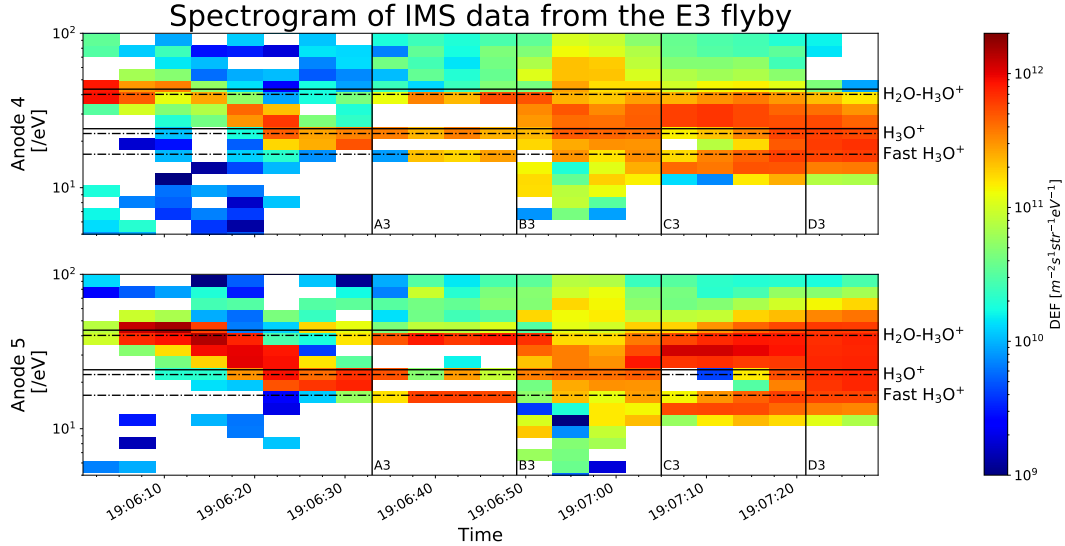


Figure 3.6: Energy spectrogram of the IMS ram anodes (Anodes 4 and 5) during the E3 flyby. Horizontal lines indicate energy locations of various molecules, solid lines indicate the location of an entirely stagnated flow without corrections, whilst the dot-dashed lines indicate the locations with spacecraft potential and ion velocity corrections applied.

3.4.2.1 E3 Low Energy Peak

During the E3 flyby CAPS IBS was operating in a high energy mode, resulting in ions below 80 eV not being detected, therefore it cannot be used in this study. However another sensor in the CAPS instrument package can be used, the Ion Mass Spectrometer (IMS). During the E5 flyby no rammed ion peak occurs consistently across consecutive energy sweeps in the CAPS IMS instrument (*not shown here*). A possible cause are dust particles or neutral molecules impacting CAPS that proceed to vaporise and ionize in the instrument, this could cause anomalous energy peaks that mask the rammed ion peak. This possibility would be consistent with the higher velocity of E5 compared to E3, along with the increased neutral gas density (Perry et al., 2015) and dust density (Teolis et al., 2010) of E5 compared to E3.

Unlike E5, CAPS IMS observed positive ions during the E3 flyby and as seen

in the IMS energy-time spectrogram in Figure 3.6, three rammed ion peaks occur inside the plume. These peaks have been previously studied by Tokar et al. (2009), with the peaks being attributed to O^+ , H_3O^+ and a water dimer ion.

The low energy peak appears after the energy of the main water group peak becomes constant, at around 19:06:30. The lower energy peak also appears in conjunction with the emergence of the dimer peak. The timing of the low energy peak is similar to the peak emergence in the IBS data for the E5 flyby.

Examining the energy locations of molecules, a faster water group ion explains the presence of the low energy peak. The spacecraft potential during the E3 flyby is approximately -3 to -4 V, as measured by the RPWS Langumir probe, and this shifts the positive ions to higher energies. If this effect is taken in isolation, then the energy locations of the detected peaks would not be associated with water group ions. Therefore ion velocities are taken into account, to reduce the energy of H_3O^+ to align the slow population with the major peak and the fast population with the low energy peak. The combination of these corrections leads to: 1) H_3O^+ and the water dimer are slowly moving ions, 2) the energy of slow moving O^+ is between the two lower peaks, 3) the lower energy peak must be associated with a faster water group ion population.

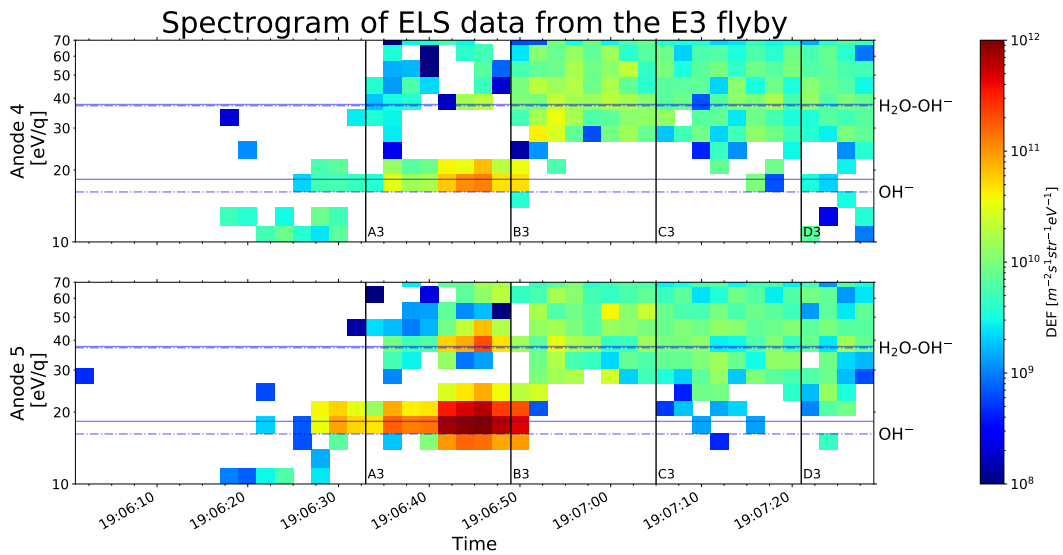


Figure 3.7: Spectrogram using ELS data from the E3 flyby, similar annotations to Figure 3.5

3.4.2.2 E3 Negative Water Ions

Similar to E5 negative ions are seen during the E3 flyby. The spectrogram for the E3 flyby can be seen in Figure 3.7.

The lack of a negative ion peak associated with a faster water ion group during the E3 flyby could be due to several factors. Firstly, the peak could be obscured by the electron background present in the plume. Secondly, the production rates of negative ions are low compared to positive ions, therefore the peak intensity may be too low to register.

3.5 Discussion

The low energy peak is only seen in the E3 and E5 -Z directed flybys and not the later E7, E17 and E18 flybys which traversed in the XY plane through the plume, as shown in Figure 3.8. This implies that the geometry of the flyby is significant and supports the interpretation of a highly directed fast water ion population.

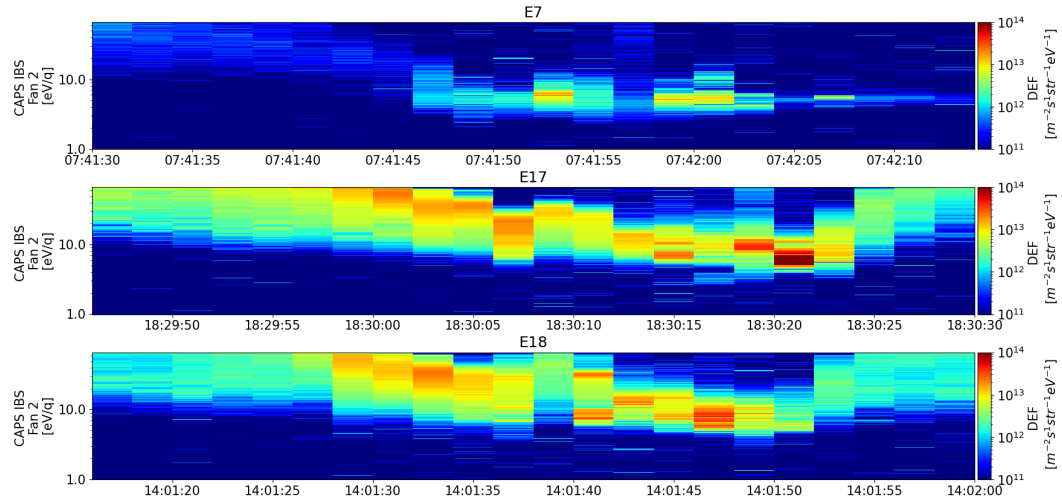


Figure 3.8: Spectrograms of IBS data gathered during the E7, E17 and E18 flybys. Comparing to the E3 and E5 flybys, no consistent second energy peak can be seen across adjacent sweeps.

The variation of measured ion velocities between the flybys can be attributed to the different geometry of the flybys. The Y velocity component of the E5 flyby was just over 50% of the Z velocity component, whilst at E3 it was just under 25%. This has been previously noted in modelling work by Sakai et al. (2016). This

difference in the relative components could explain the velocity discrepancies as CAPS sensors can only measure along track velocities using the applied method.

The generation of the two water group positive ion populations is likely through charge exchange (Tokar et al., 2009; Omidi et al., 2012; Sakai et al., 2016). Charge exchange is associated with fast moving ions interacting with slow moving neutrals. There is only a small amount of energy transfer to the newly created ion during charge exchange, meaning these ions retain similar kinetic energies to their neutral progenitors. This implies that the two ion populations can be created from two neutral populations with different velocities.

3.5.1 EM-fields

The magnetic field within the plume is largely -Z directed with perturbations due to the plume material (Dougherty et al., 2006). The presence of the magnetic field causes newly created ions to be picked up and gyrate away from Saturn. As magnetic fields cannot do work on particles, the energy difference between the positive and negative ions requires other forces to be present. The origin of these forces could be an ambipolar electric field present within the plume. These fields have been modeled in several studies (Omidi et al., 2012; Sakai et al., 2016). Sakai et al. (2016) proposed an electric field strength of $10 \mu\text{V/m}$ in the -Z direction. A field of this magnitude would both accelerate positive ions and decelerate negative ions in the -Z direction, causing a large velocity component along Cassini's track during the -Z directed E3 and E5 flybys. The longer lifetimes of positive ions compared with negative ions could result in stronger acceleration effects.

Negative ions were presumed to be stationary relative to Enceladus due to the local production and short lifetimes of the molecules. However during the studied flybys a range of valid ion velocities exist (see Table 3.1), where the negative ions would be detected in the same energy bin of ELS. For example during E3 the maximum possible OH^- ion velocity was 1800ms^{-1} , the deceleration caused by an electric field of $10 \mu\text{V/m}$ would be approximately 60ms^{-2} , requiring 30 seconds to achieve the upper limit of possible deceleration. Comparing to the proposed lifetimes in Coates et al. (2010a) of 6 seconds for H^- , this deceleration appears

reasonable given that OH^- lifetimes are likely higher than that of H^- , due to their higher electron affinity providing greater stability and thereby allowing greater deceleration. This could explain the velocities of negative ions during E3, with the required lifetime being between 5 and 30 seconds.

3.5.2 Other Possibilities

Another possibility could be doubly charged ions, resulting in a candidate molecule of 24 amu. Although there are candidate molecules in this mass range which could form doubly-charged particles, they are unlikely in the plume due to the required energetics and their lifetimes being on the order of a few seconds or less (Thissen et al., 2011).

The lower peak being associated with N^+ ions is possible but unlikely. Enceladus has previously been shown to be a major source of nitrogen in Saturn's magnetosphere (Smith et al., 2007, 2008). However this explanation would require the water peak to be associated with OH^+ and multiple reactions from a neutral ammonia source. Given that H_3O^+ is currently considered as the dominant ion and multiple reactions are unlikely, this possibility is not considered further.

3.6 Summary and Conclusions

Ion velocities have been measured in the Enceladus plume, with both fast and slow water ion populations being found. Data from all three CAPS sensors have been utilised across two flybys that occurred in 2008, CAPS IMS data were used during the E3 flyby, while IBS data were examined during the E5 flyby. Two separate positive water ion velocity distributions were found, originating from the two neutral populations within the plume: the slow thermalised emission and the fast gas emission (Teolis et al., 2017). Through processes such as charge exchange these neutral water molecules become ionised and retain their kinetic energy, generating two distinct ion energy peaks within the plume. This interpretation is different from that presented by Tokar et al. (2009) who analysed these peaks as a compositional difference rather than a velocity difference.

Negative ions were also analysed using CAPS ELS data, with ion velocities

nearly stagnant in the plume but decelerated compared to the neutral molecules and positive ions. These findings add to the discussion over the presence of a negative Z directed electric field in the plume, generated through plasma pressure or negatively charged grains (Jones et al., 2009; Sakai et al., 2016).

Chapter 4

Heavy Positive Ion Groups in Titan's Ionosphere from Cassini Plasma Spectrometer IBS Observations

This chapter is an modified version of a paper published in the *Planetary Science Journal* with the full citation:

Haythornthwaite, R. P., A. J. Coates, G. H. Jones, A. Wellbrock, J. H. Waite, V. Vuitton, & P. Lavvas, Heavy Positive Ion Groups in Titan's Ionosphere from Cassini Plasma Spectrometer IBS Observations, *The Planetary Science Journal*, Volume 2, Issue 1, id.26, 13 pp., doi:10.3847/PSJ/abd404, 02/2021

4.1 Introduction

Titan's atmosphere is nitrogen-rich and contains minor species of methane and hydrogen along with a plethora of trace species including hydrocarbons, nitriles and oxygen-bearing molecules such as carbon dioxide and carbon monoxide (Coustenis et al., 2007; Waite et al., 2005). The oxygen-bearing molecules are thought to originate from O⁺ ions and micrometeorites entering Titan's atmosphere (Hartle et al., 2006; Hörlst et al., 2012).

Titan's haze layer is made up of aerosols. Early experiments proposed a combination of polycyclic aromatic hydrocarbons (PAHs) and polycyclic aromatic nitrogen heterocycles (PANHs) as the composition of the aerosols (Sagan et al., 1993).

Early Titan flybys identified possible heavy PAH ions such as naphthalene, anthracene derivatives and an anthracene dimer at 130, 170 and 335 u/q respectively (Waite et al., 2007) and these are thought to be formed through ion-molecule reactions in the upper atmosphere (Westlake et al., 2014). Infrared measurements have also suggested the presence of PAHs/PANHS up to several hundred amu in the atmosphere (López-Puertas et al., 2013).

Previous ion composition studies using the Ion and Neutral Mass Spectrometer (INMS) and Cassini Plasma Spectrometer (CAPS) instruments revealed “families” of ions around particular mass values and a regular spacing of 12 to 14 u/q between mass group peaks. This is characteristic of the spectra of complex organic compounds and is related to the carbon/nitrogen backbone that dominates Titan’s ion chemistry (Waite et al., 2005; Cravens et al., 2006; Vuitton et al., 2007; Crary et al., 2009). Early Titan flybys by Cassini revealed positive ion masses up to 350 u/q, obtained using measurements from the CAPS Ion Beam Spectrometer (Waite et al., 2007). Later flybys demonstrated the existence of even larger positive ions up to 1100 u/q (Coates et al., 2010b). In addition to positive ions, negative ions have been detected in Titan’s ionosphere (Coates et al., 2007). These negative ions have been observed to higher masses than the positive ions with masses up to 13,800 u/q (Coates et al., 2009; Wellbrock et al., 2013, 2019). The negative ions are thought to be composed of carbon chains, with the higher masses having a suspected PAH/PANH composition (Coates et al., 2007; Desai et al., 2017).

The studies by Crary et al. (2009); Mandt et al. (2012) and Westlake et al. (2014) used IBS data to study various aspects of ion composition at Titan. These compositional studies covered positive ions (1-200 u/q) in Titan’s ionosphere and showed that the likely origin of the ions above 100 u/q were aromatic compounds created through ion-molecule reactions. Crary et al. (2009) discuss possible ion composition for mass groups up to C13, where C13 indicates the mass group where there are 13 “heavy” (carbon, nitrogen or oxygen) atoms present. The heaviest mass group they reported was the C15 group although the possible ion composition of this group was not discussed.

There have been several experimental efforts to replicate the organic haze present at Titan along with measurements of the ion-molecule gas-phase chemistry (Dubois et al., 2020). Some of these experiments have measured products up to 400 u (Berry et al., 2019). Chemical models based on CAPS measurements have proposed molecules up to the C17 group using a mechanistic approach to explain the carbon cation & anion chemistry (Ali et al., 2015). The schemes studied included hydrocarbons and nitriles, as well as various reaction paths for the growth of these molecules.

Ions with masses between 170 and 310 u/q are examined in this study with ion mass groups identified up to 275 u/q. Prominent groups identified contain 15, 16, 18 and 21 heavy atoms. Several ion groups also show variation in their occurrence between flybys.

4.2 Methodology

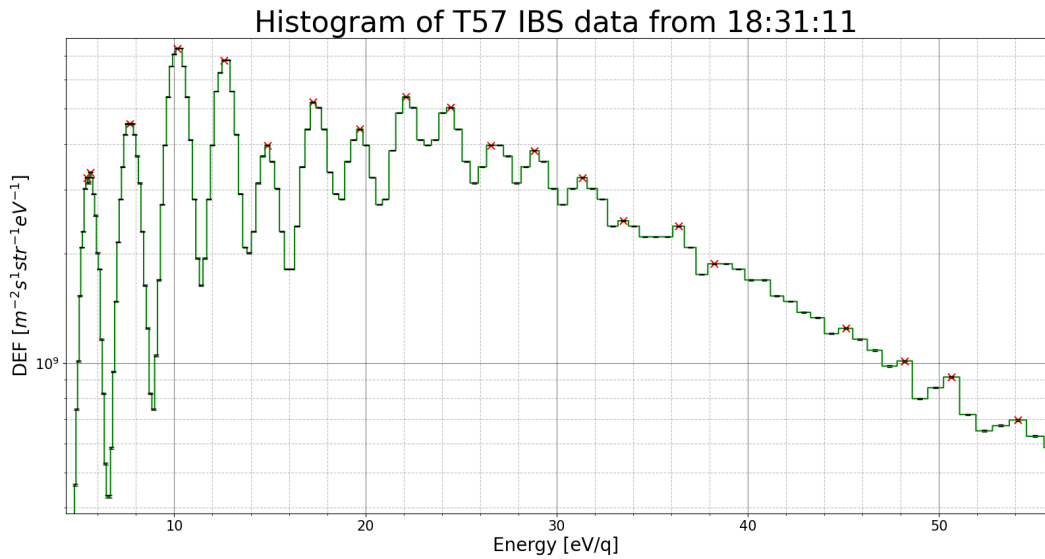


Figure 4.1: An example of an IBS energy spectrum taken during the T57 flyby. The error bars shown represent the uncertainty due to Poisson counting error. Red x's indicate the peaks as identified by the peak finding algorithm. Due to the logarithmic energy scale, at low energies the ion beams can be seen over a number of bins, while at the high energies the beams can only be seen in a single bin.

4.2.1 Cassini Plasma Spectrometer

Only data from CAPS IBS were used for the present study. CAPS IBS is a curved-electrode electrostatic analyzer and measures ion flux as a function of kinetic energy and direction (Young et al., 2004). As CAPS is mounted on an actuating platform, IBS can be rotated to increase its field of view but for the interest of this study I have focused on the Titan flybys where CAPS was at fixed actuation. This direction is approximately in the -X direction in the spacecraft frame and is aligned with the view direction of INMS. The flybys where CAPS was at a fixed actuation in the ram direction contain more resolvable ion peaks.

4.2.2 Data Analysis and Ion Winds

The first stage of the analysis was running a peak finding algorithm on each IBS energy sweep over a flyby. An example of one energy sweep can be seen in Figure 4.1. A peak was defined as any bin with a count number above the noise level of the instrument as well as above the Poisson counting error, i.e. the square root of the count number, when compared with adjacent energy bins. This was repeated across a flyby, Figure 4.2 shows the peaks identified during the T59 flyby with black dots plotted on top of a time-energy spectrogram.

During the Titan flybys, Cassini had a high velocity (6 km/s) relative to the low ion thermal (150K) and wind velocities (<230 m/s) in the ionosphere (Crary et al., 2009). These conditions imply that CAPS was measuring cold plasmas and techniques from Section 2.4 can be applied.

Through the inversion of equation (2.2) we can find a mass associated with each peak in the energy spectra. The width of each beam is roughly equal to the thermal velocity of the ions, as described by equation (4.1),

$$\frac{M}{\Delta M} \approx \frac{v_{sc} + v_{wind}}{\sqrt{\frac{2kT}{m_a}}}.$$
 (4.1)

Spacecraft charging can affect the energy/charge ratio of the particles measured by CAPS sensors. Spacecraft potential values are inferred from another Cassini instrument, the Radio and Plasma Wave Science (RPWS) Langmuir probe (Gurnett

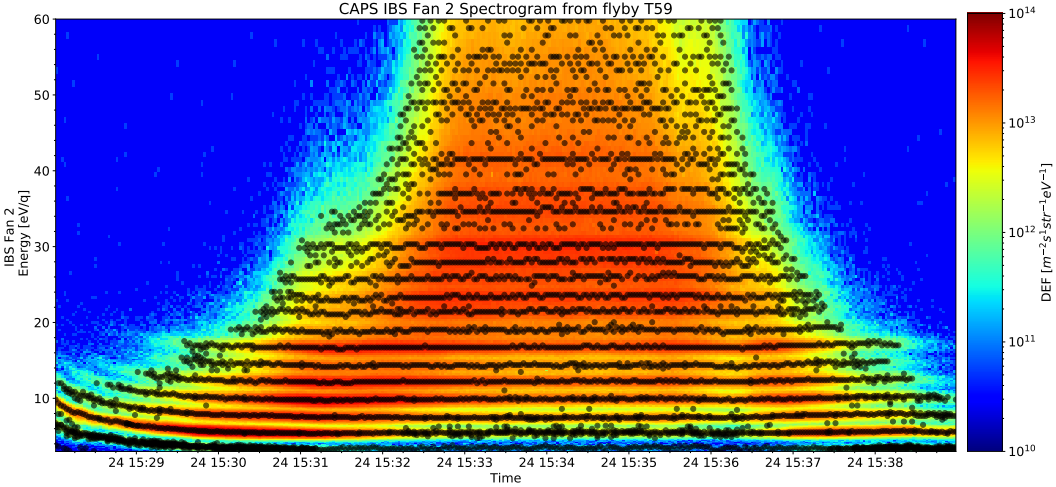


Figure 4.2: An energy/charge spectrogram from the T59 Titan flyby with intensity shown in Differential Energy Flux (DEF). Peaks identified by the algorithm are indicated by the black dots. The mass groups identified can be seen by horizontal lines of dots. Small variations in the energy of the identified peaks are due to effects such as ion velocity, spacecraft potential and slight shifts in spacecraft orientation. The energy shift on the inbound leg of the flyby (before 15:30) is due to the acceleration of ions away from Titan.

et al., 2004). A constant offset between the Langmuir probe and CAPS IBS of $+0.2 \pm 0.15$ V has been found by previous studies (Crary et al., 2009; Westlake et al., 2011; Mandt et al., 2012). For this study interpolated Langmuir probe potentials were used with an applied offset of +0.2 V. A fixed temperature of 150 K was also applied during the analysis. This value is representative of the temperatures seen in Titan's ionosphere which are between 100 and 200 K (Crary et al., 2009).

Examining the magnitudes of the three terms in equation (2.1) the dominant parameter is the ion wind. Taking the highest reported ion wind value of 260 ms^{-1} , this would represent a 9% shift in the ion kinetic energy, i.e a 2.8 eV shift for a 31.9 eV ion, which are the lightest ions examined in this study. The spacecraft potential term typically is between -0.5 and -2 eV (Crary et al., 2009). 2 eV represents a 6% energy shift for a 31.9 eV ion. Lastly, an ion temperature of 150 K corresponds to a 0.1 eV shift, a 0.3% shift for a 31.9 eV ion. As seen in equation (2.1), the ion temperature and spacecraft potential terms are not mass dependent, implying that for higher mass ions the energy shifts due to the ion temperature and spacecraft potential terms decrease as a proportion of the measured energy E_α .

The ion wind velocity calculation relies on previously identified major peaks. The determination for which peaks to use was influenced by the work of Mandt et al. (2012), who used the INMS instrument to calculate ion densities. The three major peaks used in this study were the 28, 39 and 91 u/q peaks, these masses were used as they were found to be the most abundant masses within their respective mass groups (Mandt et al., 2012).

These peaks can be used to estimate the ion winds that are present in Titan's upper atmosphere and ionosphere. The winds affect the detected energy of the ions by shifting their energy peak in each spectrum as seen in equation 2.1. To construct mass spectra from the ion data this effect must be accounted for. Using the previously stated abundant ions we can calculate the ion wind velocity by using a "mass-dependent effective spacecraft potential" defined as

$$\Phi' \approx \Phi + \frac{mv_{sc}}{e} v_{wind}, \quad (4.2)$$

by (Crary et al., 2009) and by differentiating we find

$$v_{wind} = \frac{e}{v_{sc}} \frac{d\Phi'}{dm}, \quad (4.3)$$

where Φ is the spacecraft potential, Φ' is the effective spacecraft potential, v_{sc} is the spacecraft velocity and v_{wind} is the alongtrack ion wind velocity. By finding the effective spacecraft potential corrections necessary for the three major mass peaks to be observed at their measured energies, we can calculate the gradient in equation 4.3 and the ion wind.

4.2.3 High Mass Methodology and Uncertainties

A full analysis of the ions would require convolutions of the ion distributions at separate masses with the IBS energy response and then a subsequent fit to the observed data. At the high masses studied here this becomes impractical as a result of the limited ability to resolve different masses due to the $\Delta E/E$ energy resolution at the Full Width Half Maximum (FWHM) of the IBS sensor. IBS was designed with a $\Delta E/E$ of 0.014 (Young et al., 2004) and calibration tests measured a $\Delta E/E$ of 0.02

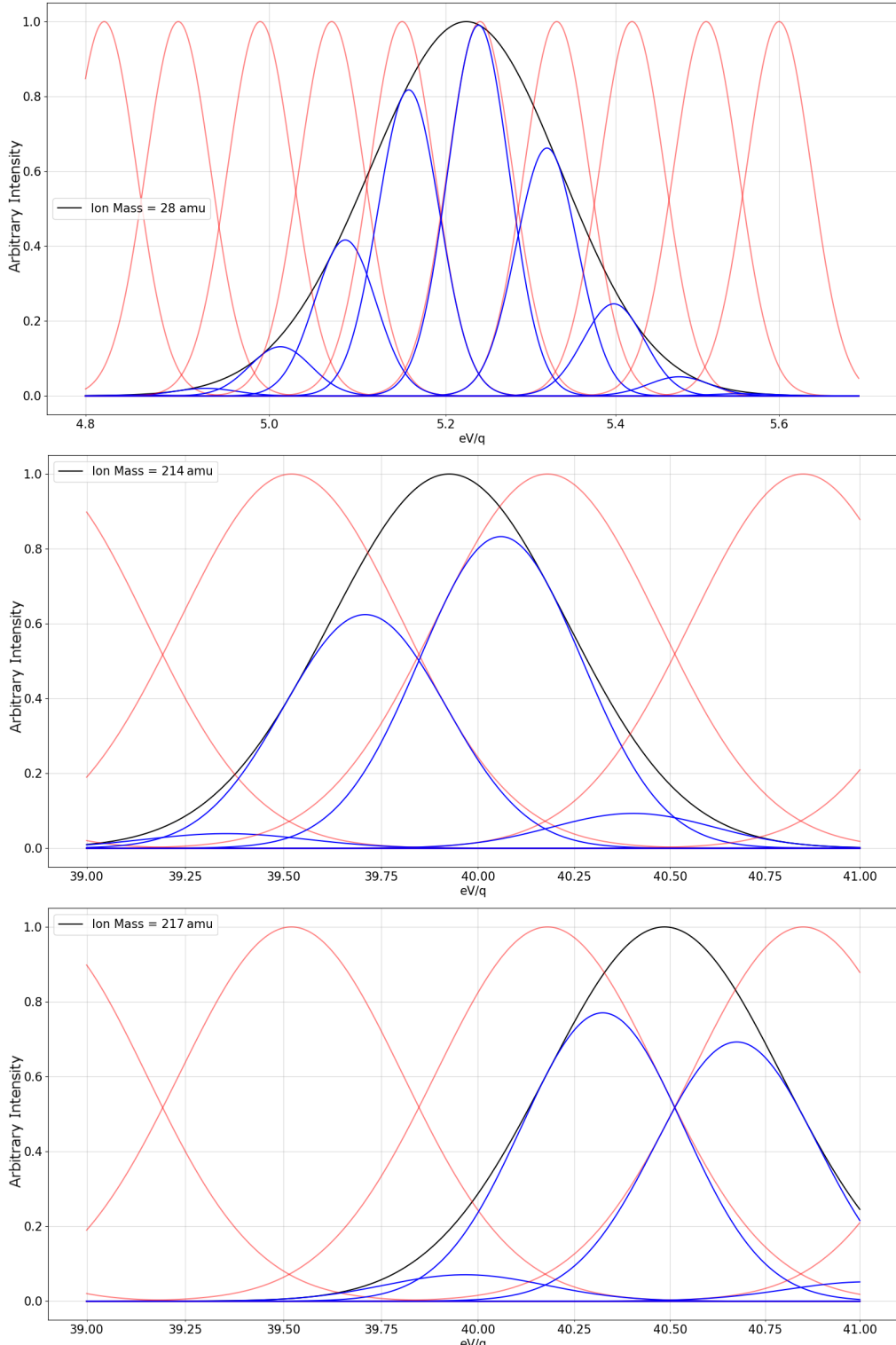


Figure 4.3: These three panels are used to illustrate the difference between observing low mass and high mass ion beams with the IBS sensor. For all three panels, the red lines represent the IBS response, with each gaussian curve representing a different IBS energy bin. The black line represents an observed ion beam, idealized with a gaussian and the width being determined by equation 4.1. The blue lines are each of the IBS energy bins (red) multiplied by the ion beam (black) and are representative of the spectra generated by IBS.

(Vilppola et al., 2001). Here I use a $\Delta E/E$ of 0.017, which was the operational $\Delta E/E$ value (Young et al., 2004) and was used in Crary et al. (2009). A $\Delta E/E$ of 0.017 results in the effective $M/\Delta M$ mass resolution being limited to <60 by the instrument's energy response.

How the energy resolution acts as a limiting factor in measurements is shown in Figure 4.3. The top panel is representative of a low mass ion beam as observed by IBS, while the middle and lower panels show high mass ion beams observed by IBS. As can be seen in the top panel, the low mass ion beam is well resolved across multiple energy bins. The sequence of blue gaussians in the top panel of Figure 4.3 can be compared to the first peak in Figure 4.1, as both represent beams with similar ion masses. The peak in Figure 4.1 appears across more bins due to the logarithmic scaling.

In contrast, the middle and lower panels show beams relating to ion masses of 214 and 217 u/q, both of which could cause a peak in the same IBS energy bin. From this it could be concluded that the same methodology can be applied to both low and high masses but comparing with Figure 4.1 we can see this is not the case. At the high energies above 35 eV/q, the beams are not resolved as they are less than three or four bins wide, with some peaks displaying similar intensity in the energy bins either side of the peak. This means that the fitting cannot be performed over several peaks and we are left to infer that any ion with the necessary mass to generate an ion beam with a peak energy within the FWHM of the peak energy bin is a plausible candidate. Returning to the middle and bottom panels of Figure 4.3, this means that any ion with a mass between 214 and 217 u/q could generate a peak in the energy bin centred around 40.2 eV/q, thus creating the uncertainty in our mass resolution.

After the peaks in the energy spectra were found and converted to mass spectra, the masses were binned at a 1 u/q resolution, similar to that done by Crary et al. (2009). This process does not generate a mass spectrum where I can analyze fragmentation patterns but shows which cations are more abundant than cations of neighboring masses.

The total mass uncertainty is calculated by adding in quadrature the uncertainty from the energy resolution and the uncertainty resulting from the 1 u/q binning process. The energy resolution dominates the total uncertainty, being ± 2 or ± 3 u/q compared to ± 0.5 u/q from the binning.

4.2.4 Studied Flybys

The five flybys studied all occurred in 2009, all with similar characteristics such as Solar Zenith Angle (SZA), latitude and longitude as can be seen in Table 4.1. CAPS was at a fixed actuation during these five flybys, meaning that rammed ionospheric ions were measured across the entire flyby, resulting in a greater number of data points than the previous actuating flybys. The times when Cassini exited Titan's shadow can also be seen in the table. 448 energy sweeps were used in total, covering altitudes from 955 to 1001 km. These are the lowest altitudes where CAPS measurements are available and where heavy ions are observed. There is variation in the solar illumination conditions in the data used between the flybys. The data selected from T55 was almost entirely in Titan's shadow, while T59 was illuminated the entire time with the other flybys containing a mixture.

4.3 Results

Through the use of the previously described algorithm across the 448 CAPS IBS energy sweeps, the occurrence of mass groups and the group peaks can be studied. Shown in Figure 4.4a is every peak identified across the five flybys, plotted against altitude. The previously found trend of heavier ions occurring at lower altitudes (Crary et al., 2009) can be seen. Figure 4.4b displays the peaks below 1000km between 200 and 300 u/q. With this plot several groups can be seen with distinct ion clustering around 203, 217, 228, 241 and 266 u/q. The T57 and T59 flybys have closest approaches of 955 and 957 km, around 10 km lower than the other three flybys that can be seen in the figure.

The low mass ions from 0-100 u/q have been well studied by both the CAPS and INMS instruments (Mandt et al., 2012; Westlake et al., 2014). Groups of intermediate mass (100-200 u/q) positive ions were found along with major peaks with

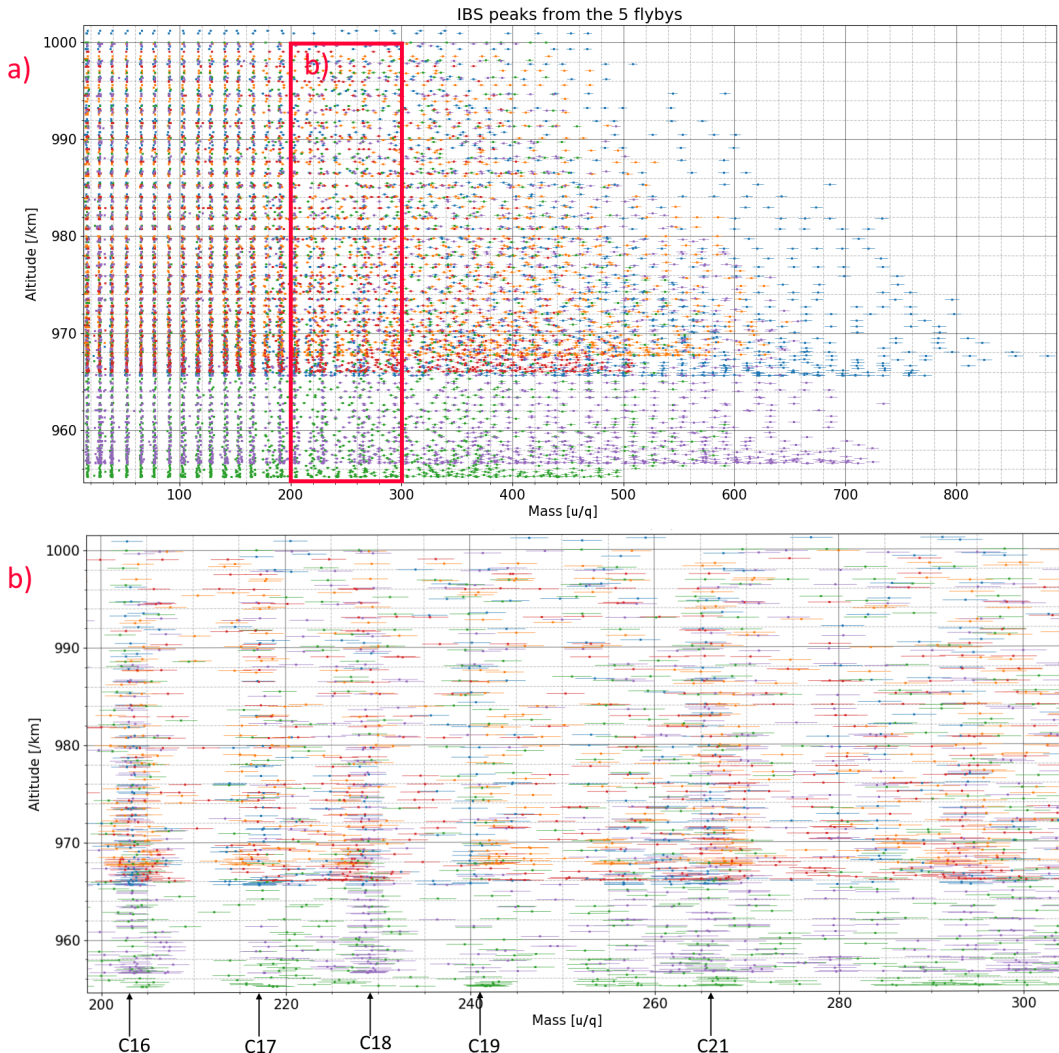


Figure 4.4: a) An altitude-mass plot for every peak identified by the peak finding algorithm at the altitudes examined. The error bars represent the instrument uncertainty for the peak detection. Each color represents a different flyby, T55 - blue, T56 - orange, T57 - green, T58 - red, T59 - purple. Panel b) is a section of panel a) between 200 and 300 u/q. Clear grouping of ions can be seen, notably around 203, 217, 229, 241 and 266 u/q, labelled C16, C17, C18, C19 and C21 respectively, as discussed in Section 4.3.2.

Flyby	UTC times	Titan shadow exit UTC time	Number of sweeps	Min altitude (km)	Max altitude (km)	Lat($^{\circ}$)	Long($^{\circ}$)	SZA Range ($^{\circ}$)	Titan Local Time
T55	21:25:13	21:28:06	88	966	1001	-19.1	176.1	134-149	22:00:27
	-	21:28:08							
T56	19:58:37	20:00:19	83	967	1000	-28.0	175.4	127-143	22:00:57
	-	20:01:21							
T57	18:30:57	18:31:37	97	955	1000	-34.9	173.1	119-137	22:07:31
	-	18:34:09							
T58	17:02:39	17:01:21	84	966	999	-44.7	172.4	112-128	22:07:42
	-	17:05:25							
T59	15:32:26	15:29:03	96	957	1000	-54.7	171.6	103-120	22:08:20
	-	15:35:39							

Table 4.1: Table displaying the data used in this study. The time where Cassini emerged from Titan’s geometric shadow is shown in the under “Titan shadow exit UTC time”. Min and Max altitudes demonstrate that these samples were taken at some of the lowest regions of Titan’s ionosphere traversed by Cassini. Latitude(Lat) and Longitude(Long) are displayed at the closest approach during the flyby. Solar Zenith Angle(SZA) Range is the range of SZA values observed in the sample range. Titan Local Time is shown in the last column.

a 12-14 u/q spacing between peaks. This study focuses on the high masses between 170 and 310 u/q outside the mass range of the INMS instrument. The structure is less clearly defined than the lower mass ranges and therefore only mass groups and significant peaks are focused on in this study.

4.3.1 Previously Reported Ion Groups (100 - 200 u/q)

For the comparison to Crary et al. (2009), after the peaks were found in the energy spectra and converted to mass values, the mass values were binned at a 1 u/q resolution. Then the number of occurrences of a peak in each 1 u/q bin across the five flybys was summed and then divided by the total number of sweeps examined across the flybys. This generates a percent occurrence value, representing how often a peak occurred at a certain mass in the studied data and is shown by the black line

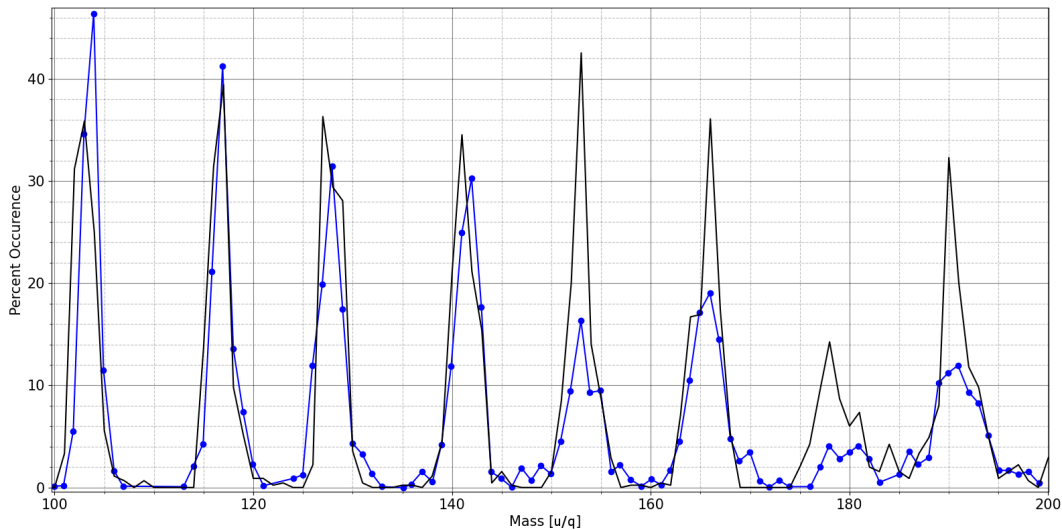


Figure 4.5: The black line represents the summed percent occurrence of the peaks over the flybys with 1 u/q binning from the present study. The blue line represents the percent occurrence from Crary et al. (2009). Good agreement can be seen, with the present study showing more defined peaks for the ion groups around 180 and 190 u/q.

in Figure 4.5. Eight mass groups were found in the 100 to 200 u/q mass range with each group being centered around a significant peak. For comparison, the percent occurrence found by Crary et al. (2009) is shown by the blue line.

This comparison is necessary due to this study’s application of different methodology than that applied previously in Crary et al. (2009). The main difference is that the cross-calibration between INMS and IBS data was not performed in this study, but was applied in the previous Crary et al. (2009) study. The comparison helps to link the existing study to the higher mass resolution measurements of INMS. Other differences include the mass peaks found by Crary et al. (2009) being derived from interpolating the energy spectra to 1 u/q mass bins using fit determined parameters and then identifying peaks. Lastly, Crary et al. (2009) studied flybys up to January 2008 and this study examines flybys during 2009, therefore, a comparison at this mass range is useful to check for variation with time.

Although there are methodology differences, this study reproduces the mass peaks identified by Crary et al. (2009) fairly accurately. Agreement between the new methodology and previous work gives confidence that the cross-calibration is not necessary for this study so I am able to extend the method to study high mass

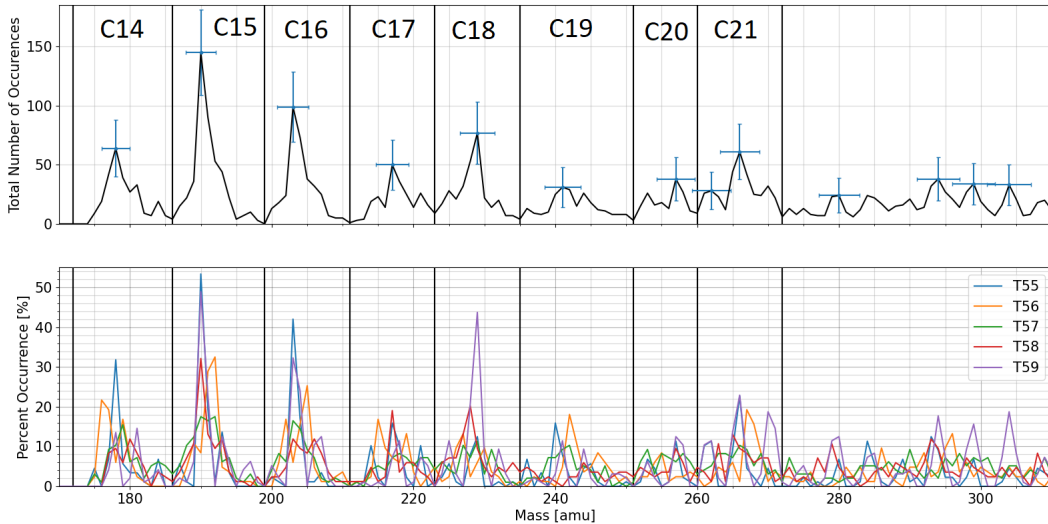


Figure 4.6: The top panel displays the total number of times a peak occurs in each 1 u/q bin. Vertical lines indicate the boundaries between the different ion groups, with the boundaries being defined by local minima in the total number of occurrences. Each group is labeled with C#, where # indicates the number of heavy (carbon/nitrogen/oxygen) ions present. The bottom panel represents the percentage occurrence by flyby, with the same group definitions as the top panel. For example the large peak for the T59 flyby in the C18 group occurs in 44% of the 96 sweeps examined. The vertical error bars in the top panel shown are three times the standard error relating to Poisson counting statistics, meaning there is a 99% probability that the number of occurrences lies within this range. The horizontal error bars are a combination of the uncertainty resulting from the energy resolution and the uncertainty from a 1 u/q binning.

ions above 200 u/q.

4.3.2 High Mass Ions (170 - 310 u/q)

The high mass ions and mass group structure is displayed in Figure 4.6. The mass group numbering (C#) indicates the number of heavy atoms (carbon/nitrogen/oxygen) present. A clear structure can be seen for the C14 to C19 groups, corresponding to masses between 172 and 251 u/q. Each group has a major peak and there are well-defined troughs between the groups. Furthermore, below 251 u/q the spacing between peaks of 12 to 14 u/q agrees with the trend observed at lower masses.

The C20 and C21 groups have major peaks but also display minor peaks and the troughs between groups are not as evident. At these masses, the 12 to 14 u/q spacing trend breaks for C20, with a 16 u/q gap between C19 and C20 and a 9 u/q

gap between the major peaks of C20 and C21. However as there are uncertainties of ± 3 u/q due to the energy resolution of IBS at these masses, it is plausible that the spacing is closer to 12 or 14 u/q. Alternatively, there is a minor peak in the C20 group at 253 u/q, which would correspond to 12 and 13 u/q gaps between the C20 peak and its neighboring groups.

Above 270 u/q no clear peak and trough structure can be seen in Figure 4.6. Several significant peaks do exist, one such peak is seen at 280 u/q that would be associated with an ion containing 22 heavy atoms. At the largest masses studied there are peaks at 294 ± 3 , 299 ± 3 and 304 ± 3 u/q. These peaks however do not have a distinct gap between them due to the uncertainties in measurement. Given the range of masses, it is likely there are multiple peaks associated with ions containing 23 or 24 heavy atoms.

4.3.2.1 Peak Spacing

Further analysis of the mass spacing between peaks was performed to aid the understanding of growth pathways. This was done by finding the mass difference between each possible pair of peaks and dividing each mass difference by the difference in number of assumed heavy atoms. For example, the mass difference for the 178 and 217 u/q peaks is 39 u/q and the difference in assumed heavy atoms is 3, generating a peak spacing of 13 u/q. This was repeated for all possible peak pairs and then the peak spacing was averaged. The results from this can be seen as a box and whisker plot in Figure 4.7, with the mean plotted in red.

The lower and upper bounds of the whiskers are due to the combined uncertainty from both peak measurements. For example, the 203 and 217 u/q peaks both have an uncertainty of ± 2 u/q, meaning the peak spacing for this pair could be between 10 and 18 u/q. The value shown for the lower bound is the average of this minimum spacing across all peak pairs, a similar calculation gives the value for the upper bound. Some peaks such as 257, 262 and 299 u/q have large interquartile ranges, these are caused by neighboring peaks with small mass differences. These peaks could also be indicative of a molecule containing a heavier atom than carbon, such as nitrogen or oxygen, which would then affect the spacing between the peaks.

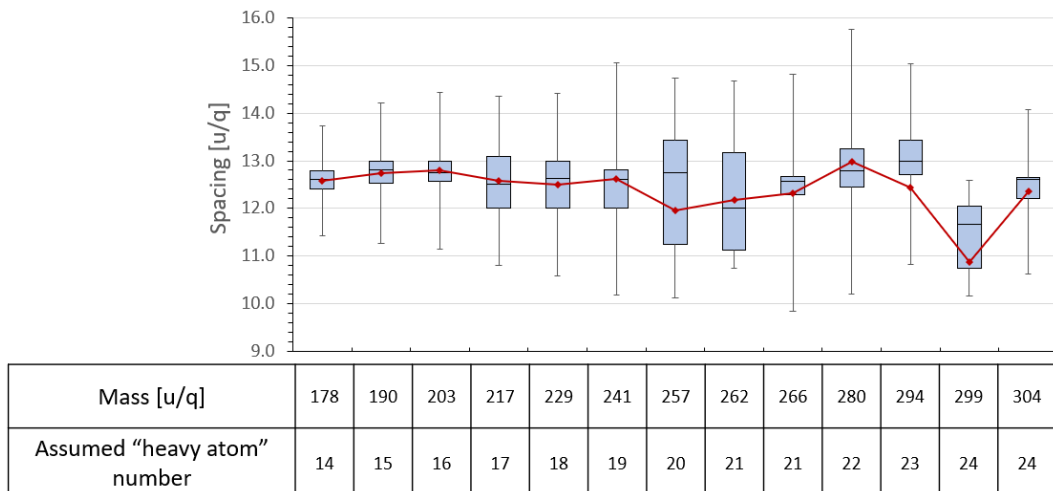


Figure 4.7: A box and whisker plot demonstrating the mass spacing between the significant observed peaks under an assumption of the number of “heavy atoms” (carbon/nitrogen/oxygen) in a molecular ion. This is calculated by finding the mass difference between pairs of peaks and dividing by the difference in “heavy atoms”. The mean spacing is plotted in red and is largely in the 12 and 13 u/q range. The box shown represents the interquartile range of the peak spacing along with the median. The low mean spacing of 11 u/q for the 299 u/q peak is due to the close neighboring masses at 294 and 304 u/q, a similar effect can be seen for the 257 and 262 u/q peaks.

The mean spacing across all peaks is 12.4 u/q, the lower quartile is typically around 12 u/q and the upper quartile around 13 u/q. These masses would be consistent with a C or CH addition to the molecular ions.

4.4 Discussion

Many structures have been hypothesized for the large molecular ions in Titan’s ionosphere. These have included polyacetylene, polyynes and cyanopolyyne (Wilson and Atreya, 2003; Lavvas et al., 2008a,b; Vuitton et al., 2019). $(\text{HCN})_n$ polymers have been proposed (Wilson and Atreya, 2003), as well as $\text{HC}_3\text{N}/\text{C}_2\text{H}_2$ copolymers (Lebonnois et al., 2002; Lavvas et al., 2008b). PAHs and PANHs have been proposed as well (López-Puertas et al., 2013; Zhao et al., 2018), resulting from the detection of benzene in Titan’s upper atmosphere (Waite et al., 2007). Amines and imine polymers have been proposed to contribute to Titan’s haze due to either the prerequisite monomers being found in Titan’s atmosphere or the molecules being detected in tholin experiments (Vuitton et al., 2006; Cable et al., 2014; Skouteris

et al., 2015). Fullerenes have also been proposed to exist (Sittler et al., 2020).

For assessing the abundant ion composition, I compare the masses associated with the ion peaks with the masses consistent with different structures. This includes those structures mentioned above as well as other possible structures such as long aliphatic hydrocarbons with different levels of saturation. These aliphatic hydrocarbon chains include alkanes, alkenes, dienes, trienes and alkynes. A table summarizing the comparison of peaks to possible structures is shown in Figure 4.8. Combinations of aliphatic hydrocarbons and various polymers can explain the observed ion peaks but the chemical structures that are consistent with all peaks are Polycyclic Aromatic Compounds (PACs). Furthermore, chemical structures such as $(HCN)_n$ polymers, are consistent with peaks for $n = 7, 8, 9$ and 11 , but are not present for $n = 10$, which is unlikely to occur. This does not rule out the presence of aliphatic compounds but rather suggests that the most abundant ions observed in this study are consistent with PACs. PACs represent a combination of PAH and/or polycyclic aromatic heterocycles containing nitrogen. Oxygen-bearing polycyclic aromatic molecules are also possible. There are also likely methylene substituted derivatives of these compounds, as proposed in Ali et al. (2015).

PACs possibly have a role in the formation of aerosols (Lavvas et al., 2011). Early experiments found that Titan tholin analogs contain PAHs (Sagan et al., 1993) and also that PAHs may adsorb onto the tholins. Later studies have also found PANHs and PAHs in Titan tholin analogs (Trainer et al., 2013; Yoon et al., 2014; Mahjoub et al., 2016; Sciamma-O'Brien et al., 2017). Gautier et al. (2017) discuss how aerosol growth is affected depending on the number of aromatics rings in the reactant composition, finding that benzene and pyridine caused production of co-polymeric structures while double-ringed aromatic produced quasi-pure polymeric structures. Other studies have also investigated the impact of ions interacting with charged aerosols, demonstrating that they contribute to the growth of these particles (Lavvas et al., 2013). These findings indicate that the composition of Titan's aerosols is likely affected by the composition of the positive PAC ions studied here.

Westlake et al. (2014) examined three hypotheses for the production of high

mass ions in Titan's ionosphere. They concluded that the most viable method for creating large molecular ions was through ion-molecule reactions with neutral acetylene, ethylene and hydrogen cyanide. Ali et al. (2015) further investigated the cation, anion and neutral chemistry that could be present in Titan's ionosphere through ion-molecule reactions. Low-temperature formation pathways of PAHs through radical-neutral reactions have been shown to exist for molecules with up to four six-membered rings (Zhao et al., 2018).

Comparing the findings presented here with the ion-molecule reactions proposed in Westlake et al. (2014) and Ali et al. (2015), I find the ion group peak masses agree with the expected masses resulting from ion-molecule reactions. Furthermore, comparing with proposed neutral PAHs/PANHs from López-Puertas et al. (2013), I find the reported neutral molecules have comparable masses, suggesting ionization and electron recombination are a factor. These two comparisons suggest a coupling between the cationic and neutral phases at the studied mass range.

4.4.1 Ion Mass Group Composition

Here I discuss the composition of the positive ions and a possible growth mechanism. The C14 and C15 group peaks have masses consistent with cationic three ringed PACs. Examining the C14 group across all flybys, the major peak lies between 176 and 181 u/q in the IBS data. Ali et al. (2015) suggested hydrocarbon cations of $\text{C}_{14}\text{H}_9^+$, $\text{C}_{14}\text{H}_{11}^+$ and $\text{C}_{14}\text{H}_{13}^+$ as well as nitrogen-bearing $\text{C}_{13}\text{H}_{10}\text{N}^+$ and $\text{C}_{13}\text{H}_{12}\text{N}^+$ ions. These molecules lie within the 176 and 181 u/q range given the associated errors, meaning I cannot distinguish between the PAHs and nitrogen-containing PACs. Similarly, the cations in the C16, C17 and C18 groups can be associated with four ringed PAC cations and the C19, C20 and C21 with five ringed PAC cations.

The C15 group frequently occurs in all flybys generating a strong peak at 190 \pm 2 u/q. Ali et al. (2015) describe the mechanism of substituting CH_2^+ in place of a hydrogen atom in a neutral PAC to generate cations, this would increase the mass of the ion by 13 u/q, consistent with our peak spacing finding of 12 to 13 u/q. Subsequent reactions with neutral ethylene creates larger cations alongside ejection

		Formula	Mass [u/q]
		$C_{18}H_9$	178^{+2}_{-2}
		$C_{14}H_{10}$	190^{+2}_{-2}
		$C_{15}H_{10}$	203^{+2}_{-3}
		$C_{16}H_{11}$	217^{+2}_{-2}
		$C_{17}H_{12}$	229^{+2}_{-3}
		$C_{18}H_{12}$	241^{+3}_{-3}
		$C_{19}H_{11}$	257^{+3}_{-3}
		$C_{18}H_{12}$	262^{+3}_{-3}
		$C_{17}H_{14}$	266^{+3}_{-3}
		$C_{18}H_{11}N$	280^{+3}_{-3}
		$C_{19}H_{14}$	299^{+3}_{-3}
		$C_{20}H_{14}$	304^{+3}_{-3}
Ringed structures	Polycyclic Aromatic Compounds	$C_{18}H_{10}$	$C_{17}H_{11}$
		$C_{16}H_{11}$	$C_{17}H_{14}$
Graphite/ Graphene	Graphite	$C_{15}H_{10}O$	$C_{16}H_{11}N$
		$C_{16}H_{11}O$	$C_{17}H_{15-22}$
Fullerene	Graphene	$C_{15}H_9N$	$C_{18}H_{13}N$
		$C_{12}H_8N_2$	$C_{21}H_{11}N$
Cycloalkane	Fullerene	C_{16}	C_{17}
		$C_{20} \& C_{22}$	C_{19}
Cycloalkane	Cycloalkane	C_{20}	C_{20}
		C_{22}	C_{22}
CN polymer	Cycloalkane	$C_{17}H_{14}$	$C_{19}H_{14}$
		$C_{19}H_{14}$	$C_{19}H_{14}$
HCN polymer	CN polymer	$C_{19}H_{14}$	$C_{19}H_{14}$
		$C_{19}H_{14}$	$C_{19}H_{14}$
HC ₃ N/C ₂ H ₂ copolymer	CN polymer	H_7CN_7	H_8CN_8
		H_7CN_7	H_9CN_9
Nitrogen-bearing polymers	HC ₃ N/C ₂ H ₂ copolymer	$C_{11}H_5N_3$	$C_{11}H_5N_3$
		$C_{12}H_4N_4$	$C_{12}H_4N_4$
Linear amine	HC ₃ N/C ₂ H ₂ copolymer	$C_{13}H_7N_3$	$C_{13}H_7N_3$
		$C_{15}H_9N_3$	$C_{15}H_9N_3$
Methanimine polymer	Linear amine	$C_{12}H_4N_2$	$C_{12}H_4N_2$
		$C_{13}H_7N$	$C_{13}H_7N$
Aliphatic Hydrocarbons	Methanimine polymer	$(CH_3NH)_x$	$C_{12}H_2N_7$
		C_2H_2	$C_{18}H_2$
Aliphatic Hydrocarbons	Polyacetylene	$(CH_2)_k$	$C_{18}H_2$
		C_2H_2	$C_{20}H_{20}$
Aliphatic Hydrocarbons	Alkane	C_3H_{2x+2}	$C_{17}H_{16}$
		C_4H_{2x}	$C_{18}H_{18}$
Diene	Alkene	C_4H_{2x+2}	$C_{17}H_{14}$
		C_3H_{2x+2}	$C_{18}H_{16}$
Triene	Diene	C_4H_{2x+4}	$C_{19}H_{16}$
		C_3H_{2x+2}	$C_{20}H_{20}$
Alkyne	Triene	C_3H_{2x+4}	$C_{19}H_{14}$
		C_3H_{2x+2}	$C_{21}H_{16}$

Figure 4.8: A table showing the structures consistent with significant peaks. The structures are broken into three groups and highlighted in different colors for clarity: ringed structures containing aromatic and cyclic molecules, nitrogen-bearing aliphatic molecules and aliphatic hydrocarbon molecules. Any molecule that lies within the mass uncertainty associated with a peak is considered plausible. Polycyclic Aromatic Compounds are consistent with all observed ion peaks, followed by a graphite- or graphene- like structure, consistent with nine of the thirteen observed peaks. The list of polycyclic aromatic molecules considered are from the NASA Ames PAH IR database (except for the 294 u/q peak) and should be viewed as not-exhaustive.

of one or two H₂ molecules. A similar mechanism is also proposed by Westlake et al. (2011), who investigated both ion-molecule reactions with neutral acetylene and ethylene.

The same CH₂⁺ substitution mechanism can be applied to generate all observed ion group peaks. From Figure 4.8 for example, possible growth chains of CH₂⁺ substitutions could be C₁₄H₉ → C₁₅H₁₀⁺ followed by C₁₅H₁₀ → C₁₆H₁₁⁺. These chains could also exist at the upper end of the studied mass range as well, C₂₀H₁₄ → C₂₁H₁₃⁺ alongside a H₂ ejection followed by C₂₁H₁₃ → C₂₂H₁₄⁺. These chains could similarly occur for nitrogen- or oxygen- bearing PACs. Although this growth pathway is consistent with the observed peak spacing it does not rule out other reactions occurring with PAC cations.

Oxygen ions entering the ionosphere and the presence of H₂O, CO₂ and CO (Cui et al., 2009; Hörst et al., 2012) imply that oxygen-bearing polycyclic aromatic molecules are plausible, although are likely to have a small contribution compared to PAHs or PANHs. The oxygen ions charge transfer with neutrals generating thermal O atoms (Vuitton et al., 2019) and interstellar medium experiments have found reaction pathways between atomic oxygen and the C₁₀H₈⁺ naphthalene cation (Le Page et al., 1999b). Le Page et al. (1999) studied reactions between various pyrene cations and atomic oxygen and found that C₁₆H₉O⁺ and C₁₆H₁₀O⁺ could be created. The reaction with CO could be significant and has been shown to incorporate oxygen into tholins in atmospheric simulation experiments (Fleury et al., 2014). Other reactions involving OH, H₂O and other oxygen-bearing molecules cannot be ruled out but are not explored here. The formation pathways and reaction rates for oxygen-bearing polycyclic aromatic molecules are poorly understood but their presence cannot be ruled out by this study.

4.4.2 Variations between Flybys

Examining the different characteristics for the five studied flybys: the closest approach altitudes were between 955 and 967 km, the closest approach longitudes were within a 5 degree range and the closest approach local times were all close to 22:00. However, the SZA values range from 103 to 149, which is primarily due

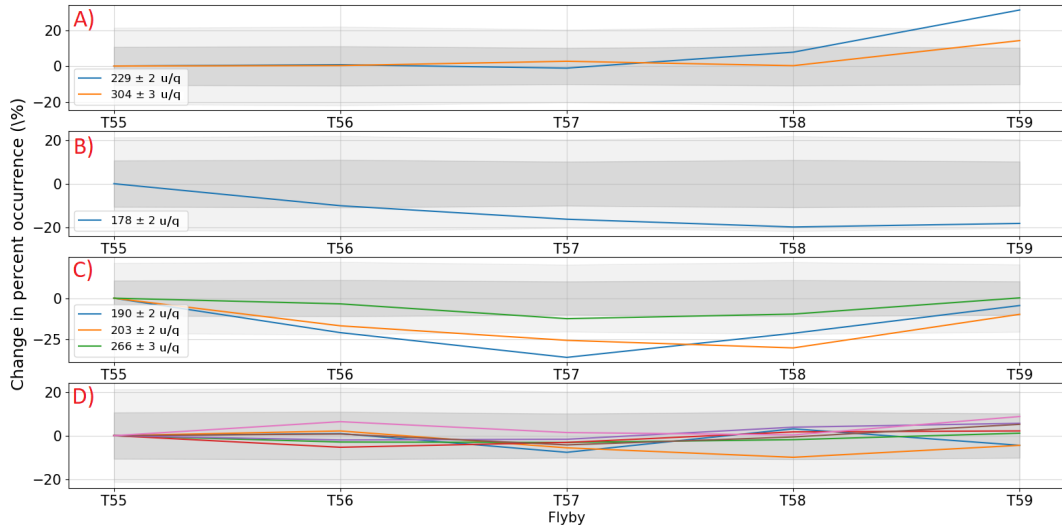


Figure 4.9: The change in percent occurrence of the observed peaks, as compared to T55. The uncertainties are Poisson counting statistics, with the dark grey and light grey regions representing one and two times the standard deviation respectively. The peaks are categorized into four groups, panel A) shows peaks which occurred more frequently under illuminated conditions. Conversely, panel B) shows a peak which occurred more frequently under unilluminated conditions. Panel C) shows the peaks which had a minimum during the flybys and panel D) are the remaining seven observed peaks that show no clear variation, with all points lying within one standard deviation.

to the flyby latitude increasing from -19° during T55, to -55° during T59. There is also variation in the percentage occurrence of some observed peaks between different flybys. This could be a signature of varying production, loss and transport rates of the ions associated with the peaks. Furthermore, it could be linked to neutral and anion chemistry that occurs, which varies between the day and nightside of Titan (Vuitton et al., 2019). Examining Figure 4.9, six of the thirteen significant peaks display clear variations. Some peaks occur more frequently with more solar radiation while one peak occurs less frequently. Furthermore, some peaks can be seen to occur less frequently in the transition between illuminated and unilluminated conditions.

From Figure 4.9, we can see that the 229 ± 2 and 304 ± 3 u/q peaks occur more frequently in the T59 flyby. Examining the percentage occurrence of the 229 u/q peak in Figure 4.9, there is a 35% increase for T59 compared to T55. The trend for the 304 ± 3 u/q peak is not as clear, with the significant increase in occurrence

occurring only during the T59 flyby.

In contrast, panel B) in Figure 4.9 shows the only example of a significant decrease in percent occurrence, associated with the 178 ± 2 u/q peak in the C14 ion mass group. Between the dark T55 flyby and the illuminated T59 flyby the peak occurrence drops by around 20%. The C14 group is the least frequently seen group in the 100-200 u/q range in both this study and Crary et al. (2009), which could be related to this observed variation.

The third panel in Figure 4.9 shows three peaks which have an occurrence minimum during the five studied flybys. The 190 ± 2 and 266 ± 3 u/q peaks have a minimum percentage occurrence during the T57 flyby while the 203 ± 2 u/q peak has a minimum during T58.

Due to Titan’s extended atmosphere the effects of solar EUV radiation on ions are seen past the terminator, up to SZA values of 135° at 1000 km (Ågren et al., 2009; Cui et al., 2009; Coates et al., 2009, 2011; Wellbrock et al., 2009, 2013). Although at high SZA values the solar radiation is attenuated by passing through more of Titan’s atmosphere. Cui et al. (2009) studied the diurnal variations of positive ions, finding that light ions were strongly depleted on the nightside while the heavy ions were moderately depleted and that the most significant diurnal variations were seen at low altitudes. These depletions are linked to the loss of ion production from solar EUV radiation.

Similar to the light cations, light anions (<50 u/q) have been shown to have higher densities on the dayside (Wellbrock et al., 2012; Mihailescu et al., 2020). On the other hand, Wellbrock et al. (2009) and Coates et al. (2009, 2011) show that heavy anion densities under illuminated conditions past the terminator are lower than unilluminated conditions in the deeper nightside ionosphere, as observed during flybys such as T57. The higher densities of heavy anions in unilluminated conditions could provide a competing pathway to heavy cation production. This could be through higher anion production rates or through lower anion loss rates, an example of a loss process would be photodetachment. Photodetachment efficiency increases with ion size (Lavvas et al., 2013; Wellbrock et al., 2019), which would

remove heavy anions from the dayside allowing for higher heavy cation densities. Ionization energy is the energy needed to remove an electron from a molecule while electron affinity is the amount of energy released when an electron is added to a molecule. There is a general trend of increasing electron affinity and decreasing ionization energy with increasing PAH mass (Christodoulides et al., 1984; Dabestani and Ivanov, 1999), meaning larger PAHs can more readily form positive or negative ions under favorable conditions.

Wellbrock et al. (2013) identified several mass groups of negative ions, with the 190-625 u/q mass group displaying the highest density of all groups at an average peak altitude of 1000 km. The flybys in this study are at a similar altitude and the mass range studied covers this negative ion group.

Due to the complex cation-neutral-anion chemistry and lack of information on reaction rates at these high masses, I cannot distinguish between different factors such as anion chemistry, ion transport and changing ion-neutral pathways. Future investigations that examine flybys in the noon/midnight regions would help identify photochemical effects. Furthermore, future chemical models could aid identification of these heavy molecular ions through examining recombination rates and ion-neutral reactions to see which ions are consistent with observed variations.

4.4.3 Comparison with Neutral PACs in Titan's Atmosphere

López-Puertas et al. (2013) studied infrared emission from Titan and applied a fitting algorithm to identify neutral PACs in the upper atmosphere. A total of 7 of their 19 most abundant PACs lie in the 170-310 u/q mass range. These seven molecules are C₁₃H₉N (179 u/q), C₁₂H₈N₂ (180 u/q), C₁₄H₁₆ (184 u/q), C₁₆H₁₀N₂ (230 u/q), C₂₀H₁₀ (250 u/q), C₂₀H₁₄ (254 u/q) and C₂₂H₁₆ (280 u/q). These neutral molecules are in the even numbered mass groups: C14, C18, C20 and C22.

Three of these molecules are in the C14 group, C₁₃H₉N, C₁₂H₈N₂ and C₁₄H₁₆. The first two of these neutrals could be related to the major C14 peak in the IBS data at 178 u/q. López-Puertas et al. (2013) reported C₁₄H₁₆ to be present at a low concentration and in this study I find a minor peak (percentage occurrence below 10%) at 184 ± 2 u/q that occurs in four of the studied flybys. This peak could result

from the ionization of the reported C₁₄H₁₆ neutral.

C₁₆H₁₀N₂ is in the C18 group and could be related to the ion mass peak at 229 u/q. The two molecules in the C20 group, C₂₀H₁₀ and C₂₀H₁₄, were some of the least abundant molecules reported by López-Puertas et al. (2013). The major peak in the C20 group is at 257 ± 3 u/q with a minor peak at 253 ± 3 u/q. This puts both molecules within the error of the ion peak. However, there is no clear peak structure at 250 u/q with the region between 248 and 251 u/q being a trough between the C20 and C21 groups. This could indicate that I see a higher level of hydrogenation in the cationic phase.

Although I do not find clear structure for the C22 group, there is a peak at 280 ± 3 u/q therefore a similar mass to the neutral C₂₂H₁₆ at 280 u/q. This peak strongly occurs during the T58 and T59 flybys, peaking at 279 u/q and 280 u/q respectively.

In summary, from the comparison between the ionic and neutral phases, the masses of previously observed neutral PACs in Titan's atmosphere correlate with cations in the ionosphere. The only exception found was the neutral PAH C₂₀H₁₀. The comparisons between the observed abundant neutral molecules and the frequently occurring ion peaks indicate that there is a need for combined study of the neutral and cationic phases to fully characterize Titan's ionosphere. In addition, further study of what neutral PAHs exist in Titan's ionosphere could aid with interpretation in future ion compositional studies.

4.5 Conclusions

The composition of positive ions between 170 and 310 u/q has been examined during five CAPS actuator-fixed flybys that took place during 2009. The composition was investigated by examining how frequently a peak occurs at a given mass. Up to 275 u/q there is a clear ion group structure of peaks and troughs, where the peaks are ion masses with a high relative abundance. Conversely, the troughs are associated with ions of low relative abundance. Between 275 and 310 u/q, several prominent peaks are found but with no clearly associated group structure. The identified ion peaks are consistent with various aliphatic compounds, however, polycyclic aromatic

compounds, such as PAHs/PANHs, are found to be consistent with all identified peaks. The spacing between peaks was found to be between 12 and 13 u/q, with an average spacing of 12.4 u/q consistent with the addition of C or CH.

Variation in the occurrence of prominent peaks indicates changes in the photochemistry, most likely due to differing solar radiation conditions, at the studied 170-310 u/q mass range. Comparisons with neutral PAHs/PANHs findings in the atmosphere reveal that the ion peaks in this study are at similar masses to the abundant molecules in the neutral phase. This implies coupling between the ion and neutral phases at these masses.

This is the first identification of these high mass ions and represent the largest distinct positive ion groups reported so far in Titan's ionosphere. The discovery of these groups will aid future atmospheric chemical models of Titan through the identification of what heavy positive ions are prominent, aiding the understanding of which reaction pathways are plausible to create the previously found heavy negative ions and neutrals. The future Dragonfly mission to Titan will study the surface composition and prebiotic chemistry. Given that the complex organic compounds created in Titan's atmosphere form the particles that comprise the haze found at lower altitudes and that these particles are expected to fall onto the surface, understanding the origin of these organic compounds gives helpful insight into the interpretation of future results.

Chapter 5

Ion velocities and spacecraft charging in Titan’s ionosphere: I. Crosstrack velocities and Cassini spacecraft potentials

During Cassini’s flybys of Titan, it passed through the moon’s atmosphere and ionosphere. Using data from the Cassini Plasma Spectrometer instrument, ion velocities perpendicular to Cassini’s trajectory have been derived in Titan’s ionosphere for the first time. The anion and cation crosstrack velocities are found to be in line with expectations from coupled ion-neutral flows inside a collisional environment. However, extreme values of crosstrack velocities are found to be several hundred metres per second, far higher than previous estimates, impacting future ion density and velocity studies of Titan’s ionosphere. Additionally, spacecraft potentials are reported from several sensors aboard Cassini. The spacecraft potentials derived from the electrostatic analyzers measuring anion and cation populations were found to be in agreement with previous studies, however, they disagree with each other and estimates from other Cassini instruments. The findings in this chapter will help future studies investigating crosstrack velocities and spacecraft charging in coupled ion-neutral flows.

5.1 Introduction

Crosstrack velocities are velocities that are perpendicular to the spacecraft's velocity vector. They are typically more reliable than alongtrack velocity measurements due to spacecraft charging and ion composition, which affects alongtrack measurements more (Lomidze et al., 2019). They are typically measured using the angular deflection of ions relative to the spacecraft's velocity vector.

In this chapter, I will cover the methodology used to derive crosstrack ion velocities for positive and negative ions in Titan's ionosphere and the findings from these results. I will also report results concerning spacecraft potential measurements from CAPS sensors and compare them to previous findings. The next chapter, Chapter 6, covers the methodology of deriving alongtrack ion velocities and spacecraft potentials, and will further investigate the dynamics of Titan's ionosphere and neutral winds in Titan's thermosphere.

5.1.1 Spacecraft potential measurements and discrepancies

As outlined in Section 2.5, spacecraft charging can be derived by CAPS measurements of positive and negative ions. During flybys of Titan by Cassini, the spacecraft passed through the moon's ionosphere measuring multiple positive and negative ion populations. By using known and estimated parameters such as ion mass and ion velocity, spacecraft potentials can be derived by examining the observed energy of the ions.

The Radio and Plasma Wave / Langmuir Probe (RPWS/LP) instrument aboard Cassini was another instrument that could provide estimates of the spacecraft potential for both positive and negative spacecraft charging. This can provide a point of comparison for spacecraft potential estimates derived from CAPS measurements. Several studies have used both spacecraft potential measurements for CAPS and RPWS and compared the offsets.

Crary et al. (2009) used CAPS IBS data to examine heavy positive ions and ion winds in Titan's ionosphere and found an offset between spacecraft potentials derived from IBS and Langmuir probe. This offset was $+0.25V \pm 0.035V$, with IBS deriving higher voltages than the Langmuir probe. The offset was approximately

constant across various voltages and was explained through the Langmuir probe and CAPS instrument being located on different parts of Cassini and a non-uniform spacecraft potential.

Similar measurements have been made of negative ions using the CAPS ELS sensor. Desai et al. (2017) found that the spacecraft potential measured by CAPS ELS was 0.4 to 0.9V more negative than that measured by the Langmuir probe. This discrepancy was interpreted as focusing effects on the anions by the spacecraft potential causing them to arrive closer to the spacecraft surface.

Comparing the potentials derived from Langmuir probe, CAPS ELS and IBS, we can see that there are discrepancies between all three sensors. Although the discrepancy between the two CAPS sensors and the Langmuir probe can be explained by a non-uniform potential, the two CAPS sensors are co-located and should experience a similar potential (Crary et al., 2009). Whether the discrepancy between the sensors is due to ion deflection by the spacecraft potential or an instrumentation or methodological issue is still an open question which will be explored further.

5.2 Methodology

5.2.1 Crosstrack ion velocities

The crosstrack velocities described here are partial crosstrack velocities, as they only take into account crosstrack velocities perpendicular to the rotation axis and not parallel to it. As Cassini passed through Titan's ionosphere, in the CAPS frame, the ions were observed as a supersonic directed ion beam due to the high relative velocity of Cassini to the ions. If there were no crosstrack velocities, these ion beams would appear when CAPS actuates across the velocity vector. The crosstrack velocities deflect the ions so they appear at an angle to the velocity vector.

These velocities are important for inferring flows in the plasma environment relative to Cassini, they also are important for the effects on other measurements. Mandt et al. (2012) states that sensitivity for INMS is affected by these crosstrack velocities and the effect on sensitivity has a inverse dependence with mass. For example, they state a 100 m/s crosstrack velocity would cause a 20% reduction in

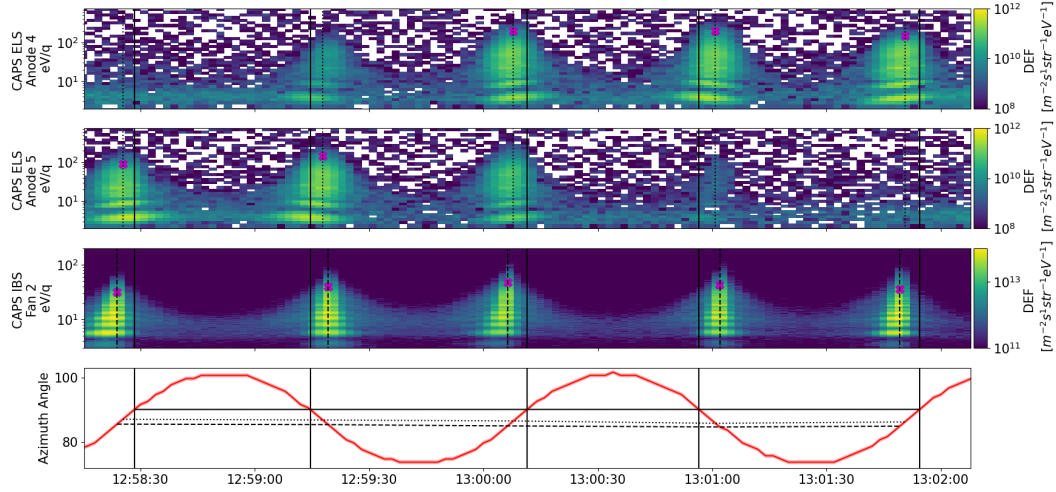


Figure 5.1: This figure displays data from the T49 flyby to illustrate how the crosstrack velocities are observed using time-energy spectrograms and the actuator position. All panels have time on the x-axis, with energy on the y-axis for the top three panels which are spectrograms while the bottom panel has azimuthal angle on the y-axis. On the three spectrograms intensity in Differential Energy Flux (DEF) is shown in colour. The top two spectrograms are two anodes from the ELS sensor, while the third spectrogram is from the IBS central fan. In the last panel the actuator position is shown with the red line as it actuates back and forth across the angle associated with Cassini’s trajectory, this angle is shown with the horizontal black line. When the actuator crosses Cassini’s trajectory vector, a vertical black line is added across all panels, indicating the expected angle that ions would arrive from if crosstrack velocities were not present. The vertical dotted and dashed lines represent the direction that the heaviest negative and positive ions respectively are measured from. These are associated with the near horizontal dotted/dashed lines in the last panel which show at what angle these ions are measured at.

the count rate for a 28 amu ion.

5.2.1.1 Method

The first step in deriving the crosstrack velocities is determining the times when CAPS actuates across Cassini’s velocity vector, which is used as a starting point to search for ion beams. These times are determined from Navigation and Ancillary Information Facility (NAIF) Spacecraft Planet Instrument C-matrix Events (SPICE) kernels, which contain spacecraft attitude information. A time window is centred on these times to ascertain when the ion beams were observed by CAPS. Across each time window, a peak finding algorithm is applied at a single energy level to find when CAPS crossed the ion beam. This energy level is determined by several

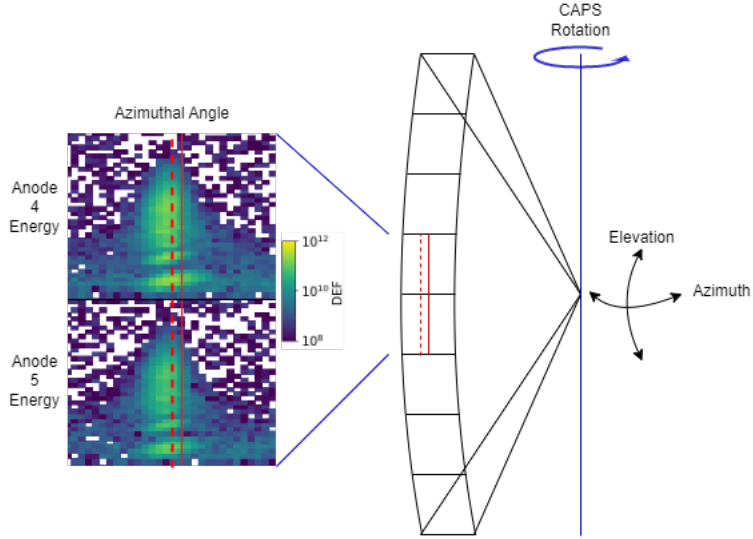


Figure 5.2: A cartoon to illustrate the field of view (FOV) of CAPS ELS and a brief pictorial depiction of the methodology in this study. Shown on the right is the FOV for CAPS ELS, with 8 anodes across the elevation direction and CAPS rotating with its actuator around the azimuthal direction. The middle fan of IBS has a similar FOV but without anodes along the elevation direction. Typically during the Titan flybys used in this study, CAPS actuates across the velocity vector so that the central anodes of ELS pass over the incoming ions. The direction the incoming ions would appear from without the effect of crosstrack velocities is noted by vertical red lines, where they are actually observed coming from is noted by the vertical red dashed line. As can be seen, this difference is associated with an angle relating to the crosstrack velocity as described in the text.

factors: the necessity to stay above the noise level of the instrument, the ability to adequately resolve the ion beam and lastly, to detect the heaviest ions possible. Detecting the heaviest ions possible is necessary as light ions can be deflected by the spacecraft potential (Jones et al., 2011), thereby including a spacecraft effect rather than the ambient crosstrack velocity. The time window applied and the energy level used are flyby dependent due to the different characteristics of flybys such as the actuation pattern used and the closest approach of the flybys. The prominence, i.e how much ion flux is enough to resolve an ion beam, is here defined as a percentage of the peak flux observed at all energies in a time window. The prominence applied to the heaviest ions for the peak finding algorithm was flyby dependent for the positive ions and 3.3% of the peak flux for the negative ions. Electrostatic analyzers such as ELS & IBS take time to sweep through the energies they measure, meaning

that depending on the energy level of the heaviest ions, they will be measured at different times during the energy sweeps. This time difference between the start of the energy sweep and the time when the heaviest ions are observed is taken into account during the calculation. Lastly, as the actual time when the actuator crossed the ion beam may be between adjacent energy sweeps, a weighted average is taken at the heaviest ion energy bin over time, weighted by the flux.

After taking into account the various steps described above, the expected ion beam and actual ion beam were found, as depicted in Figure 5.1. The calculation is described by the equation,

$$v_x = v_{sc} \sin(\theta_{pos/neg} - \theta_{ram}) \quad (5.1)$$

where v_x is the crosstrack velocity, v_{sc} is the spacecraft velocity, $\theta_{pos/neg}$ are the azimuthal angles that the positive/negative ions are observed to be coming from and θ_{ram} is the azimuthal angle of Cassini's velocity vector.

5.2.1.2 Uncertainties

There are several uncertainties associated with the measurement of the crosstrack velocity, one of which is the true position of the actuator. During the Cassini mission, there was concern that the position of the actuator was not being accurately recorded (Wilson et al., 2012). This led to homing runs being performed where the actuator was pushed to one of the stop limits to realign the actuator. Although these homing runs have been taken into account in the data processing, some uncertainty could still be present in the true position of the actuator. Furthermore, during acceleration and deceleration of the actuator at the azimuthal limits of the sweeps a ± 0.5 degree error is present.

CAPS ELS and IBS have temporal resolutions of 2 seconds at their highest cadence, meaning that a conservative estimate of this error would be at most 1 second, due to the peak ion flux appearing in only one energy sweep. A 1 second uncertainty in time at a typical Cassini flyby velocity of 6 km/s would correspond to a 100 m/s uncertainty in the crosstrack velocity.

During calibration it was noted that the ELS and IBS sensors' maximum response across the various azimuthal angles is energy dependent. This introduces another source of uncertainty, as this may affect where the maximum flux at an energy is measured and this is used in the calculation of the crosstrack velocity. This uncertainty is minimal compared to other factors, with the ELS response midpoint being 0.41 degrees off nominal at 125 eV (Young et al., 2004), while the IBS response midpoint is off by approximately 0.29 degrees (Vilppola et al., 1996, 2001).

As stated previously, the spacecraft potential can affect the charged particle trajectories thereby changing the inferred crosstrack velocities. However, some mitigation has been implemented by using the heaviest ions.

Any uncertainties in the NAIF SPICE kernels that were used to calculate the actuation and therefore the pointing of the CAPS instrument could affect the crosstrack velocity derivation. This uncertainty is likely to be negligible as the kernels have gone through several revisions and verifications since the data was collected, with the latest update being in 2019.

5.2.2 Spacecraft potential

Spacecraft charging theory and measurement methodology is covered elsewhere in this thesis, in sections 2.4, 2.5 and 6.2.1.1 .

5.2.2.1 Uncertainties

A major source of uncertainty in the spacecraft potential is the separation of spacecraft charging effects from alongtrack velocities. Equation 2.1 shows that spacecraft potentials affect the measured ion energy linearly, while the ion velocity effect on the energy scales with the mass of the ion. The derivation of the alongtrack velocity accounts for this by using multiple ion species to separate the two terms. However, when a limited number of ion species are used the separation of the two terms becomes increasingly difficult, resulting in greater uncertainty. ELS data is particularly affected due to the fewer number of energy peaks observed in the spectra as well as the limited energy resolution compared to IBS.

5.2.3 Cassini Flybys

31 flybys were utilised during this study, covering a time period between 2006 and 2012. During flybys T55 to T59, CAPS was operating at a fixed actuation, meaning crosstrack velocities could not be derived, however, spacecraft potentials could still be found.

A full list of flybys studied, the flyby characteristics, e.g. latitude, longitude, solar zenith angle, and derived velocity values can be found in Appendix A.

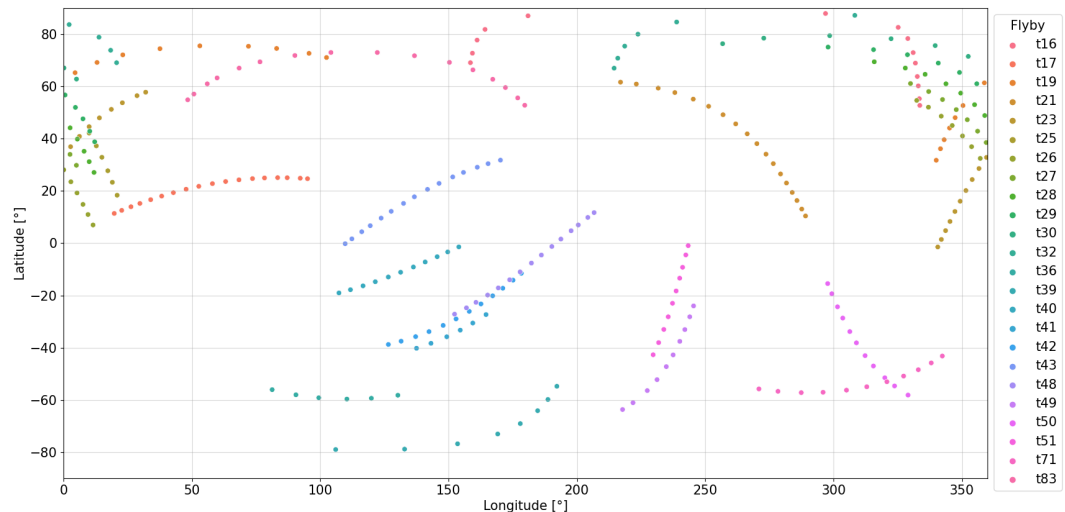


Figure 5.3: A latitude/longitude plot to display the spatial coverage of the data used. As can be seen, there is variation in sampling, but most latitudes and longitudes are covered.

5.3 Results

5.3.1 Crosstrack Ion Velocities

The distribution of the derived cation and anion crosstrack velocities can be seen in Figure 5.4. The figure demonstrates that there is a clear proportionality between the two velocity distributions. This is supported by the correlation coefficient value of 0.95. Additionally, a 95% confidence interval on the correlation coefficient gives bounds of 0.93 and 0.96, further showing the clear proportionality. The proportionality is nearly one to one, with a linear fit producing a gradient of approximately 1.1.

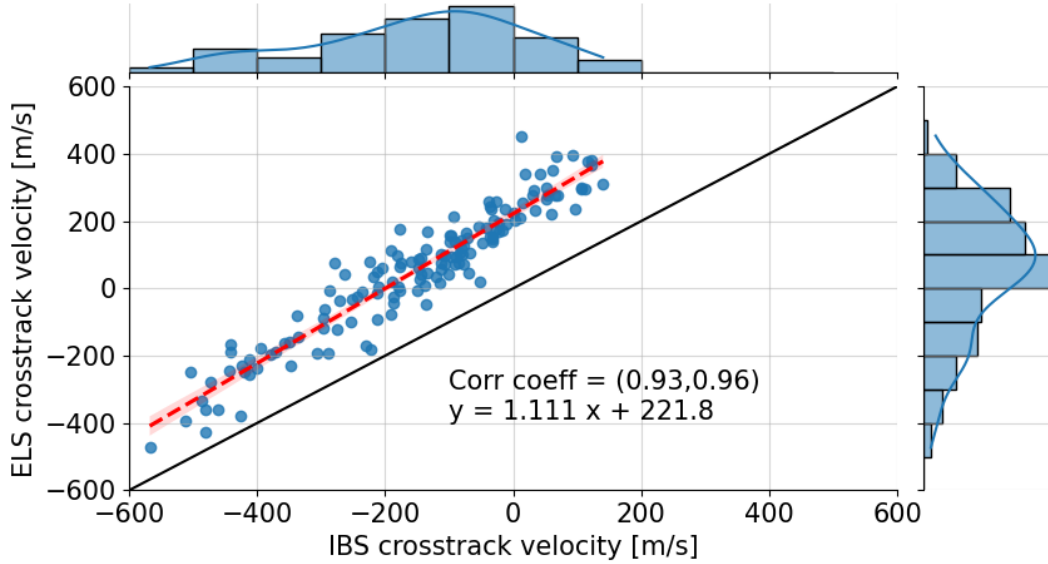


Figure 5.4: The distribution of the cation and anion crosstrack velocities as measured from CAPS IBS and ELS respectively, with 1D distributions plotted on the sides. In the plot text, the equation describing the best linear regression fit is shown, as well as 95% confidence interval values for the correlation coefficient . The fit is shown with the red dashed line, along with a 95% confidence interval in red shading. The black line is a $y=x$ line to highlight the offset.

Intriguingly, there is a clear skew among the cation crosstrack velocities towards negative values. In addition, there appears a slight skew towards positive values for the anion crosstrack velocities, although this effect is not as strong. Quantitatively, this can be seen in the linear fit, with the y -offset being 217.6 m/s.

Figure 5.5 displays the positive and negative ion crosstrack velocities by flyby. There are two notable features in this figure, firstly that there is no temporal trend for the crosstrack velocities, with little variance between flybys. This is not wholly unexpected due to the varying conditions these flybys occurred under. The other notable feature, which is the same feature as noted in Figure 5.4 is the offset between the positive and negative ion velocities along with the clear proportionality between them.

5.3.2 Derived spacecraft potential

Spacecraft potentials were derived across both actuating and non-actuating flybys. The derived potentials for the actuating flybys can be seen in Figure 5.6, with the spacecraft potentials derived from IBS and ELS data shown in light blue and orange

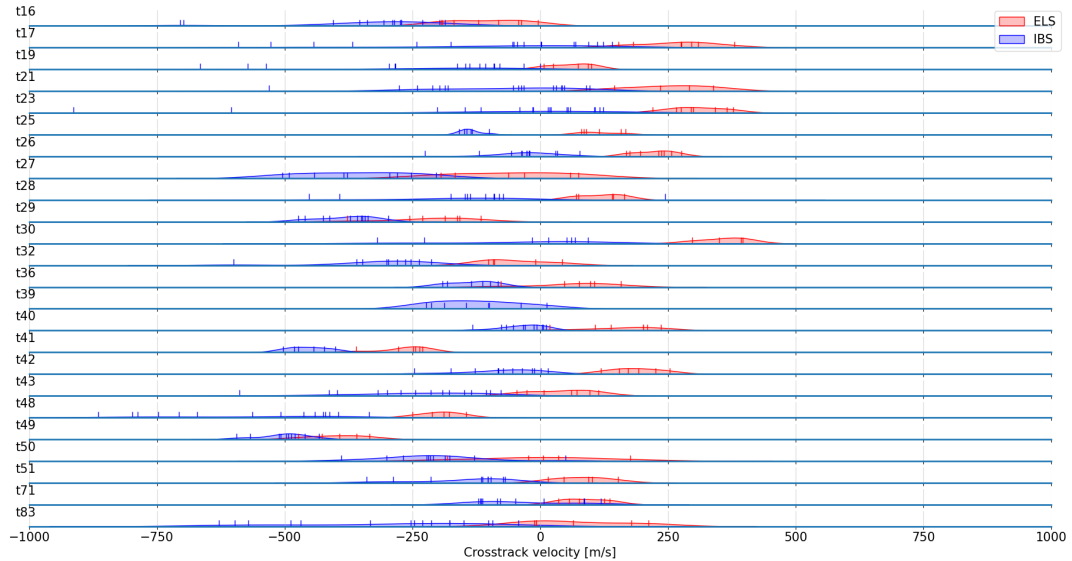


Figure 5.5: Shown are the crosstrack velocity distributions of positive and negative ions separately vertically by flyby. Positive and negative m/s refer to which side of the expected azimuthal direction the ions were measured to be arriving from. The positive ion crosstrack velocities are shown in blue, while the negative ion crosstrack velocities are shown in red. The negative ion distributions can be seen to have more positive velocities than the positive ion distributions. Extreme values above 600 m/s in magnitude are only observed for positive ions above 1200 km.

respectively. Derived potentials from the Langmuir Probe (LP) are shown in red. The LP potentials are linearly interpolated to the CAPS observation times.

Furthermore, Figure 5.6 includes CAPS estimates from other studies that derived the spacecraft potential. Crary et al. (2009) (Green) stated that the IBS derived potentials had a +0.25 V offset from the Langmuir probe measurements of spacecraft potential and this is shown in the figure. Some flybys were omitted in Crary et al. (2009), while others took place after the study. Shown in yellow are values representing if the same voltage offset found in Crary et al. (2009) (Green) was extrapolated to cover all flybys in this study. Desai et al. (2017) (Dark Blue) derived potentials from ELS negative ion measurements for several flybys and these potentials are shown. The errorbars in Figure 5.6 represent the range of values found during each flyby rather than uncertainty in a single measurement.

As can be seen, for all flybys and for both IBS and ELS derived potentials, the values fall within the -3.5 to 0 V range established by Crary et al. (2009). Further-

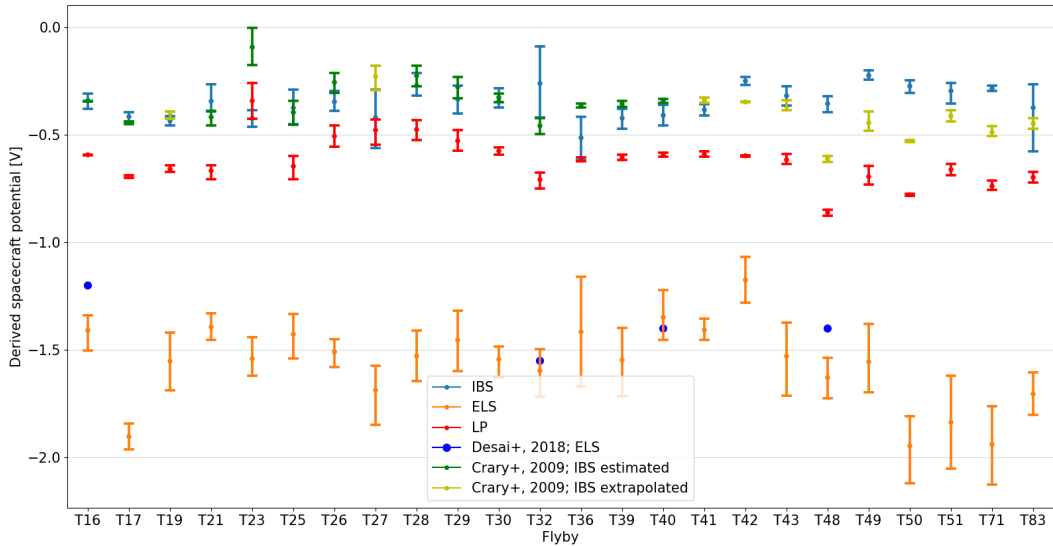


Figure 5.6: The range of spacecraft potentials as derived from IBS (Light blue) and ELS (Orange) ion measurements. Only data where potentials can be derived from both IBS and ELS sensors is shown. The derived potentials from the Langmuir Probe (Red) are shown as well, in addition to estimates from CAPS measurements by other studies, (Crary et al., 2009) (Green), (Crary et al. 2009, extrapolated: Yellow) and (Desai et al., 2017)(Dark blue). Across all the flybys, it can be seen that the IBS potentials are slightly above LP, while ELS potentials are significantly below.

more, for the flybys studied here which were studied in Crary et al. (2009), there is good agreement for the derived spacecraft potentials from IBS. Both studies agree there is roughly a +0.25 V offset from the Langmuir probe. However, from T48 onwards, the LP potentials can be seen to drop slightly while the IBS derived values remain approximately in the same voltage range.

For the data points where a comparison is possible with Desai et al. (2017), good agreement can be seen during the T32 and T40 flybys with the potentials derived from ELS data in this study. During the T16 and T48, the potentials from Desai et al. (2017) are slightly higher than the ones in this study. Similar to the LP values, a change in derived potentials can be noted during some of the later flybys such as T50, T51 and T71, with lower potentials than previously derived, with the exception of T17, being an earlier flyby with a notably lower value.

From T48 to T71, a change can be seen in the derived values in Figure 5.6. This change is characterized by the IBS derived potentials deviating from the expected

values from Crary et al. (2009) by several tenths of a volt.

As the derived spacecraft potentials in this study are mostly similar to previously derived values, it demonstrates the validity of the methodology, although the discrepancy between the derived values is of note, particularly between the CAPS sensors.

5.3.2.1 Actuator-fixed flybys

T55-T59 were fixed actuator flybys, meaning the sensors only pointed along Cassini's velocity vector and could consistently measure rammed ions on every energy sweep. Therefore, there are far more derived values for these flybys and they will be discussed separately here. The derived potentials with respect to altitude for the non-actuating flybys can be seen in Figure 5.7.

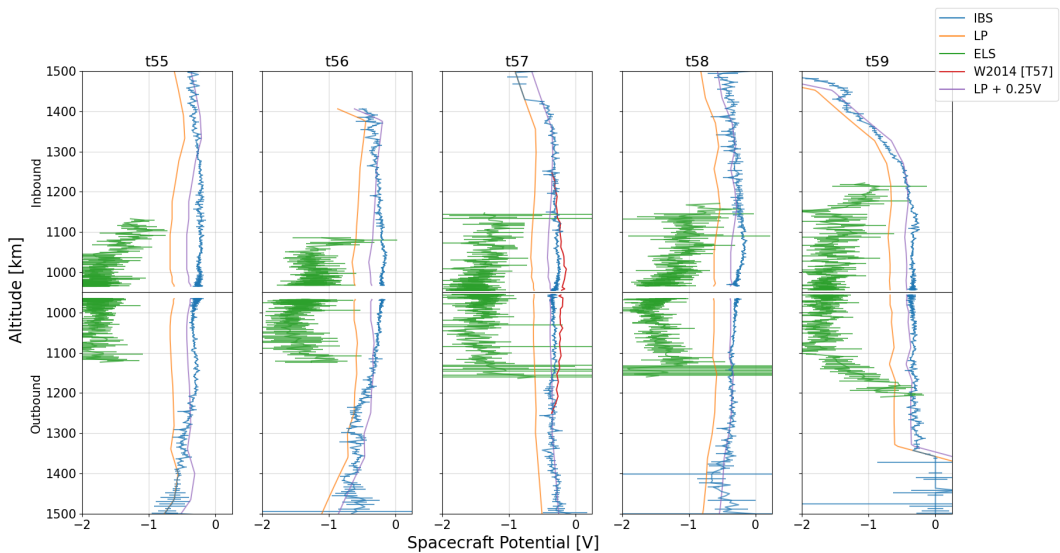


Figure 5.7: The range of spacecraft potentials as derived from ELS, IBS and LP measurements during the non-actuating CAPS T55-T59 flybys. The inbound portion of the flybys are shown in the top panels, while outbound in shown in the bottom panels. ELS derived values are shown in green, IBS derived values are shown in blue, while LP derived values are shown with in orange. Errorbars representing uncertainties are shown for the ELS and IBS derived potentials. Spacecraft potentials derived by Westlake et al. (2014) during the T57 flyby are shown in red. Lastly, the LP potentials with the +0.25 V offset described by Crary et al. (2009) are shown in purple.

The inbound and outbound legs of the flyby are shown in the top and bottom row of panels respectively, with the Langmuir Probe, ELS and IBS derived poten-

tials shown with orange, green and blue lines respectively. Potentials can be derived from negative ions up to around 1200 km in altitude, while potentials from positive ions can be derived to higher altitudes. Above 1500 km there are large uncertainties due to a limited number of positive ion groups being seen, meaning that the methodology used here is unable to accurately distinguish between spacecraft potential and ion velocity effects on the particle energies. These growing uncertainties can be seen in the errorbars for the IBS derived potentials in Figure 5.7 as Cassini nears 1500 km.

Similar to the actuating flybys, the derived spacecraft potential from IBS is higher than the one derived from the LP, with this being true for all data points below roughly 1250 km, above 1250 km this varies by flyby. The difference between the LP and IBS potentials is typically higher than the value previously reported by Crary et al. (2009), with the IBS potential being +0.3 V to +0.5 V higher than the LP reported value.

Also similar to the actuating flybys, the derived spacecraft potentials from ELS are below both that of the LP and IBS sensors. ELS derived potentials are typically 0.4 to 1.4 V lower than the LP and up to 2 V lower than the IBS derived potentials. The ELS derived potentials show no clear trend with altitude below 1100 km, remaining approximately constant, while above 1100 km there are some indications that the ELS potentials increase, becoming closer to that derived by the LP.

Spacecraft potentials have been previously derived during the T57 flyby by Westlake et al. (2014), shown in red in Figure 5.7. They used a similar method to Crary et al. (2009) with both IBS and INMS data used. Shown in purple are values representing a +0.25 V offset from the LP, in line with the findings of Crary et al. (2009).

5.4 Discussion

5.4.1 Crosstrack velocity distributions and magnitudes

The largest cation crosstrack velocity recorded was -913 m/s at an altitude of 1756 km during the T23 flyby and the largest anion crosstrack velocity was -473 m/s at

996 km during the T49 flyby, these can be seen in Figure 5.5. Previous estimates of crosstrack velocities, such as 100 m/s in Mandt et al. (2012), are smaller than the largest values recorded here. However, these estimates were made at lower altitudes in the ionosphere, rather than around 1800 km such as the maximum cation crosstrack velocity recorded in this study. Furthermore, Woodson et al. (2015) found ion velocities on the order of 1-2 km/s at altitudes of 2300-2800 km. The largest cation crosstrack velocity where both cation and anion crosstrack can be derived is -567 m/s. During the same actuation sweep the largest anion crosstrack velocity was also recorded.

Mandt et al. (2012) state that crosstrack velocities greater than 200 m/s will transfer ions outside the INMS field of view. The high velocities found in this study imply that greater emphasis should be placed on understanding the crosstrack velocities in future Titan INMS studies, as these velocities will affect ion density studies.

The distribution of the anion velocities is centred around 100 m/s, with extreme values ranging from -500 to 400 m/s, as seen in Figure 5.4. The cation velocity distribution ranges from -600 m/s to 200 m/s, with a distribution peak at around -100 m/s. Both the anion and cation distributions are unbalanced around the centre, with their tails towards more negative values being larger than the opposite tail towards more positive values. The centre offsets from 0 m/s for the cation and anion distributions is unexpected, particularly as the offsets are in opposite directions for the differently charged populations. This could be due to the presence of electric fields in Titan's ionosphere (Ågren et al., 2011; Rosenqvist et al., 2009; Shebanits et al., 2022). This hypothesis would be supported by an interpretation by Ågren et al. (2012), who found oppositely directed positive and negative ion velocities as a possible interpretation of Langmuir Probe data. They modelled their data with ion velocities of up to 260 m/s, which had been the highest velocity reported in Crary et al. (2009), however, they also state that the velocities could be higher, up to several km/s. An issue with this interpretation is that electric field directions would have to be consistent across flybys to reproduce the same velocity shift effect, and

with the variety of flyby trajectories observed in this study, this is unlikely.

The spacecraft potential can deflect the lighter ions trajectory and cause them to arrive from a different direction to the spacecraft velocity vector. On the other hand, as stated in the methodology section, mitigation was attempted for this uncertainty by choosing the heaviest ions. However the presence of these offsets may be an indication that the mitigation was not entirely successful. Crary et al. (2009) state that both the spacecraft potential and crosstrack velocity can affect the direction of the peak ion flux and for this reason they do not attempt to compute the crosstrack velocity. In this study, I use the actuator position in addition to both positive and negative ion data, which aids the separation of the two effects. This is due to the opposite charge states of the positive and negative ions, meaning that the complex spacecraft potential shape will have different effects on the differently charged ions. This could cause the centre offset noted in the previous paragraph, as well as the offset seen between the positive and negative ion populations, i.e the fit not passing through (0, 0) in Figure 5.4. On the other hand, if this offset is caused by the spacecraft potential then the expectation would be that a relationship between the magnitude of the spacecraft charging and the crosstrack velocity should be observed. However, this is not seen in the available data as evidenced in Figure 5.8, with no trends found between derived spacecraft potentials and crosstrack velocities.

The strong cation-neutral coupling described by Cravens et al. (2010) also extends to anion-neutral collisions, meaning there should be an overall cation-neutral-anion flow direction. The proportionality between the crosstrack velocities for the positive and negative ions reinforces this idea, as a neutral crosstrack flow would influence both the cation and anion crosstrack velocities similarly, meaning the velocities measured would be proportional to each other. I produce ion-neutral collision calculations demonstrating this in Chapter 6.

5.4.2 Spacecraft potential measurements

For spacecraft potentials derived during the actuating flybys, the similarity of the IBS derived potentials compared to Crary et al. (2009) imply that the methodol-

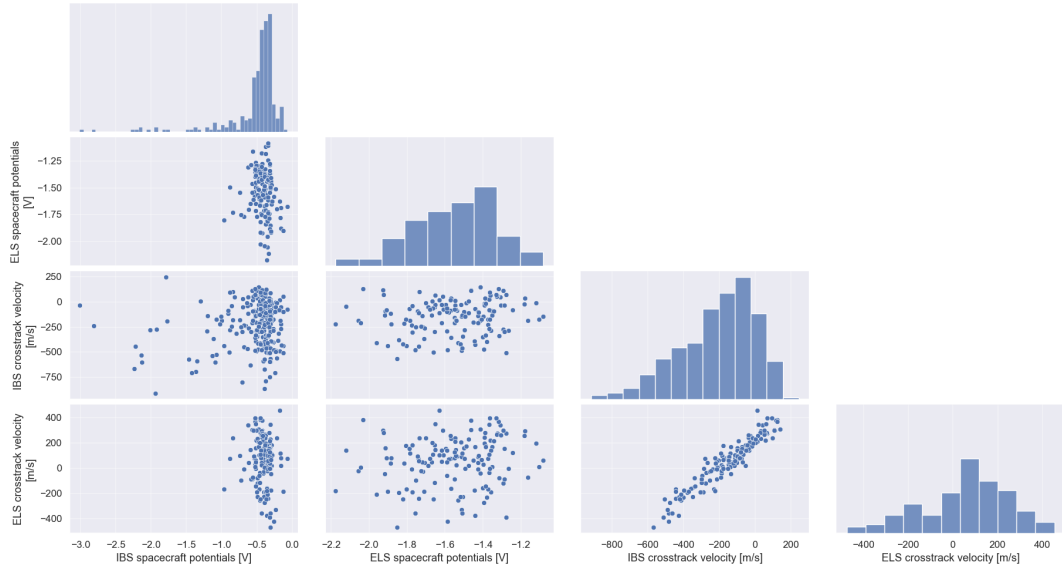


Figure 5.8: A plot demonstrating the investigation of pairwise relationships between derived values. The values shown are derived spacecraft potentials from IBS and ELS, as well as crosstrack velocities from the sensors as well. All derived values are shown, including where ELS values cannot be derived, this causes the distributions to not always be reflected in the scatter plots. As can be seen in the scatter plots there is good correlation between the crosstrack velocities, but no correlations can be seen between the crosstrack velocities and spacecraft potentials.

ogy is good, although there are differences from T48 onwards. These findings are important, as the ion masses have been assumed in this study, rather than using a cross-calibration with known ion masses from the INMS data, as Crary et al. (2009) and Westlake et al. (2014) did. This gives confidence in the validity of the methodology.

Examining the fixed-actuation flybys shown in Figure 5.7, it can be seen that the derived potentials are in agreement with predictions with those extrapolated from Crary et al. (2009) at high altitudes above 1200 km. Below this altitude, the results from Crary et al. (2009) are consistently slightly lower than those found in this study. During the non-actuating T57 flyby the IBS derived potentials can be compared to both values from Westlake et al. (2014) and the extrapolated Crary et al. (2009) values, the values derived in this study are found to lie roughly between them. One source of this discrepancy may be differing ion masses to those assumed in this study.

The major discrepancy is between the separate CAPS sensors and the Langmuir Probe. The pairplot in Figure 5.8 provides an overview of the 4 major values derived in this study. As noted previously, the crosstrack velocities are proportional but no other clear proportionality exists between the other values. The lack of proportionality between the derived spacecraft potentials (Figure 5.8: Panel in leftmost column, second row) is curious, particularly as the data in the referenced panel is restricted to altitudes where potentials can be derived from both positive and negative ions. Furthermore, the observed range of derived spacecraft potentials is quite different for the positive and negative ions. Spacecraft potentials derived from positive ions vary between -0.75 V and -0.2 V while potentials derived from negative ions vary between -0.9 V and 2.25 V.

5.4.3 Spacecraft potential discrepancies

Previous studies have proposed that the offset between the spacecraft potentials derived from Langmuir Probe and IBS data is due to a non-uniform spacecraft potential (Crary et al., 2009). This is due to the Langmuir probe being on a 1.5 metre boom and therefore located away from the spacecraft body and the CAPS instrument. This point is reiterated by Desai et al. (2017) who state that the different surfaces on the spacecraft charge to different negative values in Titan's ionosphere. However, the discrepancy between the derived potentials from IBS and ELS is unlikely to have been caused by any differential charging or a non-uniform spacecraft potential. The CAPS sensors are co-located, covered by a conductive carbon-impregnated Kapton thermal blanket (Crary et al., 2009) and share a common ground, making differential charging unlikely.

There is also the possibility of a complex magnetic field environment having an impact. Zhang et al. (2021) demonstrated that in simulations, reversing the magnetic field direction did flip the spacecraft potential from positive to negative.

The cause of the discrepancy could be related to alongtrack ion velocities, and this possibility is covered in Chapter 6. In brief, this would be related to the CAPS sensors having difficulty distinguishing between alongtrack ion velocities and spacecraft potential. This is highlighted in Figure 6.11 in Chapter 6, where there

is a strong inverse relationship between the alongtrack ion velocity and the spacecraft potential. However, as the best fit lines do not cross in Figure 6.11, which if they did would mean a single spacecraft potential could be found by imposing different alongtrack velocities, a solution that resolves the spacecraft potential discrepancy is not possible.

5.5 Conclusions

Using data from Cassini Plasma Spectrometer (CAPS) sensors, crosstrack velocities have been derived in Titan’s ionosphere for the first time. As CAPS was mounted on an actuator, the angular difference between the expected ion flow direction and the actual flow was interpreted as due to a crosstrack velocity. Crosstrack velocities for positive ions were derived from CAPS Ion Beam Spectrometer (IBS) data, while velocities for negative ions were derived from CAPS Electron Spectrometer (ELS). I found positive ion crosstrack velocities up to 1 km/s at altitudes up to 1800 km. Similarly, I found negative ion crosstrack velocities up to 0.5 km/s at 1000 km. Proportionality was observed between the positive and negative ion crosstrack velocities, agreeing with expectations from cation-neutral-anion collisional coupling. Although proportionality was observed, an offset between the charges was observed, with positive ion crosstrack velocities consistently lower than the associated negative ion velocities.

Spacecraft charging was also investigated, with spacecraft potentials derived from the IBS and ELS sensors. Previous studies have made use of various Cassini instruments to derive spacecraft potentials while Cassini was in Titan’s ionosphere and these are compared. I find that the potentials derived are comparable to previous estimates using the sensors individually, but there is large variation in the potentials between CAPS sensors, which cannot be explained through differential charging. This should be an area of future investigation, with spacecraft charging simulations utilised to understand how the complex cation-neutral-anion chemistry and dynamics of multiple populations can affect the spacecraft charge state.

The findings in this chapter may help future studies that investigate regions

with coupled ion-neutral flows, such as the proposed ESA Daedalus mission, which would take measurements of ion and neutral velocities in the Earth's atmosphere between 100 and 200 km. One of the instruments aboard Daedalus would measure crosstrack velocities.

Chapter 6 covers the alongtrack velocities from this chapter, as well as the connection to the neutral winds previously measured at Titan.

Chapter 6

Ion velocities and spacecraft charging in Titan’s ionosphere: II. Alongtrack velocities and their connection to neutral winds

As Cassini passed through Titan’s ionosphere, the Cassini Plasma Spectrometer made measurements of ion energies. In this study I derive cation and anions velocities parallel to Cassini’s velocity vector. I find that anion and cation alongtrack velocities are proportional to each other, with magnitudes up to 0.5 km/s, in line with expectations from a coupled ion-neutral collisional environment. Through examining the ion flows in the Titan frame, I observe that several flybys display ion flows contrary to previous expectations and propose possible explanations. The findings in this chapter highlight the complexity in deriving alongtrack ion velocities but also represent an interesting example of simultaneous cation and anion measurements in coupled ion-neutral flows. Chapter 5 covers crosstrack ion velocities and spacecraft charging and the work was performed in tandem to this one.

6.1 Introduction

Several studies have observed winds in Titan’s atmosphere, from the stratosphere up to thermosphere/ionosphere (Horst, 2017). Stratospheric zonal winds have been

measured at superrotational velocities of up to 200 m/s (Horst, 2017). Stratospheric meridional wind speeds were measured to be below 1 m/s (Horst, 2017).

Prior to Cassini, attempts were made to understand the thermospheric winds. Rishbeth et al. (2000) estimated thermospheric winds of 60 m/s by considering various terms in the wind equation. Using Cassini Ion and Neutral Mass Spectrometer (INMS) data, Müller-Wodarg et al. (2006) estimated zonal wind speeds of 245 ± 50 m/s from latitudinal density gradients. A later empirically derived model by Müller-Wodarg et al. (2008) found poleward horizontal winds of up to 150 m/s, along with a 50 m/s prograde zonal flow north of 60°N .

During the Cassini mission, the spacecraft made several flybys of Titan, passing through its ionosphere and thermosphere. This allowed several studies to examine ion dynamics from insitu measurements of Titan's ionospheric plasma. Crary et al. (2009) derived ion velocities along Cassini's trajectory using data from the INMS and Cassini Plasma Spectrometer (CAPS) Ion Beam Spectrometer (IBS) instruments that was collected during 14 flybys of Titan. They found values typically in the range of 100 m/s, with 260 m/s being the largest derived value, being comparable in magnitude to the results of Müller-Wodarg et al. (2006, 2008). Cui et al. (2009) used superrotating winds to explain how ions with high destruction rates created on Titan's dayside ionosphere were able to transport to the nightside ionosphere. They modelled winds with an enhanced rotation speed of 100 m/s.

How thermospheric neutral winds might contribute to ionospheric flows is discussed in Cravens et al. (2010). They investigated the relative speeds between the plasma flows and neutral gas speed. They found that the relative speed is approximately 1 m/s at 1000 km but rises to 200 m/s at 1500 km. They showed that the ionospheric plasma is strongly coupled to the neutral population below 1300 km, resulting in the low relative speed. Given the relative velocity of the neutrals and plasma they also suggest the existence of velocity shear/stagnation layers around 1300 km, where the neutral wind and plasma flows might be oppositely directed.

More recently, the Atacama Large Millimeter Array (ALMA) has been used to study the thermosphere of Titan. Lellouch et al. (2019) used ALMA data ob-

tained during August 2016 to measure the Doppler shifts of six molecular species to make direct wind measurements in the thermosphere, up to 1200 km. These neutral wind measurements showed strong prograde winds in the equatorial region that reached 340 m/s at 1000 km. They also found no convincing evidence for meridional or day-to-night flows in the measurements, with upper limits of 25-30 m/s. They suggested the driving mechanisms for the prograde winds were from waves from the upper stratosphere/mesosphere and/or from magnetospheric/ionospheric interaction. Cordiner et al. (2020) reanalysed the August 2016 ALMA data and included May 2017 ALMA data in their study of the equatorial thermospheric jet. They found a 47% reduction in the equatorial zonal wind speed over the 9 months, from 373 m/s in August 2016 to 196 m/s in May 2017. This slowing was interpreted as a dramatic slowing of the jet due to dynamical instabilities.

There have been several attempts to include ion-neutral collisions in models of Titan's ionosphere (Cui et al., 2009; Ulusen et al., 2010, 2012; Snowden and Winglee, 2013; Sillanpää and Johnson, 2015). Snowden and Winglee (2013) used a 3D multi-fluid simulation to study Titan's interaction with Saturn's magnetosphere, with the model including ion-neutral coupling. They found simulated ion velocities for N_2^+ of 600 m/s to 1 km/s near closest approach and compared this to the maximum value of 260 m/s derived by Crary et al. (2009). However, they do note the differences could be due to: the methodology in Crary et al. (2009), that the simulated trajectory samples Titan's flank where the $J \times B$ force is the strongest, or that the model does not include ion species with masses larger than 28 amu, which would lower the average ion velocity. So far, ionospheric models of Titan have not included the equatorial neutral jet found in the ALMA data.

The ionospheric dynamo region at Titan was first investigated by Rosenqvist et al. (2009). This region is defined where electrons still drift perpendicular to the magnetic field but the flow of ions is disrupted by neutral collisions. They found that the dynamo region extended from a lower boundary between 900 and 1000 km to an upper boundary at an average altitude of 1450 km. Several conductivity peaks were found as well, with two Pedersen conductivity peaks and a Hall con-

ductivity peak between them. The Pedersen conductivity peaks were found at the top and bottom of the dynamo region while the Hall conductivity peaked at 1100 km. Further investigation of ionospheric currents and electric fields in this region was performed by Ågren et al. (2011). They measured currents from 10 to 100 nA m² across the T18, T19, T21 flybys, these currents correspond to fields of 0.5 to 3 $\mu\text{V m}^{-1}$. They point out LP measurements measured ionospheric plasma speeds of 1 km/s and this would generate electric fields of 5 $\mu\text{V m}^{-1}$ in accordance with their findings. Conversely, they also state that if neutral winds are the generation mechanism, that the 150 m/s neutral winds would generate electric fields of 0.75 $\mu\text{V m}^{-1}$.

A recent study by Shebanits et al. (2022) investigating the dynamo region utilised the full plasma content by including charged dust. They found that this increases the Pedersen conductivity by 35% compared to previous estimates using electron densities. They also state that the dayside conductivities are 7-9 times larger on the dayside than the nightside due to higher plasma densities, and that these are altered by the solar cycle. At solar maximum, Hall and Pedersen conductivities are higher on the dayside and lower on the nightside, when compared to the solar minimum.

In this chapter, I will cover the methodology of deriving alongtrack ion velocities for both positive and negative ions. I will also cover spacecraft charging effects on the derivation of these velocities using CAPS data. The alongtrack ion velocity measurements will be further investigated in the context of dynamics of Titan's ionosphere and neutral winds in Titan's thermosphere. Chapter 5 covers the derivation of crosstrack ion velocities during the same set of flybys studied here. It also covers results and discussion of the crosstrack ion velocities and the spacecraft potentials.

6.2 Methodology

6.2.1 Alongtrack ion velocities

This methodology has been used previously with Cassini CAPS IBS data to study ion velocities at Enceladus (Chapter 3), and cation velocities, temperatures and composition at Titan, (Chapter 4 and (Crary et al., 2009; Mandt et al., 2012; Westlake et al., 2014)). Similarly this methodology has been applied to CAPS ELS data for anion velocities at Enceladus (Chapter 3) and ion composition at Titan (Coates et al., 2007, 2009; Wellbrock et al., 2013, 2019; Desai et al., 2017; Mihailescu et al., 2020).

6.2.1.1 Method

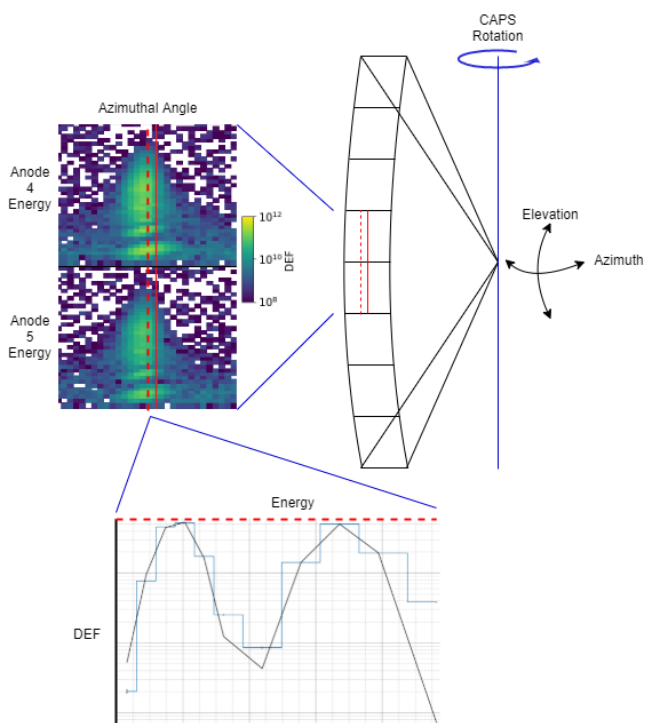


Figure 6.1: A cartoon extending on Figure 5.2. The bottom plot demonstrates the flux fitting process applied across an energy sweep which is covered further in this chapter. The red dashed line on the spectrogram cuts along the y-axis which represents energy, in the bottom plot the energy is shown on the x-axis to allow demonstration of the flux fitting process.

As CAPS was taking measurements of cold plasma, Section 2.4 is relevant for understanding the basic derivation of the alongtrack velocity. Alongtrack velocities were also previously derived in Chapter 4. The methodology in Chapter 4 only

used the energy for peak ion fluxes, rather than a Gaussian fit used here. Figure 6.1 demonstrates how the methodology applied in Chapter 5 was used to find the times of peak ion flux during actuation cycles and therefore the appropriate time to use Equation 2.1. Some terms in Equation 2.1 are known, such as the measured ion energy E_α and spacecraft velocity v_{sc} . Some parameters are fixed, such as ion temperature, which is estimated from empirical linear relationships found between temperature and altitude, reported in Crary et al. (2009). The remaining parameters, ion velocity v_{ion} and spacecraft potential Φ_{sc} are not known.

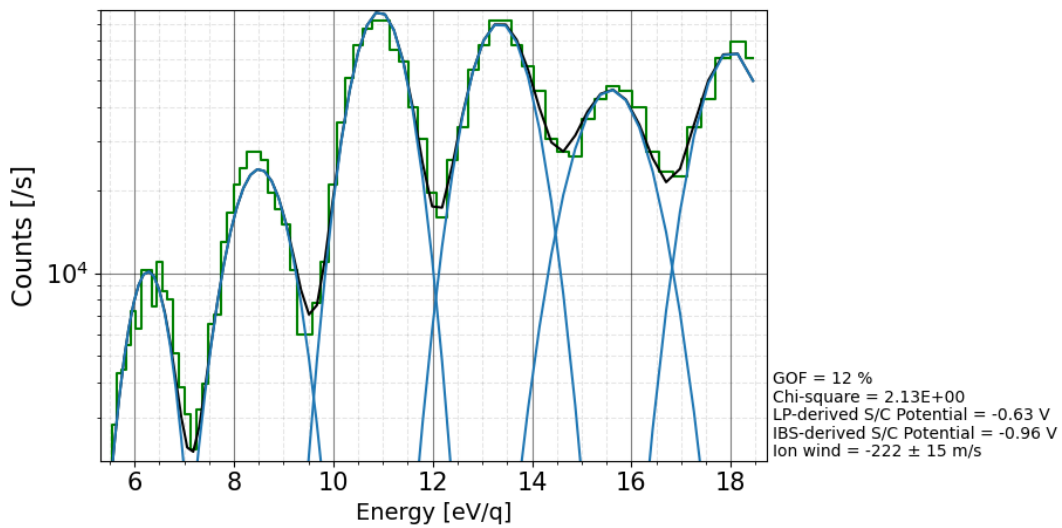


Figure 6.2: An example to illustrate the fitting algorithm to derive positive ion alongtrack velocities from IBS data. On the x-axis, energy/charge is plotted linearly and counts/second is plotted on the y-axis with logarithmic scaling. The IBS data spectrum is shown with a green step plot, with the logarithmic spaced energy bin visible. The energy peaks are not necessarily from the same energy sweep, this is due to the methodology which accounts for if peak fluxes of different ion masses don't appear in the same energy sweep. It then combines the spectra into the single spectrum seen above. Multiple Gaussians curves are shown in blue which are fitted to ion peaks associated with the various ion families observed in the spectra. The best fit of the Gaussians to the data is shown in black. Several statistics are shown in the bottom right, highlighting the derived parameters and goodness of fit (GOF).

To calculate the unknown parameters, Gaussian curves are fitted to the data, as seen in Figure 6.2, with a separate Gaussian curve used for each ion species. The widths of these Gaussians is related to the instrument response and thermal velocity of the ions, although these factors are not utilised in this methodology. The

amplitude and width of the Gaussians was allowed to freely vary to provide the best fit. This is necessary as the Gaussians can broaden due to multiple ion species with similar masses being present, i.e 28 and 29 amu, causing a single broad peak. The centres of these individual Gaussians are used as the measured ion energies, i.e the left side of equation 2.1. The Gaussian curves are summed to form a single model that can be fitted to the data by varying the unknown parameters v_{ion} and Φ_{sc} .

A weighted least squares approach is taken for fitting due to ordinary least squares not fitting appropriately around the troughs between peaks. Additionally, it does not account for scenarios seen at low altitudes, where sometimes the heavier ions have higher densities than the lighter ions, whereas typically the ion density decreases with increasing ion mass. This would result in an ordinary least squares approach attempting to best fit the heavier ions instead of the lighter ions. This is undesirable as the lighter ions are better resolved due to the number of energy bins. The weighting used is inversely proportional to the count rate observed, the higher the count rate of an energy bin, the less weighting is used to minimize the residual at that energy bin.

Using results from Mandt et al. (2012), abundant positive ions were chosen to fit to the peaks observed in the energy spectra. The positive ion masses utilised were 17, 28, 40, 53, 66, 78 and 91 amu. The data spans a wide range of altitudes and at higher altitudes only the lighter ions are seen, with heavier ions appearing at progressively lower altitudes. This required subsets of the masses to be used at different altitudes. For example, above 1600 km, only 17 and 28 amu ions are fitted, while between 1100 and 1300 km all seven ion masses listed are used. While using fewer ion masses to determine ion velocities does increase the uncertainty in the fitting, it does allow interpretation of the velocities over a larger range of altitudes.

For the positive ion mass determination, Mandt et al. (2012) used INMS data which had the capability to determine ion masses independently from ion energy, however INMS was not designed to resolve negative ion masses. Although CAPS IMS can resolve negative ion masses (Young et al., 2004), the energy range was usually limited to prevent saturation and damage to the instrument during the Titan

flybys. Through previous CAPS ELS and laboratory ion-neutral chemistry studies, the ion masses and species of abundant negative ions have been constrained. I use negative ion masses of 26, 50, 79 and 117 amu (Coates et al., 2007; Vuitton et al., 2009; Wellbrock et al., 2013; Desai et al., 2017). Desai et al. (2017) stated that the third ion mass was associated with an ion of 73-74 amu, although this was caveated that at low altitudes (<1244 km) the peak widened and could be associated with higher masses. I found that a mass of 79 amu produced more reasonable fits and would be consistent with a $C_6H_7^-$ anion. Similarly to the positive ions, the number of negative ion peaks fitted inversely scaled with altitude, below 1000 km, all four negative ion peaks were used, between 1000 and 1100 km, three peaks are used, and above 1100 km, only the two lightest ions were used.

6.2.1.2 Uncertainties

There are several uncertainties present in the derivation of the alongtrack ion velocities. As stated previously, the masses used to fit the ion peaks were based on previous studies. The most abundant ions were chosen, but other ions present can cause broadening and shifting of the ion peaks causing uncertainty in the fitting procedure.

Spacecraft charging can add uncertainty, causing both a shift in the measured energy of the ions and particle deflection. Typically during the flybys, a negative potential is recorded, due to the higher mobility of the electrons compared to the ions. This negative potential accelerates positive ions while decelerating negative ions, affecting the measured energy. The use of multiple ion masses means that this effect can be separated from the effect of alongtrack ion velocities, as alongtrack ion velocities cause a mass-dependent shift while potential does not, this can be seen clearly in equation 2.1. However, the use of fewer peaks during the fitting process can mean that the effects of the spacecraft potential and alongtrack ion velocity cannot be separated, resulting in partial correlation between the two terms. This increases the uncertainty at higher altitudes where fewer ion species are seen. As the masses have been assumed in this methodology, if the true ion masses are not the same as reported in Mandt et al. (2012) or change with altitude, the result will

be an inaccurate fitting, so this is a further source of uncertainty.

Another factor of uncertainty is the energy-angle response of the sensors (Linder et al., 1998; Young et al., 2004). This is particularly prevalent for ELS due to its wider azimuthal response. This effect manifests itself by shifting the peak energy of ions as the actuator moves the sensor across the ion beam. The effect is also mass dependent, meaning that the peak flux for different mass ions can appear at different times. To mitigate this, I use the relevant energy bins for each ion mass from the timeslice where the peak flux is observed for that ion.

As alongtrack velocities are measurements of ion velocities parallel to Cassini's velocity vector, it is important to note how changes in Cassini's velocity vector, relative to the surface while it travels through the ionosphere, affects the measurements. For example, at higher altitudes such as 1500 km, the alongtrack velocities will contain a component of the vertical velocities inside the ionosphere, however, towards closest approach this component becomes negligible as Cassini would be moving nearly parallel to the surface. Although vertical velocities are not thought to be large inside the ionosphere, on the order of 20 m/s (Müller-Wodarg et al., 2008), and not the main focus of this study, they will affect the measurements and interpretation.

A minor source of uncertainty from the sensors are the voltages on the electrostatic analyzer plates, which is up to 0.5% of the measured energy (Young et al., 2004). Another source of uncertainty is the intrinsic energy resolution of the instrument, which is 16.7% for ELS and 1.4% for IBS. The energy resolution generates uncertainty as a range of ion masses, velocities and temperature could generate the peak flux within an energy bin. It does also generate an upper limit to the range of values possible, as values outside a certain range would generate the flux peak in an adjacent bin, a point elaborated in Section 4.2.3. This effect is mitigated by using the fitting algorithm which fits across multiple energy bins.

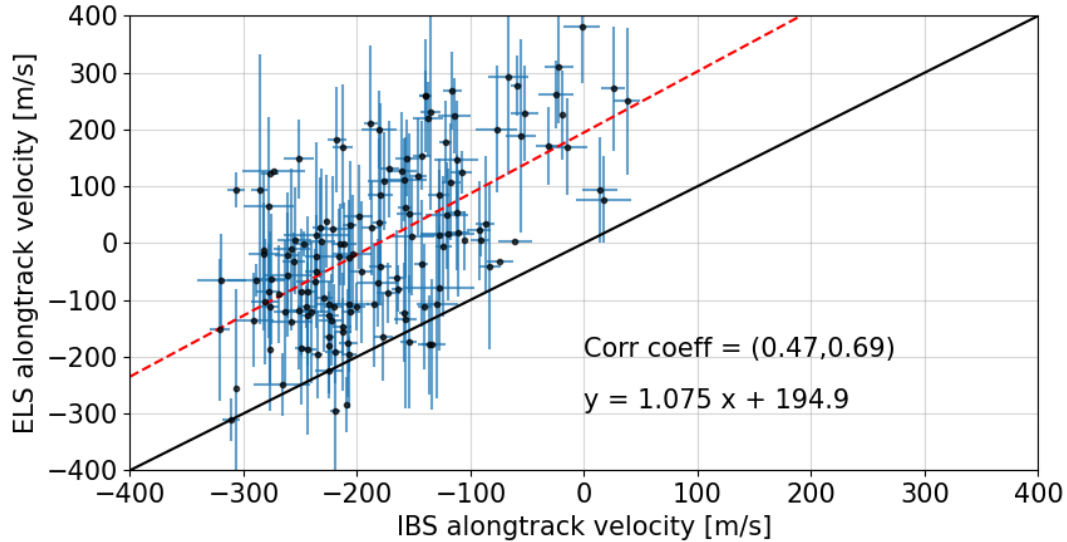


Figure 6.3: The cation and anion alongtrack velocities as measured from CAPS IBS and ELS respectively during the actuating flybys in this study, at altitudes below 1200 km. In the plot text, 95% confidence interval values are shown for the correlation coefficient and the equation describing the best linear regression fit. The fit is shown with the red dashed line. The black line is a $y=x$ line to highlight the offset. As described in the text, there is an offset in the cation velocity distribution towards negative values, while the anion velocity distribution is roughly centred at 0 m/s.

6.3 Results

6.3.1 Actuating flybys

The distribution of cation and anion alongtrack velocities measured during the actuating flybys can be seen in Figure 6.3. The distribution of the negative ion velocities measured by ELS is centred around 0 m/s. However, the positive ion velocity distribution is off-centre from 0 m/s, with a peak around -200 m/s, indicating the measurements are largely of tailwinds in the spacecraft frame. The two distributions are linearly fitted to examine the relationship between the derived parameters. As can be seen, the distribution is close to a unity gradient, with a gradient of 1.075 and has some proportionality to it. The off-centred positive ion distribution is also shown in the linear fit with the shift along the y-axis of 195 m/s.

The velocities derived are also shown categorically, with each flyby shown on the x-axis in Figure 6.4. Positive velocities in this plot correspond to headwinds in the Cassini frame, conversely, negative velocities in this plot are tailwinds. As can

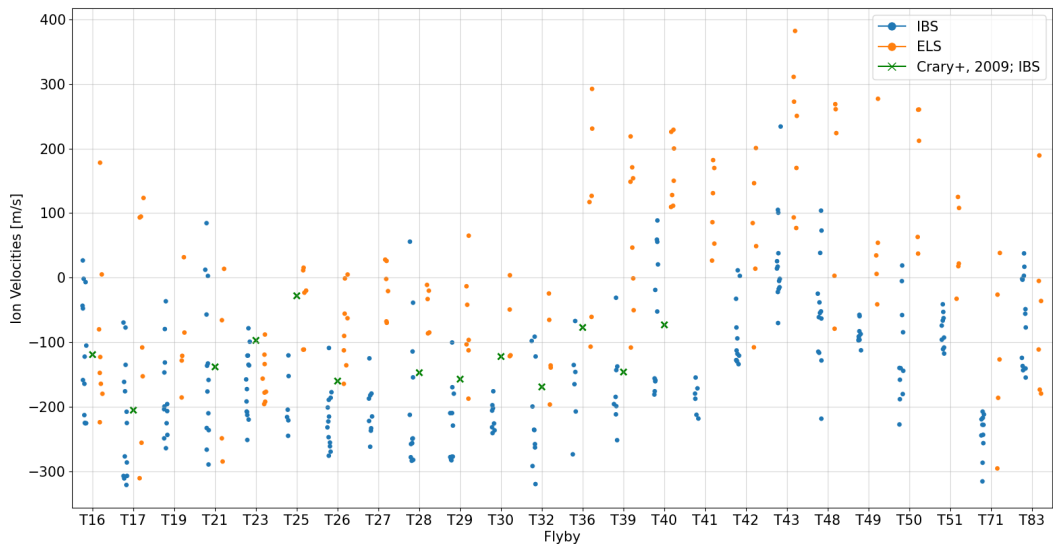


Figure 6.4: A plot displaying the derived alongtrack ion velocities from ELS and IBS from the actuating flybys below 1500 km. The negative ion alongtrack velocities are shown in orange while positive ion alongtrack velocities are shown in blue. The markers are offset in the x-axis from the flyby labels for clarity. Previously derived velocities from Crary et al. (2009) are shown in green crosses, these values were obtained at closest approach. As can be seen, the cation alongtrack velocities are dominated by negative values, indicating tailwinds in the spacecraft frame.

be seen, the derived alongtrack cation velocities are dominated by negative values. This occurs more frequently for the positive ions, a reflection of the distribution displayed in Figure 6.3. As can be seen, there is a distinct change in the derived values from T43 to T51, which will be further explored later. Values derived by Crary et al. (2009) at the closest approach during these flybys are plotted in green. These values are comparable to those derived from IBS data in this study for the majority of flybys, with the direction, i.e headwind or tailwind, agreeing for all flybys, and mostly agreeing in terms of velocity magnitude.

6.3.2 Fixed actuation flybys: T55-T59

Five non-actuating flybys, T55-T59, which took place in May-July 2009 are studied here. The general structure of the cation alongtrack velocities with respect to altitude is broadly the same across the flybys, as can be seen in Figure 6.5, with positive alongtrack velocities seen at high altitudes then transitioning to negative velocities around 1300 km. T55, T56 and T57 have a third region at low altitudes

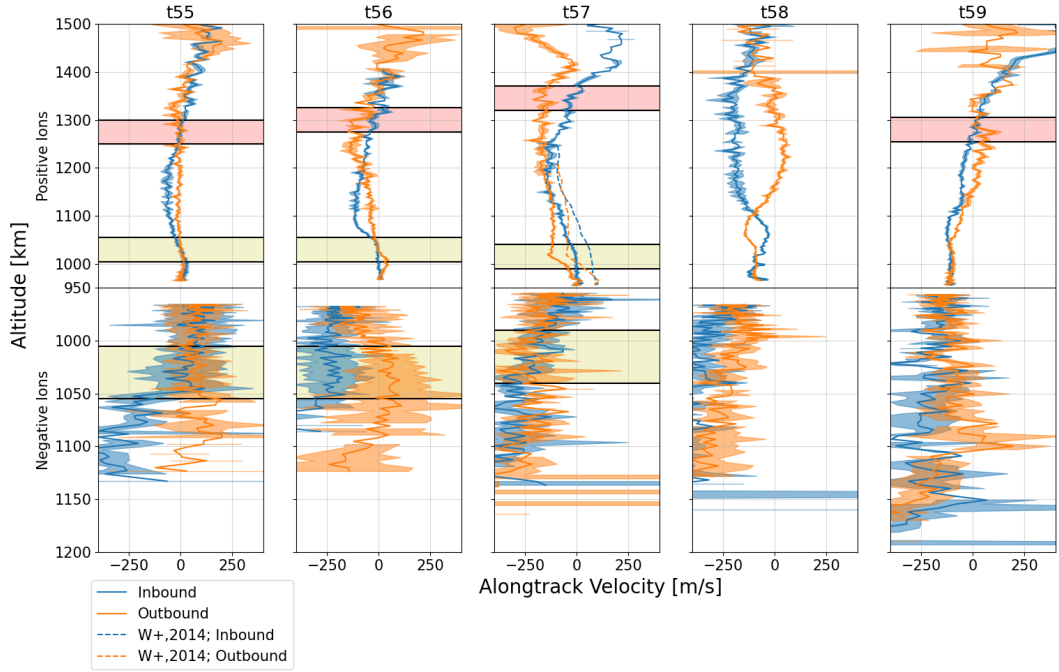


Figure 6.5: A diagram showing alongtrack ion velocities against altitude as derived from the five actuating flybys in this study. The top row shows positive ion measurements, the bottom row shows negative ion measurements. Inbound measurements are shown in blue, outbound in orange. Positive ion velocities as derived by Westlake et al. (2014) during the T57 flyby are shown with dashed lines. The red and yellow shaded regions are altitudes where transitions occur in the direction of the alongtrack velocity measured.

below 1000 km where alongtrack velocities turn positive again. For T57, velocities are also plotted from Westlake et al. (2014), which are seen with a positive offset to the velocities measured in this study.

The anion velocity structure is not as clear, with much larger uncertainties associated with the alongtrack velocity measurements. There is not a clear transition between the altitudes as seen with the cations. Generally the magnitude of the anion alongtrack velocities scale with altitude, e.g low velocities at low altitudes, high velocities at high altitudes.

6.4 Discussion

6.4.1 Ion velocity distributions and magnitudes

6.4.1.1 Actuating flybys

The data shown in Figure 6.3 displays a strong correlation between the alongtrack velocities for the positive and negative ions. This is not surprising, as these velocities are taken below 1200 km, where strong ion-neutral coupling occurs through collisions. Previously, Cravens et al. (2010) noted that the plasma is strongly coupled to the neutrals below 1300 km. Although these studies only studied cation-neutral collisions, densities of anions are similar or less than the cations (Wellbrock et al., 2013), meaning the anion-neutral coupling should be as strong as, or more, than the cation-neutral coupling. This implies that at these altitudes, the cation-neutral-anion flow should appear to move at one bulk velocity, and that any change in one flow will affect the others. On the other hand, the offset in the distribution implies that there may be other effects meaning that the positive ions are moving differently than the negative ions within this bulk flow.

This offset can be seen to vary with flyby, as seen in Figure 6.4, which shows the measured ion velocity by flyby. In Figure 6.4 most of the IBS findings are in agreement with findings from Crary et al. (2009), with the Crary values being typically within the range of values found in this study. Some flybys do display discrepancies, including T25 and T30, where the Crary values are notably higher than those derived here. Comparing between the cation and anion alongtrack velocities, we can see they are similar for some flybys, for example, T16 and T17 do not show any large differences in the distributions, while other flybys such as T41 show a large difference. For T41, all the anion velocities are positive and all the cation velocities are negative, indicating that during this flyby along Cassini's trajectory, the ions are moving in opposite directions.

Interpreting these alongtrack velocities in the Titan frame has several caveats. This is due to the previously described uncertainties but primarily that these measurements are sampling along the Cassini velocity vector, so represent a 1D mea-

surement rather than a true 3D measurement of the velocity vector. Furthermore, the 1D measurement is not sampling purely meridional, zonal or vertical components in the Titan frame, so any extrapolation needs careful treatment. However, the impact of vertical velocities are expected to be small (on the order of 10 m/s). Müller-Wodarg et al. (2008) found larger meridional flows up to 150 m/s but these were under the assumption of zero winds at 960 km. When winds were added at 960 km, the peak meridional flow dropped to 90 m/s. Lellouch et al. (2019) stated upper limits for neutral meridional flows at 25-30 m/s from ALMA measurements.

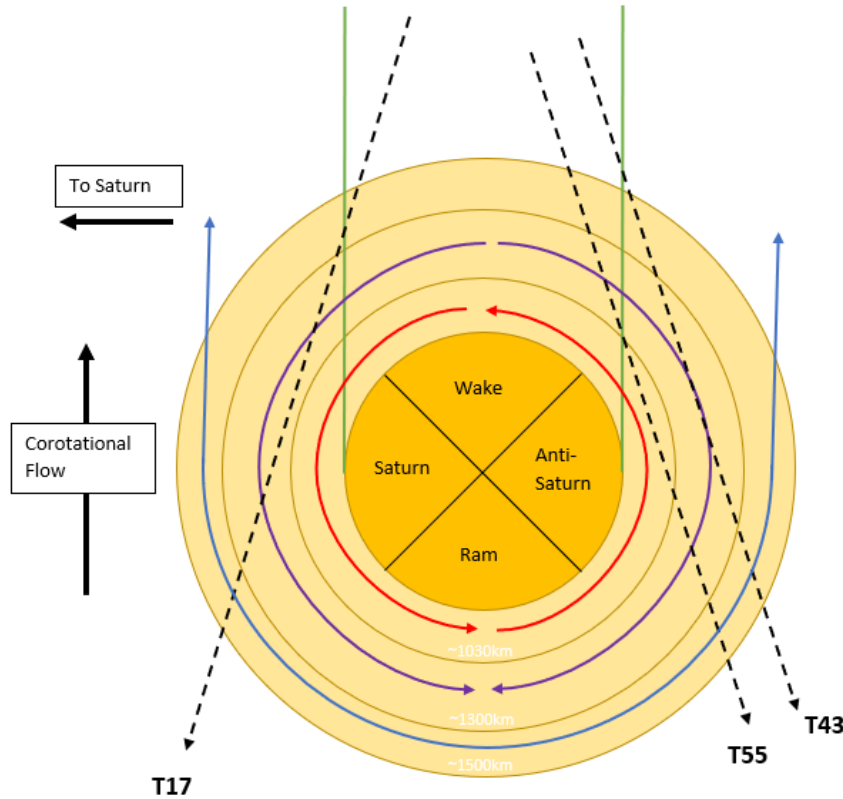


Figure 6.6: A cartoon demonstrating trajectories of Cassini flybys through Titan's ionosphere. Trajectories of three Titan flybys: T17, T43 and T55 are shown, with T17 passing Titan on the Saturn-facing sector and the other two passing on the opposite side. Shells are overlaid on Titan indicating different atmospheric layers. The innermost layer, with red arrows, indicates the portion of Titan's atmosphere which corotates/superrotates with the moon. The next layer, with purple arrows, displays different characteristics while the last layer, with blue arrows, has velocities consistent with loss to Saturn's magnetosphere. The green lines indicate the geometric wake of Titan.

With knowledge of the flyby trajectories, some insight can be gained on the meridional/zonal components. In the Titan frame during Cassini flybys, Cassini

typically travels from the wake side of Titan to the ram side, as illustrated in Figure 6.6. In the cartoon, several atmospheric layers are shown, with the innermost layer with red arrows indicating the layer that corotates/superrotates with Titan, out to the blue arrow layer which is lost to Saturn's magnetosphere. The cartoon also shows the 4 sectors used to separate the flybys in this study, with the ram and wake sides being related to the corotation flow in the magnetosphere. The other two sectors are the Saturn-facing side and anti-Saturn facing side, which are fixed due to Titan being tidally locked with Saturn.

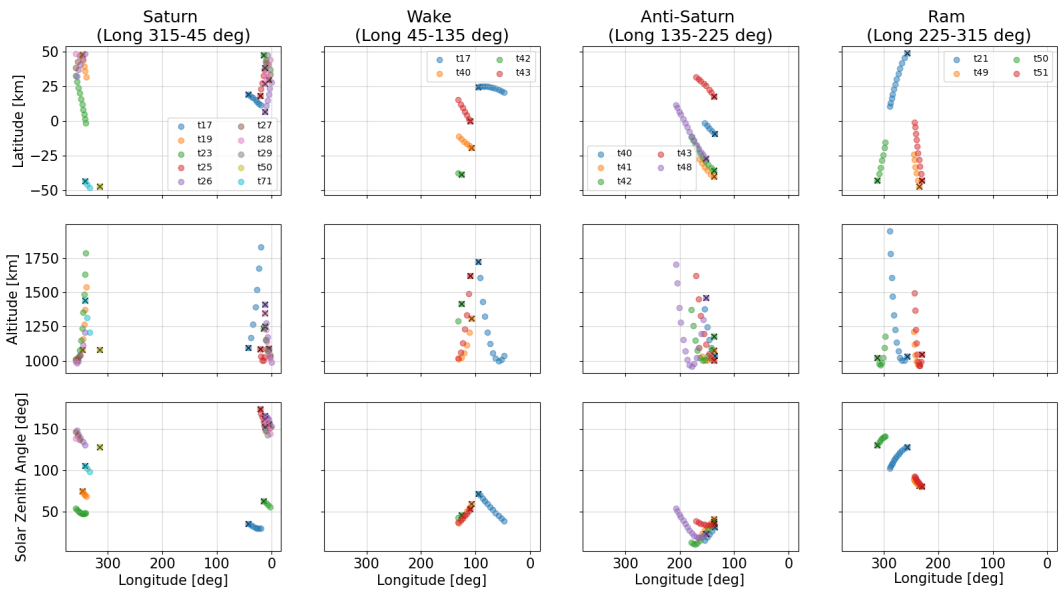


Figure 6.7: Datapoints from the low-latitude actuating flybys used in this study. The four columns are arranged by the 4 longitude sectors described in the text with longitudes plotted on the x-axis. The top row has the latitude on the y-axis, with altitude and solar zenith angle on the middle and bottom rows respectively.

The equatorial neutral jet was described by Cordiner et al. (2020) with a Gaussian fit across latitudes at an altitude of 990 km, with the jet having a FWHM of 70 degrees in 2016 and 101 degrees in 2017. To compare with this jet I restrict the data points used to within 50.5 degrees of the equator, the greatest extent of the jet found so far. This also follows from the results of Müller-Wodarg et al. (2006) who state that the atmosphere is expanded towards equatorial latitudes, with an isobar near 1400 km being located around 120 km higher at equatorial regions compared to the poles. The characteristics of the flybys are shown in Figure 6.7, which displays the

longitude, latitude, altitude and solar zenith angle of the flybys used, with an aim to compare the velocity trends with different characteristics. Figure 6.8 shows the positive ion alongtrack velocities as arranged by the 4 sectors described. I highlight the difference between datapoints gathered on the Saturn-facing and anti-Saturn facing sectors.

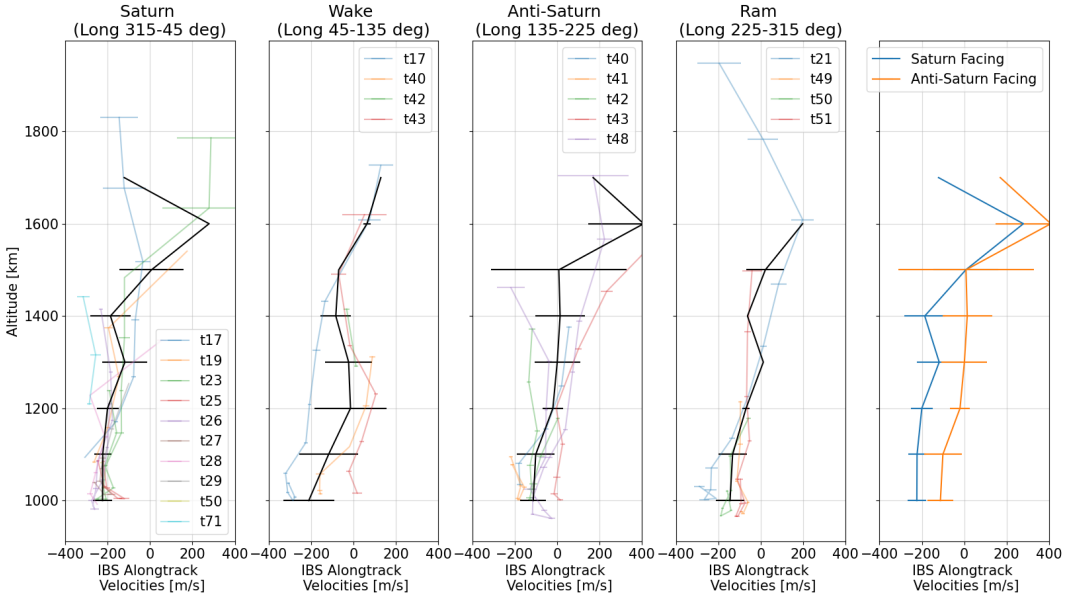


Figure 6.8: Alongtrack positive ion velocity measurements of the low latitude (within 50.5 degrees of the equator) actuating flybys, separated by sector in the first four panels. The four 90 degree longitude sectors are the Saturn-facing, wake side (the wake caused by the corotational flow in the magnetosphere), anti-Saturn facing and ram sector. In each panel ion velocity measurements from flybys are shown with errorbars in colour, with an average shown in black. The lines plotted are binned in altitude, with each bin being 100 km, the lowest bin is centred at 1000 km. The errorbars on the black lines indicate the standard deviation of the data points in that altitude bin. Some flybys can span multiple panels, if that flyby crossed multiple sectors. The fifth panel shown highlights the averages found on Saturn-facing and anti-Saturn facing sectors studied.

Although we do not purely sample a meridional or zonal component, some trends can be inferred with knowledge of Cassini's trajectory. For zonal components, if Cassini passes on the Saturn-facing side, then tailwinds in the Cassini frame are associated with eastward winds, conversely on the anti-Saturn facing side Cassini tailwinds would be associated with westward winds. Depending on the Cassini trajectory, northward or southward meridional winds may also be measured in the alongtrack velocity. Examining the rightmost panel in Figure 6.8 there is a

clear difference below 1500 km of the positive ion alongtrack velocity measurements between the Saturn-facing and anti-facing sectors, with the Saturn-facing flybys recording stronger tailwinds in the Cassini frame.

While the results from the Saturn-facing side could be expected from the neutral flow, i.e the negative alongtrack velocities being associated with the eastward neutral flow, the westward velocities on the anti-Saturn facing side are unexpected and indicate there might be a westward driving force in this region of Titan's ionosphere.

For the ram and wake sectors, the trends broadly follow depending on whether Cassini passed on the Saturn-facing/anti-Saturn facing side. For example, T17 passed through the wake sector and then through the Saturn-facing sector and the wake sector values reflect this. T43 also passed through the wake sector before passing on the anti-Saturn facing sector and the T43 values were largely above 0 m/s during the passage through the wake sector. This trend is likely due to the trajectory of Cassini.

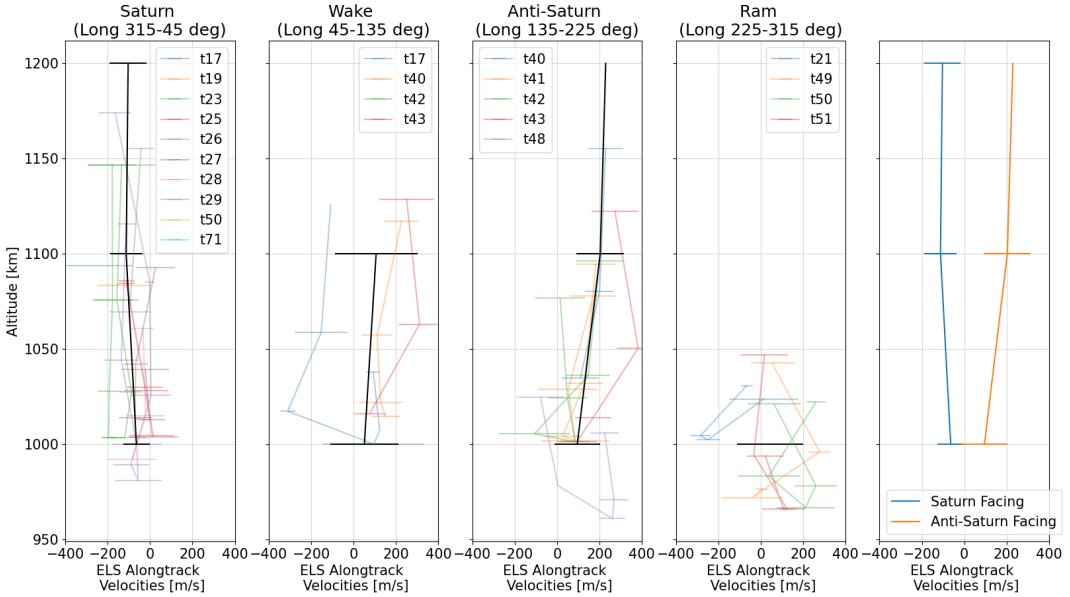


Figure 6.9: The same as Figure 6.8 but for negative ion measurements.

For the negative ion alongtrack velocities, there are fewer datapoints to analyse (see Figure 6.9), due to the measurements only being available at lower altitudes. On the Saturn-facing sector, similar results to the positive ions are found for the

negative ions, with tailwinds being found corresponding to eastward winds. This would indicate that both are being affected by neutral flows in the same way, with the difference between positive and negative ion velocities being caused by other effects. However, notably, on the anti-Saturn facing side, the alongtrack velocities for the negative ions are positive, in contrast to the positive ions. This also puts the negative ion measurements in line with expectations from neutral flows.

6.4.1.2 Non-actuating flybys

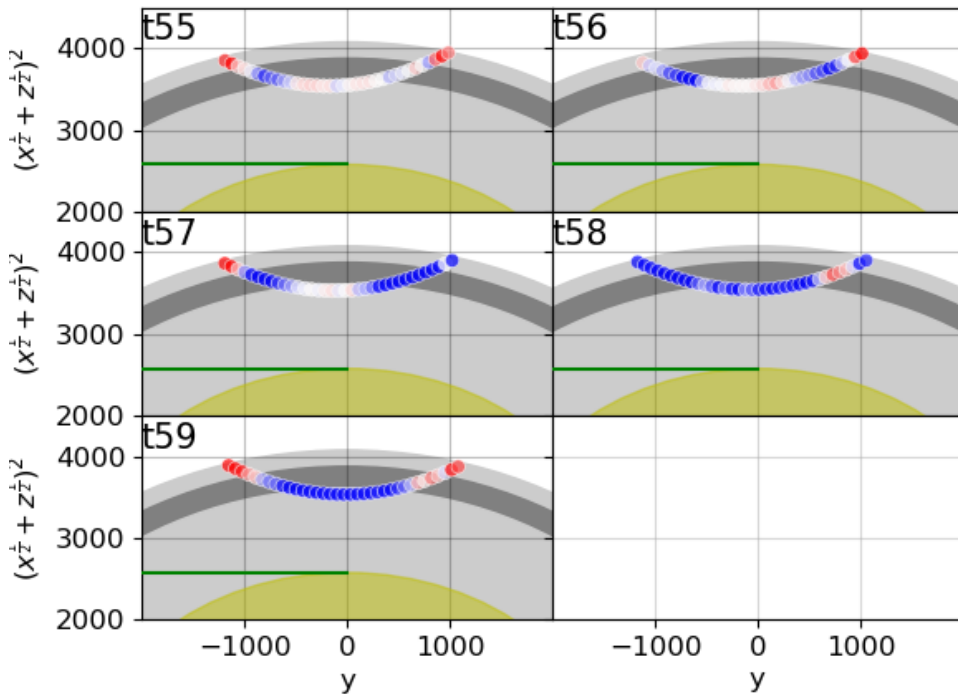


Figure 6.10: Plots of the 5 fixed actuation flybys in cylindrical coordinates. The surface of Titan is shown in yellow, with atmospheric/ionospheric boundaries at 1030 and 1300 km shown in grey. The dots shown are every tenth point during the flyby under 1500 km, with Cassini moving in a +y direction, the colour is indicative of the magnitude and direction of the alongtrack cation velocity. Red colours indicate a headwind in the spacecraft frame while blue indicates a tailwind, with white being zero wind measured. During these flybys the headwinds contain a mixture of eastward and northward velocities while tailwinds are a mixture of westward and southward velocities.

The difference between derived values from Westlake et al. (2014) and this study during the T57 flyby is likely due to a lower derived spacecraft potential

in this study. As seen in Chapter 5, the spacecraft potential derived in this study diverges from that measured by Westlake et al. (2014) below 1300 km. By closest approach, the spacecraft potential measured here is 0.14 V lower than that measured by Westlake et al. (2014), -0.35 V against -0.21 V. However, both these values are still higher than that measured by the Langmuir probe, but the value in this study is closer to the predicted value of -0.37 V by Crary et al. (2009). This discrepancy was investigated further in Chapter 5, but does highlight the difficulties in separating alongtrack velocities from spacecraft potential measurements. As the Westlake et al. (2014) values follow a similar trend to the values derived here, the interpretation of the ionospheric structure does not change but only the altitudes where these transitions occur.

Edberg et al. (2011) reported a region of high plasma densities during the T57, T58 and T59 flybys in the tail/nightside of Titan. These high densities moved progressively down the tail and was composed of a mixture of light and heavy ions from the ionosphere. Although this region was observed down the tail, at altitudes between 4000 and 15000 km from Titan, it is worth noting the variations between the data observed at low altitudes in the ionosphere and high altitudes in the tail, as the high density plasma originated in the ionosphere. During the T55 and T56 flybys where no high plasma densities are observed, very little variation is seen at the low altitudes. The velocity profile with altitude of these flybys, as seen in Figure 6.5 and Figure 6.10, is very similar. From T57 to T59 more variation is seen in the profiles, T58 for example shows no transition from positive to negative alongtrack velocities at the same altitude as the other flybys. No one mechanism is proposed by Edberg et al. (2011) to explain the phenomena, so I will not go in depth into a comparison trying to link the structures here to those observed at higher altitudes. However, in summary, the plasma lost from the ionosphere between the T56 and T57 flybys and then subsequently observed in the tail during T57 and later flybys might be linked to the variation observed in the velocity profiles observed at lower altitudes. A full investigation on how varying ion velocities in the ionosphere would drive plasma outflow is outside the scope of this chapter.

6.4.2 Corotational Flow

Titan lacks an intrinsic magnetic field and is directly exposed to the corotational flow of plasma in Saturn's magnetosphere. The direction of Titan's plasma tail has been observed to vary along the Saturn-Titan line with changing magnetospheric flow conditions (Bertucci et al., 2007).

Ledvina et al. (2012) examined the orientation of the dayside ionosphere with respect to the incident flow and found no global change of Titan's interaction with Saturn's magnetosphere. They also describe a more sharp density transition on the Saturn-facing side with a more diffuse transition on the anti-Saturn facing side.

A study by Chen and Simon (2020) used magnetic field data to study the magnetic field pile-up region around Titan. They found, consistent with earlier studies, that there is an asymmetry between the Saturn-facing and anti-Saturn facing hemispheres, with the pile-up region being extended further on the anti-Saturn facing side. They concluded this is due to the large gyro-radii of the pick-up ions and as the convective field points away from Saturn along the Saturn-Titan line, this increases the pile-up region on the anti-Saturn hemisphere.

This difference could be related to the observed difference in this study between the Saturn-facing and anti-Saturn facing sectors. The asymmetry in the magnetic pile-up would cause different compressional factors in the ionosphere meaning that the Cassini flybys may be observing different ionospheric layers on either side of Titan at the same altitude.

6.4.3 Electrodynamic dynamo region

The dynamo region is a region of an ionosphere where ion flows are disrupted by collisions with neutrals but electrons are drifting perpendicular to electric and magnetic fields (Rosenqvist et al., 2009). The lower bound is where the electron-neutral collision frequency is equal to the electron gyrofrequency and the upper bound is where the ion-neutral collision frequency is equal to the ion gyrofrequency. At Titan this region exists from 1000 km up to 1450 ± 95 km (Rosenqvist et al., 2009). Two peaks in the Pedersen conductivity have been found, one below 1000 km and another situated at 1300-1400 km (Rosenqvist et al., 2009; Shebanits et al., 2022).

Between these altitudes, Hall conductivity is found to be the dominant horizontal current (Shebanits et al., 2022).

In the Earth's ionosphere, low latitude zonal drifts are found to be westwards during the day (Fejer, 2011) in the F region (between 300 and 500 km). These are found with typical speeds of 40 m/s and are independent of season and solar flux (Fejer, 2011). At 110-120 km there is a narrow band of current flowing eastward in the equatorial regions known as the equatorial electrojet.

Sangalli et al. (2009) made measurements of the ion velocity, neutral wind velocity and electric field vectors in the collisional transition region of the Earth's ionosphere. Making measurements between 92 and 198 km allowed them to study the transition between the collision dominated region of the ionosphere between 92-105 km and the $E \times B$ dominated region between 150-198 km. They found that the ion cyclotron and ion-neutral collision frequencies are equal at an altitude of 118 km, marking the centre of the transition between the regimes, the transition ranges approximately from 105 to 122 km.

I state these findings as a comparison to Titan, in that Cassini was observing a similar region of the lower thermosphere/ionosphere, where the collisional transition region is observed. Here I perform a simple examination of the ion-neutral collision frequency and ion gyrofrequency in Titan's ionosphere using equation 1.9. I use N_2 density measurements from Waite et al. (2006) and ion densities from Mandt et al. (2012) to examine $\kappa = \frac{\Omega_i}{\bar{v}_{in}}$, the ratio of ion gyrofrequency against ion-neutral collision frequency. By applying a linear fit against the derived κ values, we find that κ is unity at 1460 km, similar to the values of 1450 ± 95 km from Rosenqvist et al. (2009) and 1390 ± 90 km from Shebanits et al. (2022).

The low-latitude flybys in the anti-Saturn sector were all under illuminated conditions, so it is not possible to conclusively say if solar flux is driving the westward velocities. It is also outside the scope of this study to perform a full comparison between the various conductivities in the dynamo region and the current state of knowledge of these layers at Earth.

6.4.4 Driving from below and circulation cells

Previous studies have found waves in Titan's thermosphere/ionosphere from in situ data (Müller-Wodarg et al., 2006) and interpreted the presence of the equatorial neutral jet and its associated dynamics with waves (Lellouch et al., 2019; Cordiner et al., 2020).

Müller-Wodarg et al. (2006) interpreted strong variations in N_2 and CH_4 densities above 1025 km as vertically propagating waves. They state that the waves could deposit momentum in Titan's thermosphere and that waves breaking up can alter zonal wind speeds, potentially even reversing the wind direction. However, they state they cannot determine the zonal wind direction from their study. The study did show that the thermosphere is strongly influenced by the atmosphere below.

Lellouch et al. (2019) suggest that the equatorial neutral jet of 340 m/s at 1000 km is a response to vertically propagating waves launched at upper stratospheric/mesospheric levels. They do state that this is a complex issue similar to Venus, with wave forcing being superimposed on top of solar influences. Cordiner et al. (2020) also attributed variability in the equatorial neutral jet to a reduction in wave breaking following from a reduction in gravity waves generated in the middle atmosphere. This variability was measured as a 47% reduction in equatorial wind speed over a 9 month period, indicating a dynamic jet system was present.

As these neutral flows are collisionally coupled to the ions, particularly at the lower altitudes, any variability in the neutral flows would likely be observed in the ion data. This could contribute towards the large variability in ion velocities measured, both in magnitude and direction.

Müller-Wodarg et al. (2008) modeled a circulation cell in the atmosphere, with upwelling over the equator, followed by poleward flows and then subsidence at the polar region. The existence of westward velocities would also lead to converging/diverging flows, with flows appearing to reverse at different altitudes, this could be indicative of a circulation cell existing.

6.4.5 Instrumentation uncertainties

One major uncertainty is the (anti)/correlation between the (negative)/positive ion velocities and the derived spacecraft potential. As stated previously, this occurs when few ion peaks are used during the fitting process. Figure 6.11 highlights this issue and how it affects the derived velocities for positive and negative ions differently. As can be seen, the trend is nearly horizontal for the positive ions, meaning that any correlation that may exist between the derived spacecraft potential and positive ion velocity is small. If there was a correlation, the fit would be expected to have a positive gradient, as increasing the spacecraft potential would reduce the ion energy which would need to be counterbalanced by an increased ion velocity to produce the observed energy.

The derived negative ion alongtrack velocities have a very clear trend with spacecraft potential. When higher alongtrack velocities are derived, lower spacecraft potentials accompany them. The confidence interval on this fit is small as well. This indicates that the algorithm has difficulty in separating between the two parameters and this may affect some parts of the interpretation. The parts affected would be related to the direction and magnitude of anion alongtrack velocities at any one instance, as a large positive velocity might just be due to a fit producing a large negative spacecraft potential. If the energy resolution and understanding of expected negative ion masses was improved, the negative ion fit would hopefully become horizontal like that of the positive ions.

However, this correlation only explains the gradient of the fits and does not explain the discrepancy between the derived potentials, i.e the y-offset between the fits.

As stated in the methodology section, several uncertainties are present from the sensors used in the study. One factor that may be important is the 3.4% difference between the recorded energy and nominal energy as measured by Vilppola et al. (2001). Vilppola et al. (2001) state that this means the analyzer gap is somewhat larger than the design value. It is not currently known whether this persisted during Cassini's mission, or if this was accounted for in reported energy bins. If a similar

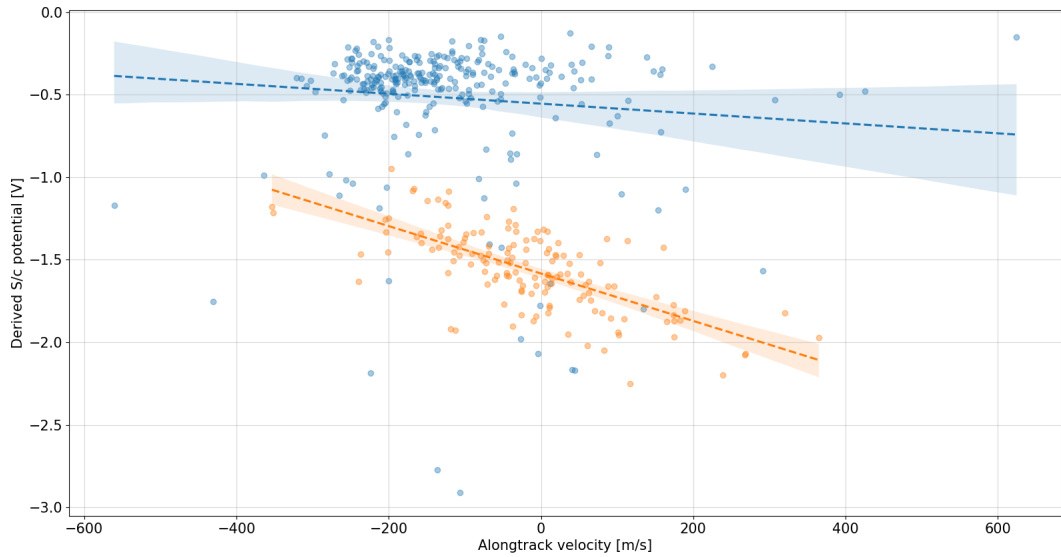


Figure 6.11: A diagram showing the derived spacecraft potentials on the y-axis and the derived alongtrack ion velocities shown on the x-axis. Negative ion values derived from ELS are shown in orange while positive ion values derived from IBS are shown in blue. A linear regression is also plotted with the shaded regions representing a 95% confidence interval of the regression line. As can be seen, there is no correlation between the potentials and alongtrack ion velocities for the positive ions, while there is a strong correlation for the negative ions.

or larger difference existed, this could partially explain the unexpected positive ion alongtrack velocities.

One way to verify the calibration of IBS would be cross-calibration with other Cassini sensors. This was briefly investigated, but not reported here as it is outside the scope of this study. However, difficulties were encountered as IBS was designed with the highest energy resolution, so cross-calibration involves utilising lower energy resolution but better understood sensors. Secondly, this calibration would need to be performed in a more stable and well understood environment compared to Titan's ionosphere, diminishing the applicability. Future modeling attempts may be the best way to resolve this issue.

6.5 Conclusions

In this study I have covered several aspects of Cassini Plasma Spectrometer data collected during its transits through Titan's ionosphere. I present to the best of my

knowledge, the first attempt at derivation of alongtrack velocities of negative ions in Titan’s ionosphere. Alongside this I also present alongtrack velocities of positive ions across 31 flybys that took place between the years 2006 and 2012.

These derived ion velocities are compared to recent results from the ALMA telescope which made measurements of neutral winds in Titan’s thermosphere. While the magnitudes of the ion velocities are found to be comparable, up to 1 km/s, the structure of the ion velocities in the thermosphere do not agree. Ion velocities indicating a westward ion movement were inferred on the anti-Saturn facing hemisphere of Titan. Although due to measurement uncertainty, it cannot be wholly verified, I offer several explanations for the presence of such velocities such as dynamo region effects. Future work continuing from this study could include a study on how seasonality at Titan might influence these ion velocities as well as the ALMA data.

Future lab studies of negative ions should be conducted to better constrain what negative ions are plausible, thereby improving future ELS data fitting attempts and resulting in less correlation between spacecraft charging and spacecraft potential. Additionally, better constraints on spacecraft charging would help improve along-track velocity derivations and mass determination.

Chapter 7

Conclusions and Further Work

7.1 Summary & Conclusions

The research in this thesis has covered topics on ion dynamics and ion composition at the Saturnian moons of Enceladus and Titan. The first study in this thesis, in Chapter 3, investigated the Enceladus plume, discovering two water ion populations with varying velocity characteristics that had been previously interpreted as a compositional difference. The second study, in Chapter 4, looked at the composition of heavy positive ions in Titan's ionosphere, reporting potential identifications for some of the high mass ions. The third and fourth studies, in Chapters 5 and 6, combined the methodologies and ideas of the first two studies to investigate ion velocities in Titan's ionosphere as well as Cassini spacecraft charging.

7.1.1 Enceladus

Enceladus's most notable feature is the water plume that emanates from its south polar region. Cassini made several passes through the plume during its tour of the Saturn system. The study in Chapter 3 investigated charged particle data obtained from two passes through the plume and drew the following conclusions:

- Two separate positive water ion populations were found within the plume, likely originated from two neutral populations previously found within the plume. This represents an alternative interpretation to that presented in Tokar et al. (2009) who suggested a compositional difference. The interpretation presented here provides better correspondence with findings in the neutral

phase, modeled EM fields and the energy resolution of CAPS.

- One population corresponded with a slow thermalised emission while the other was related to a fast gas emission within the plume, in line with findings in the neutral phase (Teolis et al., 2017).
- Negative ion velocities were also measured, with velocities found to be nearly stagnant in the plume but decelerated compared with the neutral and positive ions, representing the first attempt to measure these velocities within the plume.
- The combination of the recorded positive and negative ion velocities provides further evidence of a directed electric field within the plume. This extends on previous studies such as Sakai et al. (2016) and Farrell et al. (2010).

7.1.2 Titan

Titan is the largest moon of Saturn, notable for its extended thick atmosphere that contains complex hydrocarbons. Cassini made flybys through the thermosphere and ionosphere of Titan, allowing in situ measurements of the charged particle environment. The studies covered by Chapters 4, 5 and 6 detail measurements by CAPS of these ions and the derived findings from them, covering topics such as ion composition, dynamics and velocities. The conclusions on ion composition are:

- Up to 275 u/q, a clear grouping structure of the ion masses was found among the positive ions in Titan's ionosphere. This extends the previous study by Crary et al. (2009) to higher positive ion masses.
- The structure of all abundant positive ions were found to be consistent with polycyclic aromatic compounds (PAC), such as polycyclic aromatic hydrocarbons and polycyclic aromatic nitrogen-bearing hydrocarbons.
- The spacing between abundant ions was found to be 12 or 13 u/q, consistent with a C or CH addition as a growth pathway of the PAC molecules.

- The abundant ions were found at similar masses to reported abundant molecules in the neutral phase (López-Puertas et al., 2013), strengthening the case for the correct identification of PACs.

The conclusions on Titan ionospheric dynamics are as follows:

- Crosstrack velocities were derived for both positive and negative ions within Titan’s ionosphere for the first time. This was accomplished by measuring the angular separation between the expected arrival direction of ions with the observed direction.
- Positive ion crosstrack velocities of up to 1 km/s were found at altitudes up to 1800 km, while negative ion crosstrack velocities up to 0.5 km/s were found up to 1000 km. Proportionality was found between the derived positive and negative crosstrack velocities, this shows that a three phase cation-neutral-anion collisional coupling exists in Titan’s ionosphere.
- Alongtrack velocities, which are velocities parallel to Cassini’s trajectory were also derived for both positive and negative ions. This builds on previous work but expands in scope by covering more Titan flybys, as well as interpreting the alongtrack velocities in a wider Titan context.
- Positive ion alongtrack velocities of up to 0.6 km/s at altitudes up to 2000 km were derived, alongside negative ion alongtrack velocities of up 0.4 km/s up to 1200 km. Similar to the derived crosstrack velocities, the positive and negative alongtrack velocities are found to be proportional to each other, another piece of evidence demonstrating ion-neutral collisional coupling.
- Interpreting these velocities in Titan’s ionosphere led to the realisation of an unexpected region in Titan’s ionosphere, illustrated in Figure 6.6, where the ion velocities were opposite in direction to the expected direction from ionospheric superrotation. This disagrees with the neutral thermosphere superrotation as measured by ALMA and the previously demonstrated ion-neutral coupling.

Spacecraft charging was also investigated during the Titan ion dynamics studies, with potentials being separately derived from the positive and negative ion measurements. These two potentials were found to not be in agreement with each other, although individually the results were in agreement with previous spacecraft potential studies (Crary et al., 2009; Westlake et al., 2014; Desai et al., 2017).

7.2 Further Work

The projects completed in this thesis led to several research ideas that were not completed during the PhD timeframe. Here I describe possible projects as a guide for future research in the field.

7.2.1 CAPS heavy ion energy-angle response

One part of the analysis that was explored in Chapters 5 and 6 was the energy-angle response of CAPS sensors. Future studies should fully incorporate an energy-angle response for analysis of ELS and IBS data. It would be extremely beneficial to perform simulations of the response using known descriptions of the sensors. This could be performed using ion optics simulation software such as SIMION. Furthermore, this could also be combined with new lab studies of the instrument flight spares to analyse their response, particularly their response to the heavy ions measured in Titan's ionosphere. This would be particularly pertinent for the ELS sensor, as it was never intended to measure negative ions, so its performance is largely unknown. Initial work on this has been done by Nicolaou et al. (2022) but there is scope for further work.

7.2.2 3D velocity determination

Using the capabilities of CAPS IBS and ELS, 3D ion velocity measurements could be derived within Titan's ionosphere.

CAPS IBS was designed to obtain high-angular resolution 3D velocity space measurements (Young et al., 2004). However, this may present difficulties as one of the sensor fans has been observed to display a different angular response to the other two (Crary et al., 2009). If this could be overcome, a 3D velocity vector could be created using the crossed-fan geometry of the IBS sensor. This would

involve measuring the time difference of when an ion beam was observed by the three separate IBS fans.

The multiple anodes of ELS gives resolution capability in another axis, along the elevation direction. This would be in addition to using the actuation and the ion energies. Utilising all three axes would theoretically allow for the construction of a 3D negative ion velocity vector.

By using the 3D velocity vectors for both the positive and negative ions, magnitude and direction of ion movements in Titan's ionosphere can be found, further illuminating topics such as the presence of electric fields.

7.2.3 Cassini spacecraft charging model in Titan's ionosphere

As Chapters 5 and 6 illustrated, several difficulties remain in the interpretation of CAPS data inside Titan's ionosphere. For better understanding of spacecraft charging and ion velocities, modelling the Cassini spacecraft under Titan conditions would be beneficial. This would require a complex model that has both self-consistent electric and magnetic field modelling in tandem with multiple species of both positive and negative ions in addition to electrons. Through this, there would be improved understanding on any possible differential charging Cassini may experience and how the local plasma environment affects CAPS measurements. This model could also utilise particle tracking for understanding discrepancies in the ion velocities for positive and negative ions. Some work has been completed on this by Zhang et al. (2021) for Cassini in Saturn's ionosphere and Holmberg et al. (2021) for Saturn's inner magnetosphere but so far this has not been attempted in Titan's ionosphere.

7.2.4 Future mission & campaigns

In the future, new missions and campaigns will aid interpretation of Cassini data. These include recent advances in remote sensing such as the ground based Atacama Large Millimeter/submillimeter Array (ALMA) telescope and the space based James Webb Space Telescope (JWST). In addition, several spacecraft are planned to visit moons of Jupiter and Saturn which will benefit from Cassini insights and

will also provide further context for Cassini findings.

7.2.4.1 Remote Sensing: ALMA & JWST

Data obtained from future Titan campaigns using ALMA could be combined with observations from Cassini instruments. Early ALMA Titan studies mostly included compositional and distribution studies of molecules (Cordiner et al., 2014, 2015). There was previous overlap between Cassini and ALMA, highlighted by Cordiner et al. (2019), who investigated atmospheric composition using both ALMA and infrared data obtained by Cassini. Other results such as Lellouch et al. (2019); Cordiner et al. (2020) have already increased understanding of Titan’s winds but further extension of this work would investigate long term seasonal trends, such as the change in the pole-to-pole circulation of the atmosphere. Furthermore, most of the work currently being performed compares infrared ALMA data to infrared data from Cassini, but there is much potential for combining ALMA data with other Cassini datasets, particularly in compositional studies.

JWST launched on 25th December 2021 and began science operations on the 12th July 2022. Widely seen as a successor to the Hubble Space Telescope (HST), JWST has a large potential contribution to Titan science, with a spatial resolution exceeding HST and a spectral resolution exceeding Cassini at the same wavelengths. Nixon et al. (2016) outlined some of the studies that could be performed including surface studies and studies of tropospheric and stratospheric clouds, hazes and composition. The longevity of JWST will enable long term seasonal studies of Titan to take place, with the possibility of observing the same seasons Cassini observed later in the mission.

7.2.4.2 Jovian Orbiters: Europa Clipper & JUICE

Two missions are launching in the near future to study the Jovian moons, the NASA-led Europa Clipper, currently planned for launch in 2024, and the ESA-led Jupiter Icy Moons Explorer (JUICE), planned for launch in 2023. Europa Clipper will make 44 flybys of the icy moon Europa, whilst JUICE will make flybys of Ganymede, Callisto and Europa before entering into orbit around Ganymede. The knowledge gained from these missions will have transferable knowledge to Cassini data. In

particular, the study of Europa, which is believed to have a water plume similar to Enceladus, will allow comparative studies to be performed between the two moons thus gaining insight into plume mechanics.

7.2.4.3 Saturnian spacecraft: Dragonfly

Looking further ahead than the Jovian missions, future missions that return to the Saturn system are planned. Dragonfly is a future NASA mission with a planned launch in 2027. The spacecraft is a large quadcopter that will be sent to study prebiotic chemistry on Titan. It will have a suite of instruments measuring chemical composition, geology and meteorology. Using its findings on the surface, one of its science goals is that a connection can be made between the complex chemistry found in the atmosphere and the molecules found on the surface. By combining these findings with measurements from Cassini, the full mechanism where small molecules combine into larger molecules which then descend to the surface can be studied.

Appendix A

Studied Titan flybys

A.1 Table A.1

Flyby	Date	UTC	Alt	Lat	Long	SZA	Cross-vel	Along-vel
T16	2006-07-22	00:25	950	85.5	318.7	105.4	(-286, -4)	(-225, -223)
T17	2006-09-07	20:16	1000	22.6	56.9	44.6	(111, 296)	(-285, 94)
T19	2006-10-09	17:23	980	60.9	358.2	81.0	(-90, 73)	(-243, -84)
T21	2006-12-12	11:41	1000	43.5	264.5	125.2	(42, 338)	(-266, -248)
T23	2007-01-13	08:34	1000	30.8	358.2	53.3	(106, 299)	(-251, -119)
T25	2007-02-22	03:11	1000	30.3	16.1	161.3	(-136, 114)	(-120, 15)
T26	2007-03-10	01:49	981	31.6	357.7	149.6	(-21, 196)	(-260, -55)
T27	2007-03-26	00:23	1010	40.8	357.8	144.2	(-295, -61)	(-214, -1)
T28	2007-04-10	22:58	991	50.1	357.8	137.5	(-90, 140)	(-249, -86)
T29	2007-04-26	21:33	981	59.3	358.0	129.9	(-371, -186)	(-277, 65)
T30	2007-05-12	20:10	959	68.5	358.1	121.8	(60, 350)	(-231, 3)
T32	2007-06-13	17:46	965	84.4	358.7	107.1	(-253, -100)	(-319, -65)
T36	2007-10-02	04:43	975	-59.6	108.4	67.5	(-134, 46)	(-145, 117)
T39	2007-12-20	22:58	970	-70.3	175.6	61.4	(-144, 43)	(-251, 148)

Table A.1: Alt, Lat, Lon and SZA are Altitude (in km), Latitude (deg), Longitude (deg) and Solar Zenith Angle (deg) are within 2 minutes of closest approach, values are from the Atmospheres Node of NASA PDS. The "Cross-vel" column contains pairs of (positive ion crosstrack velocity, negative ion crosstrack velocity) in m/s as measured nearest to closest approach, the sign indicates the direction of the velocity. "Along-vel" is similar to "Cross-vel" but for alongtrack velocities, with positively signed values indicating headwinds in the Cassini frame.

A.2 Table A.2

Flyby	Date	UTC	Alt	Lat	Long	SZA	Cross-vel	Along-vel
T40	2008-01-05	21:30	1010	-11.5	130.3	37.6	(-67, 107)	(-155, 150)
T41	2008-02-22	17:32	1000	-34.9	151.4	30.3	(-423, -229)	(-179, 85)
T42	2008-03-25	14:28	1000	-27.2	156.2	21.4	(1, 225)	(-128, 84)
T43	2008-05-12	10:02	1000	18.0	137.2	35.9	(-148, 61)	(14, 93)
T48	2008-12-05	14:26	960	-10.5	178.6	25.0	(-440, -189)	(-24, 260)
T49	2008-12-21	13:00	970	-44.2	236.7	82.5	(-511, -392)	(-82, -41)
T50	2009-02-07	08:51	967	-33.9	306.4	136.1	(-222, -181)	(-188, 211)
T51	2009-03-27	04:43	960	-30.6	234.8	84.1	(-72, 151)	(-107, 125)
T55	2009-05-21	21:27	965	-21.8	177.8	141.6		(2, 92)
T56	2009-06-06	20:00	965	-31.9	178.1	135.1		(7, -160)
T57	2009-06-22	18:33	955	-41.9	178.3	128.0		(-4, -120)
T58	2009-07-08	17:04	965	-52.1	178.8	120.2		(-63, -196)
T59	2009-07-24	15:31	955	-62.0	179.5	112.2		(-115, -146)
T71	2010-07-07	00:26	1004	-56.5	303.4	82.3	(-77, 126)	(-219, -295)
T83	2012-05-22	01:10	954	72.7	127.5	71.2	(-149, -7)	(-143, -36)

Table A.2: For column descriptions see previous table. Flybys T55 through T59 do not have cross-track velocity measurements and the along-track velocities are an average of 40 seconds around closest approach.

Appendix B

Acronyms

<i>CAPS</i>	Cassini Plasma Spectrometer
<i>DEF</i>	Differential Energy Flux
<i>ELS</i>	Electron Spectrometer
<i>ESA</i>	European Space Agency
<i>FOV</i>	Field Of View
<i>IBS</i>	Ion Beam Spectrometer
<i>IMS</i>	Ion Mass Spectrometer
<i>INMS</i>	Ion and Neutral Mass Spectrometer
<i>LP</i>	Langmuir Probe
<i>MCP</i>	Microchannel Plate
<i>MHD</i>	Magnetohydrodynamics
<i>NAIF</i>	Navigation and Ancillary Information Facility
<i>NASA</i>	National Aeronautics and Space Administration
<i>PSD</i>	Phase Space Density
<i>RPWS</i>	Radio and Plasma Wave Science
<i>SPICE</i>	Spacecraft Planet Instrument C-matrix Events

Bibliography

- A. Ali, E. Sittler, D. Chornay, B. Rowe, and C. Puzzarini. Organic chemistry in titan’s upper atmosphere and its astrobiological consequences: I. views towards cassini plasma spectrometer (caps) and ion neutral mass spectrometer (inms) experiments in space. *Planetary and Space Science*, 109-110: 46 – 63, 2015. ISSN 0032-0633. doi: <https://doi.org/10.1016/j.pss.2015.01.015>. URL <http://www.sciencedirect.com/science/article/pii/S0032063315000161>.
- P. Banks and G. Kockarts. Aeronomy, vol. a. *vol., B*, pages 101–122, 1973.
- W. Baumjohann and R. Treumann. *Basic space plasma physics*. 1996. doi: 10.1142/p015.
- J. L. Berry, M. S. Ugelow, M. A. Tolbert, and E. C. Browne. The influence of gas-phase chemistry on organic haze formation. *The Astrophysical Journal*, 885(1): L6, oct 2019. doi: 10.3847/2041-8213/ab4b5b. URL <https://doi.org/10.3847/2041-8213/ab4b5b>.
- C. Bertucci. Induced Magnetospheres. In *Magnetospheres in the Solar System*, pages 407–425. American Geophysical Union (AGU), 2021. ISBN 978-1-119-81562-4. doi: 10.1002/9781119815624.ch26. URL <https://agupubs.onlinelibrary.wiley.com/doi/abs/10.1002/9781119815624.ch26>. Section: 26 _eprint: <https://agupubs.onlinelibrary.wiley.com/doi/pdf/10.1002/9781119815624.ch26>.
- C. Bertucci, F. M. Neubauer, K. Szego, J. E. Wahlund, A. J. Coates, M. K.

- Dougherty, D. T. Young, and W. S. Kurth. Structure of Titan's mid-range magnetic tail: Cassini magnetometer observations during the T9 flyby. *Geophysical Research Letters*, 34(24):L24S02, Nov. 2007. doi: 10.1029/2007GL030865.
- M. Cable, S. Hörst, C. He, A. Stockton, M. Mora, M. Tolbert, M. Smith, and P. Willis. Identification of primary amines in titan tholins using microchip non-aqueous capillary electrophoresis. *Earth and Planetary Science Letters*, 403: 99 – 107, 2014. ISSN 0012-821X. doi: <https://doi.org/10.1016/j.epsl.2014.06.028>. URL <http://www.sciencedirect.com/science/article/pii/S0012821X14004130>.
- C. Chen and S. Simon. A comprehensive study of Titan's magnetic pile-up region during the Cassini era. *Planetary and Space Science*, 191:105037, Oct. 2020. doi: 10.1016/j.pss.2020.105037.
- A. Christodoulides, D. McCorkle, and L. Christopoulu. Electron affinities of atoms molecules and radicals. *Electron-Molecule Interactions and Their Applications*, 2:423–641, 1984.
- A. Coates, F. Crary, G. Lewis, D. Young, J. Waite Jr., and E. Sittler Jr. Discovery of heavy negative ions in Titan's ionosphere. *Geophysical Research Letters*, 34(22), 2007. doi: 10.1029/2007GL030978. URL <https://agupubs.onlinelibrary.wiley.com/doi/abs/10.1029/2007GL030978>.
- A. Coates, A. Wellbrock, G. Lewis, G. Jones, D. Young, F. Crary, and J. Waite. Heavy negative ions in titan's ionosphere: Altitude and latitude dependence. *Planetary and Space Science*, 57(14):1866 – 1871, 2009. ISSN 0032-0633. doi: <https://doi.org/10.1016/j.pss.2009.05.009>. URL <http://www.sciencedirect.com/science/article/pii/S0032063309001548>.
- A. Coates, G. Jones, G. Lewis, A. A. Wellbrock, D. Young, F. Crary, R. Johnson, T. Cassidy, and T. Hill. Negative ions in the Enceladus plume. *Icarus*, 206(2):618 – 622, 2010a. ISSN 0019-1035. doi: <https://doi.org/10.1016/j.icarus.2009.07.015>.

013. URL <http://www.sciencedirect.com/science/article/pii/S0019103509003030>. Cassini at Saturn.
- A. Coates, A. Wellbrock, G. Lewis, G. Jones, D. Young, F. Crary, J. Waite, R. Johnson, T. Hill, and E. Sittler Jr. Negative ions at titan and enceladus: recent results. *Faraday Discuss.*, 147:293–305, 2010b. doi: 10.1039/C004700G. URL <http://dx.doi.org/10.1039/C004700G>.
- A. Coates, A. Wellbrock, G. Jones, J. Waite, P. Schippers, M. Thomsen, C. Arridge, and R. L. Tokar. Photoelectrons in the enceladus plume. *Journal of Geophysical Research: Space Physics*, 118(8):5099–5108, 2013. doi: 10.1002/jgra.50495. URL <https://agupubs.onlinelibrary.wiley.com/doi/abs/10.1002/jgra.50495>.
- A. J. Coates. Interaction of Titan’s ionosphere with Saturn’s magnetosphere. *Philosophical Transactions of the Royal Society of London Series A*, 367(1889):773–788, Feb. 2009. doi: 10.1098/rsta.2008.0248.
- A. J. Coates, J.-E. Wahlund, K. Ågren, N. Edberg, J. Cui, A. Wellbrock, and K. Szego. Recent Results from Titan’s Ionosphere. *Space Science Reviews*, 162(1):85–111, Dec. 2011. ISSN 1572-9672. doi: 10.1007/s11214-011-9826-4. URL <https://doi.org/10.1007/s11214-011-9826-4>.
- M. A. Cordiner, C. A. Nixon, N. A. Teanby, P. G. J. Irwin, J. Serigano, S. B. Charnley, S. N. Milam, M. J. Mumma, D. C. Lis, G. Villanueva, L. Paganini, Y. J. Kuan, and A. J. Remijan. ALMA Measurements of the HNC and HC₃N Distributions in Titan’s Atmosphere. *The Astrophysical Journal Letters*, 795(2):L30, Nov. 2014. doi: 10.1088/2041-8205/795/2/L30.
- M. A. Cordiner, M. Y. Palmer, C. A. Nixon, P. G. J. Irwin, N. A. Teanby, S. B. Charnley, M. J. Mumma, Z. Kisiel, J. Serigano, Y. J. Kuan, Y. L. Chuang, and K. S. Wang. Ethyl Cyanide On Titan: Spectroscopic Detection and Mapping Using Alma. *The Astrophysical Journal Letters*, 800(1):L14, Feb. 2015. doi: 10.1088/2041-8205/800/1/L14.

- M. A. Cordiner, N. A. Teanby, C. A. Nixon, V. Vuitton, A. E. Thelen, and S. B. Charnley. ALMA Spectral Imaging of Titan Contemporaneous with Cassini's Grand Finale. *The Astronomical Journal*, 158(2):76, Aug. 2019. doi: 10.3847/1538-3881/ab2d20.
- M. A. Cordiner, E. Garcia-Berrios, R. G. Cosentino, N. A. Teanby, C. E. Newman, C. A. Nixon, A. E. Thelen, and S. B. Charnley. Detection of Dynamical Instability in Titan's Thermospheric Jet. *The Astrophysical Journal Letters*, 904(1):L12, Nov. 2020. doi: 10.3847/2041-8213/abc688.
- A. Coustenis, R. K. Achterberg, B. J. Conrath, D. E. Jennings, A. Marten, D. Gautier, C. A. Nixon, F. M. Flasar, N. A. Teanby, B. Bézard, R. E. Samuelson, R. C. Carlson, E. Lellouch, G. L. Bjoraker, P. N. Romani, F. W. Taylor, P. G. J. Irwin, T. Fouchet, A. Hubert, G. S. Orton, V. G. Kunde, S. Vinatier, J. Mondellini, M. M. Abbas, and R. Courtin. The composition of Titan's stratosphere from Cassini/CIRS mid-infrared spectra. *Icarus*, 189(1):35–62, July 2007. doi: 10.1016/j.icarus.2006.12.022.
- F. Crary, B. Magee, K. Mandt, J. Waite, J. Westlake, and D. Young. Heavy ions, temperatures and winds in Titan's ionosphere: Combined Cassini CAPS and INMS observations. *Planetary and Space Science*, 57(14):1847 – 1856, 2009. ISSN 0032-0633. doi: <https://doi.org/10.1016/j.pss.2009.09.006>. URL <http://www.sciencedirect.com/science/article/pii/S0032063309002682>.
- T. Cravens, R. McNutt Jr., J. Waite Jr., I. Robertson, J. Luhmann, W. Kasprzak, and W. Ip. Plume ionosphere of Enceladus as seen by the Cassini ion and neutral mass spectrometer. *Geophysical Research Letters*, 36(8), 2009. doi: 10.1029/2009GL037811. URL <https://agupubs.onlinelibrary.wiley.com/doi/abs/10.1029/2009GL037811>.
- T. E. Cravens, I. P. Robertson, J. H. Waite Jr., R. V. Yelle, W. T. Kasprzak, C. N. Keller, S. A. Ledvina, H. B. Niemann, J. G. Luhmann, R. L. McNutt,

- W.-H. Ip, V. De La Haye, I. Mueller-Wodarg, J.-E. Wahlund, V. G. Anicich, and V. Vuitton. Composition of titan's ionosphere. *Geophysical Research Letters*, 33(7), 2006. doi: 10.1029/2005GL025575. URL <https://agupubs.onlinelibrary.wiley.com/doi/abs/10.1029/2005GL025575>.
- T. E. Cravens, M. Richard, Y.-J. Ma, C. Bertucci, J. G. Luhmann, S. Ledvina, I. P. Robertson, J.-E. Wahlund, K. Ågren, J. Cui, I. Müller-Wodarg, J. H. Waite, M. Dougherty, J. Bell, and D. Ulusen. Dynamical and magnetic field time constants for Titan's ionosphere: Empirical estimates and comparisons with Venus. *Journal of Geophysical Research: Space Physics*, 115(A8), 2010. ISSN 2156-2202. doi: 10.1029/2009JA015050. URL <https://agupubs.onlinelibrary.wiley.com/doi/abs/10.1029/2009JA015050>. eprint: <https://agupubs.onlinelibrary.wiley.com/doi/pdf/10.1029/2009JA015050>.
- J. Cui, M. Galand, R. V. Yelle, V. Vuitton, J.-E. Wahlund, P. P. Lavvas, I. C. F. Müller-Wodarg, T. E. Cravens, W. T. Kasprzak, and J. H. Waite Jr. Diurnal variations of titan's ionosphere. *Journal of Geophysical Research: Space Physics*, 114(A6), 2009. doi: 10.1029/2009JA014228. URL <https://agupubs.onlinelibrary.wiley.com/doi/abs/10.1029/2009JA014228>.
- J. Cui, R. V. Yelle, V. Vuitton, J. H. Waite, W. T. Kasprzak, D. A. Gell, H. B. Niemann, I. C. F. Müller-Wodarg, N. Borggren, G. G. Fletcher, E. L. Patrick, E. Raaen, and B. A. Magee. Analysis of Titan's neutral upper atmosphere from Cassini Ion Neutral Mass Spectrometer measurements. *Icarus*, 200(2):581–615, Apr. 2009. doi: 10.1016/j.icarus.2008.12.005.
- R. Dabestani and I. N. Ivanov. A compilation of physical, spectroscopic and photochemical properties of polycyclic aromatic hydrocarbons. *Photochemistry and Photobiology*, 70(1):10–34, 1999. doi: 10.1111/j.1751-1097.1999.tb01945.x. URL <https://onlinelibrary.wiley.com/doi/abs/10.1111/j.1751-1097.1999.tb01945.x>.

- R. T. Desai, A. J. Coates, A. Wellbrock, V. Vuitton, F. J. Crary, D. González-Caniulef, O. Shebanits, G. H. Jones, G. R. Lewis, J. H. Waite, M. Cordiner, S. A. Taylor, D. O. Kataria, J. E. Wahlund, N. J. T. Edberg, and E. C. Sittler. Carbon Chain Anions and the Growth of Complex Organic Molecules in Titan’s Ionosphere. *The Astrophysical Journal Letters*, 844(2):L18, Aug. 2017. doi: 10.3847/2041-8213/aa7851.
- Y. Dong, T. W. Hill, B. D. Teolis, B. A. Magee, and J. H. Waite. The water vapor plumes of Enceladus. *Journal of Geophysical Research (Space Physics)*, 116 (A10):A10204, Oct 2011. doi: 10.1029/2011JA016693.
- M. Dougherty, K. Khurana, F. Neubauer, C. Russell, J. Saur, J. Leisner, and M. Burton. Identification of a dynamic atmosphere at enceladus with the cassini magnetometer. *Science*, 311(5766):1406–1409, 2006. ISSN 0036-8075. doi: 10.1126/science.1120985. URL <https://science.sciencemag.org/content/311/5766/1406>.
- D. Dubois, N. Carrasco, L. Jovanovic, L. Vettier, T. Gautier, and J. Westlake. Positive ion chemistry in an n2-ch4 plasma discharge: Key precursors to the growth of titan tholins. *Icarus*, 338:113437, 2020. ISSN 0019-1035. doi: <https://doi.org/10.1016/j.icarus.2019.113437>. URL <http://www.sciencedirect.com/science/article/pii/S0019103518306316>.
- N. J. T. Edberg, K. Ågren, J. E. Wahlund, M. W. Morooka, D. J. Andrews, S. W. H. Cowley, A. Wellbrock, A. J. Coates, C. Bertucci, and M. K. Dougherty. Structured ionospheric outflow during the Cassini T55-T59 Titan flybys. *Planetary and Space Science*, 59(8):788–797, June 2011. doi: 10.1016/j.pss.2011.03.007.
- W. M. Farrell, W. S. Kurth, R. L. Tokar, J. E. Wahlund, D. A. Gurnett, Z. Wang, R. J. MacDowall, M. W. Morooka, R. E. Johnson, and J. H. Waite. Modification of the plasma in the near-vicinity of Enceladus by the enveloping dust. *Geophysical Research Letters*, 37(20):L20202, Oct 2010. doi: 10.1029/2010GL044768.

- B. G. Fejer. Low Latitude Ionospheric Electrodynamics. *Space Science Reviews*, 158(1):145–166, Jan. 2011. doi: 10.1007/s11214-010-9690-7.
- B. L. Fleshman, P. A. Delamere, and F. Bagenal. Modeling the Enceladus plume-plasma interaction. *Geophysical Research Letters*, 37:L03202, Feb. 2010. doi: 10.1029/2009GL041613.
- B. Fleury, N. Carrasco, T. Gautier, A. Mahjoub, J. He, C. Szopa, E. Hadamcik, A. Buch, and G. Cernogora. Influence of CO on Titan atmospheric reactivity. *Icarus*, 238:221–229, Aug. 2014. doi: 10.1016/j.icarus.2014.05.027.
- T. Gautier, J. A. Sebree, X. Li, V. T. Pinnick, A. Grubisic, M. J. Loeffler, S. A. Getty, M. G. Trainer, and W. B. Brinckerhoff. Influence of trace aromatics on the chemical growth mechanisms of Titan aerosol analogues. *Planetary and Space Science*, 140:27–34, June 2017. doi: 10.1016/j.pss.2017.03.012.
- D. A. Gurnett, W. S. Kurth, D. L. Kirchner, G. B. Hospodarsky, T. F. Averkamp, P. Zarka, A. Lecacheux, R. Manning, A. Roux, P. Canu, N. Cornilleau-Wehrlin, P. Galopeau, A. Meyer, R. Boström, G. Gustafsson, J. E. Wahlund, L. Åhlen, H. O. Rucker, H. P. Ladreiter, W. Macher, L. J. C. Woolliscroft, H. Alleyne, M. L. Kaiser, M. D. Desch, W. M. Farrell, C. C. Harvey, P. Louarn, P. J. Kellogg, K. Goetz, and A. Pedersen. The Cassini Radio and Plasma Wave Investigation. *Space Science Reviews*, 114(1-4):395–463, Sept. 2004. doi: 10.1007/s11214-004-1434-0.
- C. J. Hansen, L. Esposito, A. I. F. Stewart, J. Colwell, A. Hendrix, W. Pryor, D. Shemansky, and R. West. Enceladus’ water vapor plume. *Science*, 311 (5766):1422–1425, 2006. ISSN 0036-8075. doi: 10.1126/science.1121254. URL <https://science.sciencemag.org/content/311/5766/1422>.
- C. J. Hansen, L. W. Esposito, A. I. F. Stewart, B. Meinke, B. Wallis, J. E. Colwell, A. R. Hendrix, K. Larsen, W. Pryor, and F. Tian. Water vapour jets inside the plume of gas leaving Enceladus. *Nature*, 456(7221):477–479, Nov 2008. doi: 10.1038/nature07542.

- C. J. Hansen, D. E. Shemansky, L. W. Esposito, A. I. F. Stewart, B. R. Lewis, J. E. Colwell, A. R. Hendrix, R. A. West, J. Waite, J. H., and B. Teolis. The composition and structure of the Enceladus plume. *Geophysical Research Letters*, 38(11):L11202, Jun 2011. doi: 10.1029/2011GL047415.
- R. E. Hartle, E. C. Sittler, F. M. Neubauer, R. E. Johnson, H. T. Smith, F. Crary, D. J. McComas, D. T. Young, A. J. Coates, D. Simpson, S. Bolton, D. Reisenfeld, K. Szego, J. J. Berthelier, A. Rymer, J. Vilppola, J. T. Steinberg, and N. Andre. Preliminary interpretation of Titan plasma interaction as observed by the Cassini Plasma Spectrometer: Comparisons with Voyager 1. *Geophysical Research Letters*, 33(8):L08201, Apr. 2006. doi: 10.1029/2005GL024817.
- R. P. Haythornthwaite, A. J. Coates, G. H. Jones, and J. H. Waite. Fast and Slow Water Ion Populations in the Enceladus Plume. *Journal of Geophysical Research (Space Physics)*, 125(2):e27591, Feb. 2020. doi: 10.1029/2019JA027591.
- R. P. Haythornthwaite, A. J. Coates, G. H. Jones, A. Wellbrock, J. H. Waite, V. Vuitton, and P. Lavvas. Heavy Positive Ion Groups in Titan's Ionosphere from Cassini Plasma Spectrometer IBS Observations. *The Planetary Science Journal*, 2(1):26, Feb. 2021. doi: 10.3847/PSJ/abd404.
- M. M. Hedman, D. Dhingra, P. D. Nicholson, C. J. Hansen, G. Portyankina, S. Ye, and Y. Dong. Spatial variations in the dust-to-gas ratio of Enceladus' plume. *Icarus*, 305:123–138, May 2018. doi: 10.1016/j.icarus.2018.01.006.
- T. W. Hill, M. F. Thomsen, R. L. Tokar, A. J. Coates, G. R. Lewis, D. T. Young, F. J. Crary, R. A. Baragiola, R. E. Johnson, Y. Dong, R. J. Wilson, G. H. Jones, J.-E. Wahlund, D. G. Mitchell, and M. Horányi. Charged nanograins in the enceladus plume. *Journal of Geophysical Research: Space Physics*, 117(A5), 2012. doi: 10.1029/2011JA017218. URL <https://agupubs.onlinelibrary.wiley.com/doi/abs/10.1029/2011JA017218>.
- M. K. G. Holmberg, F. Cipriani, T. Nilsson, S. Hess, H. L. F. Huybrighs, L. Z. Hadid, G. Déprez, R. J. Wilson, M. W. Morooka, and M. Felici. Cassini-

- Plasma Interaction Simulations Revealing the Cassini Ion Wake Characteristics: Implications for In-Situ Data Analyses and Ion Temperature Estimates. *Journal of Geophysical Research (Space Physics)*, 126(8):e29026, Aug. 2021. doi: 10.1029/2020JA029026.
- S. M. Horst. Titan's atmosphere and climate. *Journal of Geophysical Research: Planets*, 122(3):432–482, 2017. doi: <https://doi.org/10.1002/2016JE005240>. URL <https://agupubs.onlinelibrary.wiley.com/doi/abs/10.1002/2016JE005240>.
- S. M. Hörst, R. V. Yelle, A. Buch, N. Carrasco, G. Cernogora, O. Dutuit, E. Quirico, E. Sciamma-O'Brien, M. A. Smith, Á. Somogyi, C. Szopa, R. Thissen, and V. Vuitton. Formation of Amino Acids and Nucleotide Bases in a Titan Atmosphere Simulation Experiment. *Astrobiology*, 12(9):809–817, Sept. 2012. doi: 10.1089/ast.2011.0623.
- G. Jones, C. Arridge, A. Coates, G. Lewis, S. Kanani, A. Wellbrock, D. Young, F. Crary, R. Tokar, R. Wilson, T. Hill, R. Johnson, D. Mitchell, J. Schmidt, S. Kempf, U. Beckmann, C. Russell, Y. Jia, M. Dougherty, J. Waite Jr., and B. Magee. Fine jet structure of electrically charged grains in Enceladus' plume. *Geophysical Research Letters*, 36(16), 2009. doi: 10.1029/2009GL038284. URL <https://agupubs.onlinelibrary.wiley.com/doi/abs/10.1029/2009GL038284>.
- G. Jones, A. Coates, and A. Wellbrock. Negative ion flow at Titan. In *AGU Fall Meeting Abstracts*, volume 2011, pages SA13A–1887, Dec 2011.
- M. Kelley. *The Earth's Ionosphere: Plasma Physics and Electrodynamics*. ISSN. Elsevier Science, 2009. ISBN 9780080916576. URL <https://books.google.co.uk/books?id=3G1WQnjBQNgC>.
- A. Kivelson, M. Kivelson, and C. Russell. *Introduction to Space Physics*. Cambridge atmospheric and space science series. Cambridge University Press, 1995.

ISBN 9780521457149. URL <https://books.google.co.uk/books?id=qWHSqXGfsfQC>.

- T. Kostiuk, K. E. Fast, T. A. Livengood, T. Hewagama, J. J. Goldstein, F. Espenak, and D. Buhl. Direct measurement of winds on Titan. *Geophysical Research Letters*, 28(12):2361–2364, June 2001. doi: 10.1029/2000GL012617.
- H. Kriegel, S. Simon, U. Motschmann, J. Saur, F. M. Neubauer, A. M. Persoon, M. K. Dougherty, and D. A. Gurnett. Influence of negatively charged plume grains on the structure of Enceladus’ Alfvén wings: Hybrid simulations versus Cassini Magnetometer data. *Journal of Geophysical Research (Space Physics)*, 116(A10):A10223, Oct 2011. doi: 10.1029/2011JA016842.
- P. Lavvas, M. Sander, M. Kraft, and H. Imanaka. Surface Chemistry and Particle Shape: Processes for the Evolution of Aerosols in Titan’s Atmosphere. *The Astrophysical Journal*, 728(2):80, Feb. 2011. doi: 10.1088/0004-637X/728/2/80.
- P. Lavvas, R. V. Yelle, T. Koskinen, A. Bazin, V. Vuitton, E. Vigren, M. Galand , A. Wellbrock, A. J. Coates, J.-E. Wahlund, F. J. Crary, and D. Snowden. Aerosol growth in Titan’s ionosphere. *Proceedings of the National Academy of Science*, 110(8):2729–2734, Feb. 2013. doi: 10.1073/pnas.1217059110.
- P. P. Lavvas, A. Coustenis, and I. M. Vardavas. Coupling photochemistry with haze formation in Titan’s atmosphere, Part I: Model description. *Planetary and Space Science*, 56(1):27–66, Jan. 2008a. doi: 10.1016/j.pss.2007.05.026.
- P. P. Lavvas, A. Coustenis, and I. M. Vardavas. Coupling photochemistry with haze formation in Titan’s atmosphere, Part II: Results and validation with Cassini/Huygens data. *Planetary and Space Science*, 56(1):67–99, Jan. 2008b. doi: 10.1016/j.pss.2007.05.027.
- V. Le Page, Y. Keheyian, T. P. Snow, and V. M. Bierbaum. Gas phase chemistry of pyrene and related cations with molecules and atoms of interstellar interest. *International Journal of Mass Spectrometry*, 185:949–959, Apr. 1999. doi: 10.1016/S1387-3806(98)14217-3.

- V. Le Page, Y. Keheyian, T. P. Snow, and V. M. Bierbaum. Gas phase chemistry of pyrene and related cations with molecules and atoms of interstellar interest. *International Journal of Mass Spectrometry*, 185:949–959, Apr. 1999b. doi: 10.1016/S1387-3806(98)14217-3.
- S. Lebonnois, E. Bakes, and C. P. McKay. Transition from gaseous compounds to aerosols in titan’s atmosphere. *Icarus*, 159(2):505 – 517, 2002. ISSN 0019-1035. doi: <https://doi.org/10.1006/icar.2002.6943>. URL <http://www.sciencedirect.com/science/article/pii/S0019103502969435>.
- S. A. Ledvina, S. H. Brecht, and T. E. Cravens. The orientation of Titan’s day-side ionosphere and its effects on Titan’s plasma interaction. *Earth, Planets and Space*, 64(2):207–230, Feb. 2012. doi: 10.5047/eps.2011.08.009.
- E. Lellouch, M. A. Gurwell, R. Moreno, S. Vinatier, D. F. Strobel, A. Moullet, B. Butler, L. Lara, T. Hidayat, and E. Villard. An intense thermospheric jet on Titan. *Nature Astronomy*, 3:614–619, Apr. 2019. doi: 10.1038/s41550-019-0749-4.
- G. Lewis, N. André, C. Arridge, A. Coates, L. Gilbert, D. Linder, and A. Rymer. Derivation of density and temperature from the cassini–huygens caps electron spectrometer. *Planetary and Space Science*, 56(7):901 – 912, 2008. ISSN 0032-0633. doi: <https://doi.org/10.1016/j.pss.2007.12.017>. URL <http://www.sciencedirect.com/science/article/pii/S0032063307003959>.
- G. F. Lindal, G. E. Wood, H. B. Hotz, D. N. Sweetnam, V. R. Eshleman, and G. L. Tyler. The atmosphere of Titan: An analysis of the Voyager 1 radio occultation measurements. *Icarus*, 53(2):348–363, Feb. 1983. doi: 10.1016/0019-1035(83)90155-0.
- D. R. Linder, A. J. Coates, R. D. Woodliffe, C. Alsop, A. D. Johnstone, M. Grande, A. Preece, B. Narheim, and D. T. Young. The Cassini CAPS Electron Spec-

- trometer. *Geophysical Monograph Series*, 102:257, Jan. 1998. doi: 10.1029/GM102p0257.
- L. Lomidze, J. K. Burchill, D. J. Knudsen, A. Kouznetsov, and D. R. Weimer. Validity study of the swarm horizontal cross-track ion drift velocities in the high-latitude ionosphere. *Earth and Space Science*, 6(3):411–432, 2019. doi: <https://doi.org/10.1029/2018EA000546>. URL <https://agupubs.onlinelibrary.wiley.com/doi/abs/10.1029/2018EA000546>.
- M. López-Puertas, B. M. Dinelli, A. Adriani, B. Funke, M. García-Comas, M. L. Moriconi, E. D’Aversa, C. Boersma, and L. J. Allamandola. Large Abundances of Polycyclic Aromatic Hydrocarbons in Titan’s Upper Atmosphere. *The Astrophysical Journal*, 770(2):132, June 2013. doi: 10.1088/0004-637X/770/2/132.
- B. Magee and J. Waite. Neutral Gas Composition of Enceladus’ Plume - Model Parameter Insights from Cassini-INMS. In *Lunar and Planetary Science Conference*, page 2974, Mar 2017.
- A. Mahjoub, M. Schwell, N. Carrasco, Y. Benilan, G. Cernogora, C. Szopa, and M.-C. Gazeau. Characterization of aromaticity in analogues of titan’s atmospheric aerosols with two-step laser desorption ionization mass spectrometry. *Planetary and Space Science*, 131:1–13, Oct. 2016. doi: 10.1016/j.pss.2016.05.003.
- K. E. Mandt, D. A. Gell, M. Perry, J. Hunter Waite Jr., F. A. Crary, D. Young, B. A. Magee, J. H. Westlake, T. Cravens, W. Kasprzak, G. Miller, J.-E. Wahlund, K. Ågren, N. J. T. Edberg, A. N. Heays, B. R. Lewis, S. T. Gibson, V. de la Haye, and M.-C. Liang. Ion densities and composition of titan’s upper atmosphere derived from the cassini ion neutral mass spectrometer: Analysis methods and comparison of measured ion densities to photochemical model simulations. *Journal of Geophysical Research: Planets*, 117(E10), 2012. doi: 10.1029/2012JE004139. URL <https://agupubs.onlinelibrary.wiley.com/doi/abs/10.1029/2012JE004139>.
- T. Mihailescu, R. T. Desai, O. Shebanits, R. Haythornthwaite, A. Wellbrock, A. J.

- Coates, J. P. Eastwood, and J. H. Waite. Spatial Variations of Low-mass Negative Ions in Titan’s Upper Atmosphere. *The Planetary Science Journal*, 1(2):50, Sept. 2020. doi: 10.3847/PSJ/abb1ba.
- T. J. Millar, C. Walsh, and T. A. Field. Negative Ions in Space. *Chemical Reviews*, 117(3):1765–1795, Feb. 2017. ISSN 0009-2665. doi: 10.1021/acs.chemrev.6b00480. URL <https://doi.org/10.1021/acs.chemrev.6b00480>. Publisher: American Chemical Society.
- R. Moreno, A. Marten, and T. Hidayat. Interferometric measurements of zonal winds on Titan. *Astronomy & Astrophysics*, 437(1):319–328, July 2005. doi: 10.1051/0004-6361:20042117.
- I. C. F. Müller-Wodarg, R. V. Yelle, N. Borggren, and J. H. Waite Jr. Waves and horizontal structures in titan’s thermosphere. *Journal of Geophysical Research: Space Physics*, 111(A12), 2006. doi: <https://doi.org/10.1029/2006JA011961>. URL <https://agupubs.onlinelibrary.wiley.com/doi/abs/10.1029/2006JA011961>.
- I. C. F. Müller-Wodarg, R. V. Yelle, J. Cui, and J. H. Waite. Horizontal structures and dynamics of titan’s thermosphere. *Journal of Geophysical Research: Planets*, 113(E10), 2008. doi: <https://doi.org/10.1029/2007JE003033>. URL <https://agupubs.onlinelibrary.wiley.com/doi/abs/10.1029/2007JE003033>.
- G. Nicolaou, R. P. Haythornthwaite, and A. J. Coates. Resolving Space Plasma Species With Electrostatic Analyzers. *Frontiers in Astronomy and Space Sciences*, 9:861433, June 2022. doi: 10.3389/fspas.2022.861433.
- C. A. Nixon, R. K. Achterberg, M. Ádámkovics, B. Bézard, G. L. Bjoraker, T. Cornet, A. G. Hayes, E. Lellouch, M. T. Lemmon, M. López-Puertas, S. Rodriguez, C. Sotin, N. A. Teanby, E. P. Turtle, and R. A. West. Titan Science with the James Webb Space Telescope. *Publications of the Astronomical Society of the Pacific*, 128(959):018007, Jan. 2016. doi: 10.1088/1538-3873/128/959/018007.

- N. Omidi, R. L. Tokar, T. Averkamp, D. A. Gurnett, W. S. Kurth, and Z. Wang. Flow stagnation at enceladus: The effects of neutral gas and charged dust. *Journal of Geophysical Research: Space Physics*, 117(A6), 2012. doi: 10.1029/2011JA017488. URL <https://agupubs.onlinelibrary.wiley.com/doi/abs/10.1029/2011JA017488>.
- M. Perry, B. Teolis, D. Hurley, B. Magee, J. Waite, T. Brockwell, R. Perryman, and R. McNutt. Cassini INMS measurements of Enceladus plume density. *Icarus*, 257:139 – 162, 2015. ISSN 0019-1035. doi: <https://doi.org/10.1016/j.icarus.2015.04.037>. URL <http://www.sciencedirect.com/science/article/pii/S0019103515001803>.
- C. Porco, D. DiNino, and F. Nimmo. How the Geysers, Tidal Stresses, and Thermal Emission across the South Polar Terrain of Enceladus are Related. *The Astronomical Journal*, 148(3):45, Sep 2014. doi: 10.1088/0004-6256/148/3/45.
- C. C. Porco, E. Baker, J. Barbara, K. Beurle, A. Brahic, J. A. Burns, S. Charnoz, N. Cooper, D. D. Dawson, A. D. Del Genio, T. Denk, L. Dones, U. Dyudina, M. W. Evans, S. Fussner, B. Giese, K. Grazier, P. Helfenstein, A. P. Ingersoll, R. A. Jacobson, T. V. Johnson, A. McEwen, C. D. Murray, G. Neukum, W. M. Owen, J. Perry, T. Roatsch, J. Spitale, S. Squyres, P. Thomas, M. Tiscareno, E. P. Turtle, A. R. Vasavada, J. Veverka, R. Wagner, and R. West. Imaging of Titan from the Cassini spacecraft. *Nature*, 434(7030):159–168, Mar. 2005. doi: 10.1038/nature03436.
- F. Postberg, J. Schmidt, J. Hillier, S. Kempf, and R. Srama. A salt-water reservoir as the source of a compositionally stratified plume on enceladus. *Nature*, 474: 620 EP –, Jun 2011. URL <https://doi.org/10.1038/nature10175>.
- F. Postberg, R. N. Clark, C. J. Hansen, A. J. Coates, C. M. Dalle Ore, F. Scipioni, M. M. Hedman, and J. H. Waite. *Plume and Surface Composition of Enceladus*, page 129. 2018b. doi: 10.2458/azu_uapress_9780816537075-ch007.
- K. Ågren, D. J. Andrews, S. C. Buchert, A. J. Coates, S. W. H. Cowley, M. K.

- Dougherty, N. J. T. Edberg, P. Garnier, G. R. Lewis, R. Modolo, H. Opgenoorth, G. Provan, L. Rosenqvist, D. L. Talboys, J. E. Wahlund, and A. Wellbrock. Detection of currents and associated electric fields in Titan's ionosphere from Cassini data. *Journal of Geophysical Research (Space Physics)*, 116(A4):A04313, Apr. 2011. doi: 10.1029/2010JA016100.
- K. Ågren, N. J. T. Edberg, and J. E. Wahlund. Detection of negative ions in the deep ionosphere of Titan during the Cassini T70 flyby. *Geophysical Research Letters*, 39(10):L10201, May 2012. doi: 10.1029/2012GL051714.
- H. Rishbeth, R. Yelle, and M. Mendillo. Dynamics of titan's thermosphere. *Planetary and Space Science*, 48(1):51–58, 2000. ISSN 0032-0633. doi: [https://doi.org/10.1016/S0032-0633\(99\)00076-8](https://doi.org/10.1016/S0032-0633(99)00076-8). URL <https://www.sciencedirect.com/science/article/pii/S0032063399000768>.
- L. Rosenqvist, J. E. Wahlund, K. Ågren, R. Modolo, H. J. Opgenoorth, D. Strobel, I. Müller-Wodarg, P. Garnier, and C. Bertucci. Titan ionospheric conductivities from Cassini measurements. *Planetary and Space Science*, 57(14-15): 1828–1833, Dec. 2009. doi: 10.1016/j.pss.2009.01.007.
- C. Sagan, B. N. Khare, W. R. Thompson, G. D. McDonald, M. R. Wing, J. L. Bada, T. Vo-Dinh, and E. T. Arakawa. Polycyclic Aromatic Hydrocarbons in the Atmospheres of Titan and Jupiter. *The Astrophysical Journal*, 414:399, Sept. 1993. doi: 10.1086/173086.
- S. Sakai, T. Cravens, N. Omidi, M. Perry, and J. H. Waite. Ion energy distributions and densities in the plume of Enceladus. *Planetary and Space Science*, 130: 60 – 79, 2016. ISSN 0032-0633. doi: <https://doi.org/10.1016/j.pss.2016.05.007>. URL <http://www.sciencedirect.com/science/article/pii/S0032063316301295>. Atmospheres, Magnetospheres and Surfaces of the outer planets, their satellites and ring systems: Part XI.

- L. Sangalli, D. J. Knudsen, M. F. Larsen, T. Zhan, R. F. Pfaff, and D. Rowland. Rocket-based measurements of ion velocity, neutral wind, and electric field in the collisional transition region of the auroral ionosphere. *Journal of Geophysical Research: Space Physics*, 114(A4), 2009. doi: <https://doi.org/10.1029/2008JA013757>. URL <https://agupubs.onlinelibrary.wiley.com/doi/abs/10.1029/2008JA013757>.
- P. Schippers, N. André, R. E. Johnson, M. Blanc, I. Dandouras, A. J. Coates, S. M. Krimigis, and D. T. Young. Identification of photoelectron energy peaks in Saturn's inner neutral torus. *Journal of Geophysical Research (Space Physics)*, 114 (A12):A12212, Dec 2009. doi: 10.1029/2009JA014368.
- E. Sciamma-O'Brien, K. T. Upton, and F. Salama. The Titan Haze Simulation (THS) experiment on COSMIC. Part II. Ex-situ analysis of aerosols produced at low temperature. *Icarus*, 289:214–226, June 2017. doi: 10.1016/j.icarus.2017.02.004.
- O. Shebanits, J. E. Wahlund, J. H. Waite, and M. K. Dougherty. Conductivities of Titan's Dusty Ionosphere. *Journal of Geophysical Research (Space Physics)*, 127 (2):e29910, Feb. 2022. doi: 10.1029/2021JA029910.
- I. Sillanpää and R. E. Johnson. The role of ion-neutral collisions in Titan's magnetospheric interaction. *Planetary and Space Science*, 108:73–86, Apr. 2015. doi: 10.1016/j.pss.2015.01.007.
- E. C. Sittler, J. F. Cooper, S. J. Sturner, and A. Ali. Titan's ionospheric chemistry, fullerenes, oxygen, galactic cosmic rays and the formation of exobiological molecules on and within its surfaces and lakes. *Icarus*, 344: 113246, 2020. ISSN 0019-1035. doi: <https://doi.org/10.1016/j.icarus.2019.03.023>. URL <http://www.sciencedirect.com/science/article/pii/S0019103518302306>. Cassini Mission Science Results.
- D. Skouteris, N. Balucani, N. Faginas-Lago, S. Falcinelli, and M. Rosi. Dimerization of methanimine and its charged species in the atmosphere of Titan and

- interstellar/cometary ice analogs. *Astronomy and Astrophysics*, 584:A76, Dec. 2015. doi: 10.1051/0004-6361/201526978.
- H. Smith, R. Johnson, E. Sittler, M. Shappirio, D. Reisenfeld, O. Tucker, M. Burger, F. Crary, D. McComas, and D. Young. Enceladus: The likely dominant nitrogen source in saturn's magnetosphere. *Icarus*, 188(2):356 – 366, 2007. ISSN 0019-1035. doi: <https://doi.org/10.1016/j.icarus.2006.12.007>. URL <http://www.sciencedirect.com/science/article/pii/S0019103506004556>.
- H. T. Smith, M. Shappirio, R. E. Johnson, D. Reisenfeld, E. C. Sittler, F. J. Crary, D. J. McComas, and D. T. Young. Enceladus: A potential source of ammonia products and molecular nitrogen for saturn's magnetosphere. *Journal of Geophysical Research: Space Physics*, 113(A11), 2008. doi: 10.1029/2008JA013352. URL <https://agupubs.onlinelibrary.wiley.com/doi/abs/10.1029/2008JA013352>.
- H. T. Smith, R. E. Johnson, M. E. Perry, D. G. Mitchell, R. L. McNutt, and D. T. Young. Enceladus plume variability and the neutral gas densities in Saturn's magnetosphere. *Journal of Geophysical Research (Space Physics)*, 115(A10): A10252, Oct 2010. doi: 10.1029/2009JA015184.
- D. Snowden and R. Winglee. Three-dimensional multi-fluid simulations of Titan's interaction with Saturn's magnetosphere: Comparisons with Cassini's T55 flyby. *Journal of Geophysical Research (Space Physics)*, 118(8):4852–4863, Aug. 2013. doi: 10.1002/jgra.50392.
- J. N. Spitale and C. C. Porco. Association of the jets of Enceladus with the warmest regions on its south-polar fractures. *Nature*, 449:695–697, Oct. 2007. doi: 10.1038/nature06217.
- S. Taylor, A. Coates, G. Jones, A. Wellbrock, A. Fazakerley, R. Desai, R. Carretero, M. Michiko, P. Schippers, and J. Waite. Modeling, analysis, and interpretation of photoelectron energy spectra at enceladus observed by

- cassini. *Journal of Geophysical Research: Space Physics*, 123(1):287–296, 2018. doi: 10.1002/2017JA024536. URL <https://agupubs.onlinelibrary.wiley.com/doi/abs/10.1002/2017JA024536>.
- V. Tenishev, M. R. Combi, B. D. Teolis, and J. H. Waite. An approach to numerical simulation of the gas distribution in the atmosphere of Enceladus. *Journal of Geophysical Research (Space Physics)*, 115(A9):A09302, Sep 2010. doi: 10.1029/2009JA015223.
- V. Tenishev, D. C. S. Öztürk, M. R. Combi, M. Rubin, J. H. Waite, and M. Perry. Effect of the Tiger Stripes on the water vapor distribution in Enceladus' exosphere. *Journal of Geophysical Research (Planets)*, 119(12):2658–2667, Dec 2014. doi: 10.1002/2014JE004700.
- B. D. Teolis, M. E. Perry, B. A. Magee, J. Westlake, and J. H. Waite. Detection and measurement of ice grains and gas distribution in the enceladus plume by cassini's ion neutral mass spectrometer. *Journal of Geophysical Research: Space Physics*, 115(A9), 2010. doi: 10.1029/2009JA015192. URL <https://agupubs.onlinelibrary.wiley.com/doi/abs/10.1029/2009JA015192>.
- B. D. Teolis, M. E. Perry, C. J. Hansen, J. H. Waite, C. C. Porco, J. R. Spencer, and C. J. A. Howett. Enceladus Plume Structure and Time Variability: Comparison of Cassini Observations. *Astrobiology*, 17(9):926–940, Sep 2017. doi: 10.1089/ast.2017.1647.
- R. Thissen, O. Witasse, O. Dutuit, C. S. Wedlund, G. Gronoff, and J. Lilensten. Doubly-charged ions in the planetary ionospheres: a review. *Physical Chemistry Chemical Physics (Incorporating Faraday Transactions)*, 13:18264, 2011. doi: 10.1039/C1CP21957J.
- R. Tokar, R. Johnson, M. Thomsen, R. Wilson, D. Young, F. Crary, A. Coates, G. Jones, and C. Paty. Cassini detection of Enceladus' cold water-group plume ionosphere. *Geophysical Research Letters*, 36(13), 2009. doi: 10.1029/

- 2009GL038923. URL <https://agupubs.onlinelibrary.wiley.com/doi/abs/10.1029/2009GL038923>.
- M. G. Trainer, J. A. Sebree, Y. H. Yoon, and M. A. Tolbert. The Influence of Benzene as a Trace Reactant in Titan Aerosol Analogs. *The Astrophysical Journal Letters*, 766(1):L4, Mar. 2013. doi: 10.1088/2041-8205/766/1/L4.
- G. L. Tyler, V. R. Eshleman, J. D. Anderson, G. S. Levy, G. F. Lindal, G. E. Wood, and T. A. Croft. Radio Science Investigations of the Saturn System with Voyager 1: Preliminary Results. *Science*, 212(4491):201–206, Apr. 1981. doi: 10.1126/science.212.4491.201.
- D. Ulusen, J. G. Luhmann, Y. J. Ma, S. Ledvina, T. E. Cravens, K. Mandt, J. H. Waite, and J. E. Wahlund. Investigation of the force balance in the Titan ionosphere: Cassini T5 flyby model/data comparisons. *Icarus*, 210(2):867–880, Dec. 2010. doi: 10.1016/j.icarus.2010.07.004.
- D. Ulusen, J. G. Luhmann, Y. J. Ma, K. E. Mandt, J. H. Waite, M. K. Dougherty, J. E. Wahlund, C. T. Russell, T. E. Cravens, N. J. T. Edberg, and K. Agren. Comparisons of Cassini flybys of the Titan magnetospheric interaction with an MHD model: Evidence for organized behavior at high altitudes. *Icarus*, 217(1):43–54, Jan. 2012. doi: 10.1016/j.icarus.2011.10.009.
- J. H. Vilppola, J. T. Keisala, P. J. Tanskanen, and H. Huomo. Optimization of hemispherical electrostatic analyzer manufacturing with respect to resolution requirements. *Review of Scientific Instruments*, 64(8):2190–2194, Aug. 1993. doi: 10.1063/1.1143958.
- J. H. Vilppola, P. J. Tanskanen, H. Huomo, and B. L. Barraclough. Simulations of the response function of a plasma ion beam spectrometer for the Cassini mission to Saturn. *Review of Scientific Instruments*, 67(4):1494–1501, Apr. 1996. doi: 10.1063/1.1146881.
- J. H. Vilppola, P. J. Tanskanen, B. L. Barraclough, and D. J. McComas. Comparison between simulations and calibrations of a high resolution electrostatic analyzer.

Review of Scientific Instruments, 72(9):3662–3669, Sept. 2001. doi: 10.1063/1.1392337.

V. Vuitton, R. V. Yelle, and V. G. Anicich. The Nitrogen Chemistry of Titan’s Upper Atmosphere Revealed. *The Astrophysical Journal Letters*, 647(2):L175–L178, Aug. 2006. doi: 10.1086/507467.

V. Vuitton, R. Yelle, and M. McEwan. Ion chemistry and n-containing molecules in titan’s upper atmosphere. *Icarus*, 191(2):722 – 742, 2007. ISSN 0019-1035. doi: <https://doi.org/10.1016/j.icarus.2007.06.023>. URL <http://www.sciencedirect.com/science/article/pii/S0019103507002709>.

V. Vuitton, P. Lavvas, R. Yelle, M. Galand, A. Wellbrock, G. Lewis, A. Coates, and J.-E. Wahlgren. Negative ion chemistry in titan’s upper atmosphere. *Planetary and Space Science*, 57(13):1558 – 1572, 2009. ISSN 0032-0633. doi: <https://doi.org/10.1016/j.pss.2009.04.004>. URL <http://www.sciencedirect.com/science/article/pii/S0032063309001068>. Surfaces and Atmospheres of the Outer Planets, Their Satellites and Ring Systems: Part V.

V. Vuitton, R. Yelle, S. Klippenstein, S. Hörst, and P. Lavvas. Simulating the density of organic species in the atmosphere of titan with a coupled ion-neutral photochemical model. *Icarus*, 324:120 – 197, 2019. ISSN 0019-1035. doi: <https://doi.org/10.1016/j.icarus.2018.06.013>. URL <http://www.sciencedirect.com/science/article/pii/S0019103517307522>.

J. Waite, W. Lewis, B. Magee, J. Lunine, W. McKinnon, C. Glein, O. Mousis, D. Young, T. Brockwell, J. Westlake, M.-J. Nguyen, B. Teolis, H. Niemann, R. McNutt, M. Perry, and W.-H. Ip. Liquid water on Enceladus from observations of ammonia and ^{40}Ar in the plume. *Nature*, 460:487–490, Jul 2009. doi: 10.1038/nature08153.

J. Waite, C. Glein, R. Perryman, B. Teolis, B. Magee, G. Miller, J. Grimes, M. Perry, K. Miller, A. Bouquet, J. Lunine, T. Brockwell, and S. Bolton. Cassini

finds molecular hydrogen in the enceladus plume: Evidence for hydrothermal processes. *Science*, 356(6334):155–159, 2017. ISSN 0036-8075. doi: 10.1126/science.aai8703. URL <https://science.sciencemag.org/content/356/6334/155>.

J. Waite, C. Glein, F. Postberg, and J. Lunine. Enceladus as Revealed by the Cassini-Huygens Mission. In *Lunar and Planetary Science Conference*, Lunar and Planetary Science Conference, page 1290, Mar 2019.

J. H. Waite, H. Niemann, R. V. Yelle, W. T. Kasprzak, T. E. Cravens, J. G. Luhmann, R. L. McNutt, W.-H. Ip, D. Gell, V. De La Haye, I. Müller-Wordag, B. Magee, N. Borggren, S. Ledvina, G. Fletcher, E. Walter, R. Miller, S. Scherer, R. Thorpe, J. Xu, B. Block, and K. Arnett. Ion neutral mass spectrometer results from the first flyby of titan. *Science*, 308(5724):982–986, 2005. ISSN 0036-8075. doi: 10.1126/science.1110652. URL <https://science.sciencemag.org/content/308/5724/982>.

J. H. Waite, M. R. Combi, W.-H. Ip, T. E. Cravens, R. L. McNutt, W. Kasprzak, R. Yelle, J. Luhmann, H. Niemann, D. Gell, B. Magee, G. Fletcher, J. Lunine, and W.-L. Tseng. Cassini Ion and Neutral Mass Spectrometer: Enceladus Plume Composition and Structure. *Science*, 311(5766):1419–1422, Mar. 2006. doi: 10.1126/science.1121290.

J. H. Waite, D. T. Young, T. E. Cravens, A. J. Coates, F. J. Crary, B. Magee, and J. Westlake. The process of tholin formation in titan’s upper atmosphere. *Science*, 316(5826):870–875, 2007. ISSN 0036-8075. doi: 10.1126/science.1139727. URL <https://science.sciencemag.org/content/316/5826/870>.

A. Wellbrock, A. J. Coates, G. H. Jones, C. S. Arridge, G. Lewis, B. Magee, J. H. Waite, E. C. Sittler, F. J. Crary, and D. T. Young. Negative ions at Titan - density trends. In *AGU Fall Meeting Abstracts*, volume 2009, pages P51G–1198, Dec. 2009.

- A. Wellbrock, A. J. Coates, G. H. Jones, C. S. Arridge, G. Lewis, E. C. Sittler, and D. T. Young. Density trends of negative ions at Titan. In *AGU Fall Meeting Abstracts*, volume 2012, pages P21F–1898, Dec. 2012.
- A. Wellbrock, A. Coates, G. Jones, G. Lewis, and J. Waite. Cassini caps-els observations of negative ions in titan’s ionosphere: Trends of density with altitude. *Geophysical Research Letters*, 40(17):4481–4485, 2013. doi: 10.1002/grl.50751. URL <https://agupubs.onlinelibrary.wiley.com/doi/abs/10.1002/grl.50751>.
- A. Wellbrock, A. J. Coates, G. H. Jones, V. Vuitton, P. Lavvas, R. T. Desai, and J. H. Waite. Heavy negative ion growth in Titan’s polar winter. *Monthly Notices of the Royal Astronomical Society*, 490(2):2254–2261, 09 2019. ISSN 0035-8711. doi: 10.1093/mnras/stz2655. URL <https://doi.org/10.1093/mnras/stz2655>.
- J. H. Westlake, J. M. Bell, J. H. Waite Jr., R. E. Johnson, J. G. Luhmann, K. E. Mandt, B. A. Magee, and A. M. Rymer. Titan’s thermospheric response to various plasma environments. *Journal of Geophysical Research: Space Physics*, 116(A3), 2011. doi: 10.1029/2010JA016251. URL <https://agupubs.onlinelibrary.wiley.com/doi/abs/10.1029/2010JA016251>.
- J. H. Westlake, J. H. Waite Jr., N. Carrasco, M. Richard, and T. Cravens. The role of ion-molecule reactions in the growth of heavy ions in Titan’s ionosphere. *Journal of Geophysical Research: Space Physics*, 119(7):5951–5963, 2014. doi: 10.1002/2014JA020208. URL <https://agupubs.onlinelibrary.wiley.com/doi/abs/10.1002/2014JA020208>.
- E. Whipple. Potentials of surfaces in space. *Reports on progress in Physics*, 44(11):1197, 1981. Publisher: IOP Publishing.
- E. Wilson and S. Atreya. Chemical sources of haze formation in titan’s atmosphere. *Planetary and Space Science*, 51(14):1017 – 1033, 2003. ISSN 0032-0633. doi: <https://doi.org/10.1016/j.pss.2003.06>.

003. URL <http://www.sciencedirect.com/science/article/pii/S0032063303001338>. Surfaces and Atmospheres of the Outer Planets their Satellites and Ring Systems.
- R. Wilson, F. Crary, L. Gilbert, D. Reisenfeld, J. Steinberg, and R. Livi. *Cassini Plasma Spectrometer (CAPS) PDS user's guide*, 2012. Available at https://pds-ppi.igpp.ucla.edu/data/CO-E_J_S_SW-CAPS-3-CALIBRATED-V1.0/DOCUMENT/CAPS_USER_GUIDE/CAPS_PDS_USER_GUIDE_V1_00.PDF.
- A. K. Woodson, H. T. Smith, F. J. Crary, and R. E. Johnson. Ion composition in Titan's exosphere via the Cassini Plasma Spectrometer I: T40 encounter. *Journal of Geophysical Research (Space Physics)*, 120(1):212–234, Jan. 2015. doi: 10.1002/2014JA020499.
- S. K. Yeoh, Z. Li, D. B. Goldstein, P. L. Varghese, D. A. Levin, and L. M. Trafton. Constraining the Enceladus plume using numerical simulation and Cassini data. *Icarus*, 281:357–378, Jan 2017. doi: 10.1016/j.icarus.2016.08.028.
- Y. H. Yoon, S. M. Hörst, R. K. Hicks, R. Li, J. A. de Gouw, and M. A. Tolbert. The role of benzene photolysis in Titan haze formation. *Icarus*, 233:233–241, May 2014. doi: 10.1016/j.icarus.2014.02.006.
- D. Young, J. Berthelier, M. Blanc, J. Burch, A. Coates, R. Goldstein, M. Grande, T. Hill, R. Johnson, V. Kelha, D. Mccomas, E. Sittler, K. Svenes, K. Szegö, P. Tanskanen, K. Ahola, D. Anderson, S. Bakshi, R. Baragiola, B. Barraclough, R. Black, S. Bolton, T. Booker, R. Bowman, P. Casey, F. Crary, D. Delapp, G. Dirks, N. Eaker, H. Funsten, J. Furman, J. Gosling, H. Hannula, C. Holmlund, H. Huomo, J. Illiano, P. Jensen, M. Johnson, D. Linder, T. Luntama, S. Maurice, K. Mccabe, K. Mursula, B. Narheim, J. Nordholt, A. Preece, J. Rudzki, A. Ruitberg, K. Smith, S. Szalai, M. Thomsen, K. Viherkanto, J. Vilppola, T. Vollmer, T. Wahl, M. Wüest, T. Ylikorpi, and C. Zinsmeyer. Cassini Plasma Spectrometer Investigation. *Space Science Reviews*, 114(1):1–112, Sep 2004. ISSN

1572-9672. doi: 10.1007/s11214-004-1406-4. URL <https://doi.org/10.1007/s11214-004-1406-4>.

Z. Zhang, R. T. Desai, Y. Miyake, H. Usui, and O. Shebanits. Particle-in-cell simulations of the Cassini spacecraft's interaction with Saturn's ionosphere during the Grand Finale. *Monthly Notices of the Royal Astronomical Society*, 504(1): 964–973, June 2021. doi: 10.1093/mnras/stab750.

L. Zhao, R. I. Kaiser, B. Xu, U. Ablikim, M. Ahmed, M. M. Evseev, E. K. Bashkirov, V. N. Azyazov, and A. M. Mebel. Low-temperature formation of polycyclic aromatic hydrocarbons in Titan's atmosphere. *Nature Astronomy*, 2: 973–979, Oct. 2018. doi: 10.1038/s41550-018-0585-y.

K. Ågren, J. E. Wahlund, P. Garnier, R. Modolo, J. Cui, M. Galand, and I. Müller-Wodarg. On the ionospheric structure of Titan. *Planetary and Space Science*, 57(14):1821–1827, Dec. 2009. ISSN 0032-0633. doi: 10.1016/j.pss.2009.04.012. URL <http://www.sciencedirect.com/science/article/pii/S0032063309001263>.